

TEST OF THE $\Delta S = \Delta Q$ RULE AND CP-INVARIANCE

IN K_{e3} DECAY

Thesis by

John Daniel Gallivan

In Partial Fulfillment of the Requirements

For the Degree of

Doctor of Philosophy

California Institute of Technology

Pasadena, California

1971

(Submitted July 14, 1970)

ACKNOWLEDGEMENTS

The experiment described in this thesis was a major effort, even by the standards of high energy physics, and its success depended on a large number of physicists, technicians, programmers and scanners. In the course of this work, the author was influenced by many people. It is a pleasure to thank Professor Charles Peck, as academic advisor, for his patient and sympathetic guidance, and Professor Frank Sciulli, who supervised most of the research described herein, and who taught by example as much as by persuasion. The author also acknowledges the stimulating environment of the Caltech User's Group, in particular Professors David Binnie, Ricardo Gomez, and Alvin Tollestrup, and the cooperation of Michael Mallary as fellow graduate student on the experiment.

The Bevatron operations staff and members of the Lofgren Group at the Lawrence Radiation Laboratory gave invaluable assistance during the preparation and operation of this experiment at the Bevatron. A. Lake, D. Sell, W. Friedler, H. Grau, S. Sedleniek, and D. Toomer contributed to the design and construction of the equipment. Messrs. D. Chu, P. Walden, K. Young, G. Murata, and J. Stanley assisted in the setup and running stages of the experiment. Messrs. C. Lam, D. Molodowitch, J. Tam, and L. Young assisted materially in the data analysis. The scanning and measuring staff was supervised by J. Ferrari and included J. Edwards, M. Jolliff, M. Jordan, J. Lyon and G. Martin. The staff of the Caltech Computing Center gave the

author much assistance in programming and computer operations. The contributions of Dr. Bruce Sherwood who designed the PDP-8 program

EXPO, and Dr. James Van Putten who designed and built the lead plate spark chambers, are sincerely appreciated. Finally, this manuscript is evidence of Virginia Franklin's typing skill.

The author thanks the United States Atomic Energy Commission and the National University of Ireland for financial support during the author's graduate residence at Caltech.

ABSTRACT

The complex quantity $X = (\text{amplitude of the } \Delta S = -\Delta Q \text{ process } \bar{K}^0 \rightarrow \pi^- e^+ \nu / \text{amplitude of the } \Delta S = +\Delta Q \text{ process } K^0 \rightarrow \pi^- e^+ \nu)$ has been measured in a counter-spark-chamber experiment at the LRL Bevatron. Assuming CPT invariance, $\text{Im}X \neq 0$ implies CP-violation in the decay. K^0 -mesons were produced in two brass targets by 2.85 GeV/c pions. A series of veto counters and hodoscopes selected neutral decays into two charged particles. The electron and pion were identified by (1) pulse height in a Freon 12 threshold Cerenkov counter, (2) visual appearance in three radiation lengths of lead, and (3) pulse height in a set of fourteen shower counters. From 240K pictures, 1,079 events were isolated with a $(2 \pm 1)\%$ background level. A maximum likelihood fit to the $\pi^- e^+$ and $\pi^+ e^-$ time distributions gave the result:

$$\text{Re}X = -.069 \pm .036$$

$$\text{Im}X = +.108 \begin{array}{l} +.092 \\ -.074 \end{array}$$

This result is within two standard deviations of $X = 0$ and therefore consistent with it (relative probability = 0.25). It is, on the other hand, more than four standard deviations from the existing world average (+0.14, -0.13) and therefore inconsistent with it (relative probability $< 3.3 \times 10^{-4}$). Sensitivity of the result to a large number of possible systematic effects was investigated and it was concluded that any systematic error was small compared to the statistical error.

TABLE OF CONTENTS

<u>PART</u>	<u>TITLE</u>	<u>PAGE</u>
I.	INTRODUCTION	1
	(A) Theoretical Background of the $\Delta S = \Delta Q$ Rule	1
	(B) K_{e3}^0 Decay	6
	(C) History and Current Status of the $\Delta S = \Delta Q$ Rule	9
	(D) Experimental Measurement of X	13
	(E) This Experiment	15
II.	EXPERIMENTAL APPARATUS	19
	(A) General Features of the Apparatus	19
	(B) Triggering Components of the Apparatus	23
	(C) Data Recording Components	26
III.	DATA ANALYSIS AND BACKGROUNDS	32
	(A) Scanning	33
	(B) Measuring and Event Reconstruction	42
	(C) Final Selections	50
	(D) Estimation of Remanent Background	58
IV.	EFFICIENCY CALCULATION AND MAXIMUM LIKELIHOOD FITS	71
	(A) K_{e3} Efficiency Calculation	71
	(B) Maximum Likelihood Fitting of Data	85
V.	CONCLUSIONS AND OUTLOOK	100

TABLE OF CONTENTS (Continued)

<u>PART</u>	<u>TITLE</u>	<u>PAGE</u>
VI.	APPENDICES	103
VII.	REFERENCES	173

APPENDICES

<u>NUMBER</u>	<u>TITLE</u>	<u>PAGE</u>
1.	Theoretical Supplement	103
2.	Pion Beam	110
3.	Targets and Target Counters	114
4.	Spark Chambers	119
5.	Freon Cerenkov Counter	124
6.	Hodoscopes and Shower Counters	129
7.	Fast Electronics and Trigger Logic	135
8.	Slow Electronics and Computer	140
9.	Data-taking Procedures and Checks	142
10.	Scanning Procedures	143
11.	Measuring, Reconstruction and Track Fitting	157
12.	Monte Carlo Program	163
13.	Smearing of Time Distributions Used in Maximum Likelihood Calculation	170

LIST OF FIGURES

<u>FIGURE</u>	<u>CAPTION</u>	<u>PAGE</u>
1.	SU(3) Properties of Currents	5
2.	Terms I, II, III of $N^+(t)$	14
3.	The Nine Experimental Measurements of X Summarized in Table 1	17
4.	Experimental Apparatus	22
5.	Block Diagram of Trigger and Data Recording Logic	27
6.	Shower Counter Distributions of Electrons and Pions	34
7.	Electron Pulse Height in Shower Counters for Three Electron Energy Regions	35
8.	Average Individual Scanning Efficiency of Production-Decay Region Scan	41
9.	Distribution of χ^2_{track} in Decay-Shower Measurement	45
10.	$M_{p\pi}$ and $M_{\pi\pi}$ Distributions from Each Target	47
11.	χ^2 Per Degree of Freedom for All Tracks	48
12.	Distribution of $\Delta X_{\text{vertex}} = (X_{\text{plate}} - X_{\text{fit}})$	49
13.	Decay Position Distribution of All Events Passing Reconstruction	51
14.	Decay Position of Events Rejected by Quantitative Selections (1) - (7)	57
15.	Decay Position Distributions of Events Rejected in Shower Chamber Rescan	59
16.	Comparison of πe Sample with $\pi\pi$ Sample	63

LIST OF FIGURES (Continued)

<u>FIGURE</u>	<u>CAPTION</u>	<u>PAGE</u>
17.	$M_{e^+e^-}$ - Distributions from Lead Converter and πe Sample	66
18.	M_{ep} Distributions for e^+ and e^- Events	68
19.	Sketch of K^0 - production Distributions	75
20.	Comparison of Calibration Data and Monte Carlo for Momentum and Angle Distributions from Each Target	76
21.	Comparison of Decay Position Distribution for Calibration Data and Monte Carlo from Each Target	77
22.	Mean GC Pulse Height as a Function of Position for T1 πe Data	81
23.	Efficiency Functions at 2.8 Kg	82
24.	Comparison Between πe Data and Monte Carlo for Pion Momentum, Electron Momentum, and πe Resultant Momentum	83
25.	Comparison between πe Data and Monte Carlo for $m_{\pi e}$, the Invariant Mass of the πe	84
26.	Decay Position Distributions of Final πe Sample	88
27.	The Best Value of X from This Experiment	89
28.	Likelihood Contours for Fit to Sum	97
29.	Likelihood Contours for Fit to Asymmetry	98
30.	Sketch of π^- Beamline	111
31.	Block Diagram of Beam Electronics	112
32.	Number of Vees on Film and $\pi\pi$ Trigger Rate for Different Target Materials	116

LIST OF FIGURES (Continued)

<u>FIGURE</u>	<u>CAPTION</u>	<u>PAGE</u>
33.	Block Diagram of Target Electronics	118
34.	Sketch of Gas Cerenkov Counter	125
35.	Block Diagram of Gas Cerenkov Electronics	128
36.	Block Diagram of MH Electronics	130
37.	Block Diagram of RH Electronics	132
38.	Block Diagram of SH Electronics	134
39.	Block Diagram of Trigger Electronics	136
40.	Computer Scan Analysis of K_{e3} Trigger	144
41.	Electron Pulse Height in Shower Counters for Four Segments of Decay Region	145
42.	Pion Pulse Height in Shower Counters for Four Segments of Decay Region	146
43.	Horizontal Separation Between Pion and Electron at Shower Counters	148
44.	Shower Counter Pulse Heights of e and π for Different Charges	149
45.	Electron Acceptance of Computer Scan as a Function of Electron Energy	150
46.	Shower Scanning Criteria	152
47.	Production-Decay Region Scanning Criteria	154
48.	Special Cases in Production-Decay Region Scan	156
49.	Production-Decay Region Measurements	158
50.	Comparison Between Calibration Data and Monte Carlo for γ -profile of π	165

LIST OF FIGURES (Continued)

<u>FIGURE</u>	<u>CAPTION</u>	<u>PAGE</u>
51.	Comparison Between Calibration Data and Monte Carlo for Z-profile of π	166
52.	Comparison Between πe Data and Monte Carlo for Z-profile of e	168
53.	Comparison Between πe Data and Monte Carlo for Z-profile of π	169
54.	Difference in $N^+(N^-)$ with Various Corrections for Higher Moments of p_K - Spectrum	172

LIST OF TABLES

<u>TABLE</u>	<u>TITLE</u>	<u>PAGE</u>
1.	Measurements of X, 1963-69	16
2.	Effect of Quantitative Selections on πe Sample	56
3.	Backgrounds in πe Sample	70
4.	Corrections to K_{e3} Efficiency Function	79
5.	Fits with Variations in Fiducial Volume	93
6.	Fits with Variations in Mean Momentum, Mean Production Point and K_{e3} Efficiency Function	94
7.	Fits Made Investigating Background and Biases in Data	96
8.	Fast Logic Signals	138

I. INTRODUCTION

In the past decade, one of the most spectacular developments in particle physics has been the use of internal symmetries in understanding the interactions between elementary particles. The most prominent of these symmetries, $SU(3)$, combines isotopic spin and strangeness, both of which are conserved in the strong interactions. The weak interactions conserve neither isotopic spin nor strangeness and so violate $SU(3)$. However, as will be shown, the most elegant way of breaking $SU(3)$ implies certain selection rules in weak transitions. One of these is the $\Delta S = \Delta Q$ rule, which applies to strangeness-changing semileptonic transitions where ΔS is the change in strangeness and ΔQ the change in charge of the hadrons involved in the transition. The rule was first proposed in 1958 by Feynman and Gell-Mann and has been the subject of theoretical speculation and experimental investigation ever since. This thesis describes an experiment which studied the leptonic decay of the K-meson, $K \rightarrow \pi + e + \nu$ and measured the parameter X , the ratio of the $\Delta S = -\Delta Q$ amplitude $\langle \pi^- e^+ \nu | \bar{K}^0 \rangle$ to the $\Delta S = +\Delta Q$ amplitude $\langle \pi^- e^+ \nu | K^0 \rangle$.

A. Theoretical Background of the $\Delta S = \Delta Q$ Rule

In 1958 Feynman and Gell-Mann⁽¹⁾ formulated the presently accepted notion of the weak interaction as a current-current interaction, for which the interaction Lagrangian density has the form:

$$L_{\text{int}}^{\text{wk}}(\underline{x}) = \frac{-G}{\sqrt{2}} J_{\lambda}^{\dagger}(\underline{x}) \cdot J_{\lambda}(\underline{x}) \text{ where } G \sim 10^{-5} m_p^{-2} \text{ and } J_{\lambda}(\underline{x}) \text{ is a current}$$

which has contributions from all particles having weak interactions. J_λ has a vector part and an axial vector part which obey current conservation laws of varying degrees of validity. Up to the present, there is no evidence for scalar, pseudoscalar or tensor contributions to the currents although they are allowed by Lorentz invariance. If one separates J_λ into a leptonic part and a hadronic part, then L_{int}^{wk} becomes:

$$L_{int}^{wk}(x) = \frac{-G}{\sqrt{2}} \left\{ J_\lambda^{\dagger lept} J_\lambda^{lept} + (J_\lambda^{\dagger hadr} J_\lambda^{lept} + J_\lambda^{\dagger lept} J_\lambda^{hadr}) + J_\lambda^{\dagger hadr} J_\lambda^{hadr} \right\}.$$

The first term involves only leptons which do not have strong interactions. Matrix elements involving this first term can be accurately calculated by first order perturbation theory and experiments on the purely leptonic decay $\mu \rightarrow e \nu \bar{\nu}$ are consistent with the current:

$$J_\lambda^{lept} = \bar{\Psi}_\mu \gamma_\lambda (1 + \gamma_5) \Psi_{\nu_\mu} + \bar{\Psi}_e \gamma_\lambda (1 + \gamma_5) \Psi_{\nu_e}$$

in the usual relativistic Dirac spinor notation.

Of the terms involving hadrons, the first $J_\lambda^{\dagger hadr} J_\lambda^{lept} + J_\lambda^{\dagger lept} J_\lambda^{hadr}$, offers most hope of understanding, since J_λ^{hadr} occurs only once and its matrix elements are easier to handle than those of $J_\lambda^{\dagger hadr} J_\lambda^{hadr}$. The best known term in J_λ^{hadr} is the β -decay term involving nucleons, $\bar{\Psi}_p \gamma_\lambda (1 + C\gamma_5) \Psi_n$ where $C \sim 1.2$. In isotopic spin formalism this can be written $\bar{\Psi}_N I_+ \gamma_\lambda (1 + C\gamma_5) \Psi_N$ where Ψ_N is a general nucleon spinor, and I_+ is the isospin raising operator. Meson decays are accounted for by introducing terms containing meson fields into the hadronic current. The conserved vector current hypothesis pro-

vides an elegant prescription for adding the vector part of the meson current. For pions it is

$$J_{\lambda}^{\text{pion}}(\text{vector part}) = i[\Phi_{\pi}^{*} I_{+} \delta_{\lambda} \Phi_{\pi} - (\delta_{\lambda} \Phi_{\pi})^{*} I_{-} \Phi_{\pi}]$$

where Φ_{π} is the pseudoscalar pion field and I_{+} is the isospin raising operator. With this addition the vector current of nucleons and pions is conserved. $\pi^{+} \rightarrow \pi^{0} + e^{+} + \nu$ is an example of semileptonic pion decay and its experimental rate agrees well with that predicted by the above pion vector current.

The decays considered so far do not involve strangeness change ($\Delta S = 0$). To account for strangeness-changing ($\Delta S \neq 0$) decays of hyperons and K-mesons, terms involving these particles are introduced similar to the nucleon and pion terms. Still considering semileptonic processes only, the current $\Psi_p \gamma_{\lambda} (a + b\gamma_5) \Psi_{\Lambda}$ will give rise to Λ β -decay, $\Lambda \rightarrow p + e^{-} + \bar{\nu}$, and a combination of pion and K-meson fields similar to the pion current will give processes such as $K^{+} \rightarrow \pi^{0} + e^{+} + \nu$. Other possible terms in the $\Delta S \neq 0$ current are (abbreviating the bilinear form):

- (i) $(p, \Sigma^0), (n, \Sigma^{-}), (\pi^0, K^{-}), (\pi^{+}, \bar{K}^0)$
- (ii) $(n, \Sigma^{+}), (\Sigma^{-}, \Xi^0), (K^0, \pi^{+})$
- (iii) $(n, \Lambda), (\Sigma^{-}, \Xi^{-}), (\pi^0, \bar{K}^0)$

All the currents have been written with $\Delta S = +1$, but the first set has $\Delta Q = +1$ while the second and third sets have $\Delta Q = -1$ and $\Delta Q = 0$ respectively. So the first set of currents provide for the $\Delta S = +\Delta Q$

processes

$$\Lambda \rightarrow p + l^- + \bar{\nu}$$

$$\Sigma^- \rightarrow n + l^- + \bar{\nu}$$

$$K^+ \rightarrow \pi^0 + l^+ + \nu (\bar{\nu})$$

$$K^0 \rightarrow \pi^- + l^+ + \nu$$

while the second set provides for the $\Delta S = -\Delta Q$ processes

$$\Sigma^+ \rightarrow n + l^+ + \nu$$

$$K^0 \rightarrow \pi^+ + l^- + \bar{\nu}$$

$$\Xi^0 \rightarrow \Sigma^- + l^+ + \nu .$$

The third set cannot play a role in semileptonic processes since there are no known neutral leptonic currents. Feynman and Gell-Mann noted that $\Delta S = -\Delta Q$ terms like (n, Σ^+) were not needed to account for the observed hyperon decays and would lead to unobserved processes, $\Sigma^+ \rightarrow n + l^+ + \nu$. They also noted that $\Delta S = -\Delta Q$ in conjunction with $\Delta S = +\Delta Q$ terms would lead to decays such as $\Xi^- \rightarrow \pi^- n$ with $\Delta S = +2$.

With the advent of SU(3) symmetry for the strong interactions, the $\Delta S = \Delta Q$ rule appears in a very natural way. The pion and nucleon currents involve isospin through the I_+ operator which transforms like an object with $|\vec{I}| = 1$, $I_3 = +1$ and hence has the same SU(3) transformation properties as the π^+ . If the rules $|\Delta S| = 1$ and $\Delta S = \Delta Q$ are true for strangeness-changing decays, then the simplest SU(3) properties for the strangeness-changing current are those of the K^\pm -mesons. This is illustrated in Fig. 1(a) where the SU(3) spin

operator $F_1 + iF_2 (I_+)$ is identified with the π^+ and the $\Delta S = 1$, $\Delta S = \Delta Q$ SU(3) operator $F_4 + iF_5$ is identified with the K^+ . The current is represented by an arrow from the origin of a multiplet to the position of the particle having the same SU(3) transformation properties.

The octet current hypothesis, proposed by Cabibbo,⁽²⁾ consists of the proposal that all hadronic currents in the weak interaction are members of an SU(3) octet of currents. The currents shown in Fig. 1(a) are all charged; the remaining currents, which correspond to the π^0 , η , K^0 , \bar{K}^0 , are all neutral and hence do not take part in semileptonic decays. In this scheme, the semileptonic decays can be seen as transitions in the particle octets induced by the currents of Fig. 1(a), as shown in Fig. 1(b). Decays such as $K^0 \rightarrow \pi^+ + e^- + \bar{\nu}$ or $\Sigma^+ \rightarrow n + e^+ + \nu$ require transitions caused by currents which are not members of an octet, and so violate the $\Delta S = \Delta Q$ rule. In fact, the lowest SU(3) multiplets admitting such a member are $\underline{10}$ or $\overline{10}$ as shown in Fig. 1(c), where the currents correspond to Δ^- and $\bar{\Delta}^+$.

B. \underline{K}_{e3}^0 Decay

Measuring the magnitude of the $\Delta S = -\Delta Q$ amplitudes in hyperon decays, $\Sigma^+ \rightarrow n + \ell^+ + \nu$, $\Xi^0 \rightarrow \Sigma^- + \ell^+ + \nu$, involves direct measurement of the branching ratios for these processes. The situation is different for neutral K-mesons due to the $K_L - K_S$ phenomenon, whereby K-decay occurs from states which are almost eigenstates of CP and so are not eigenstates of strangeness. This means that $\bar{K}^0 \rightarrow \pi^- + e^+ + \nu$ can interfere with $K^0 \rightarrow \pi^- + e^+ + \nu$ and by studying the interference

one can measure the phase of any $\Delta S = -\Delta Q$ amplitude present relative to the $\Delta S = +\Delta Q$ amplitude. As shown in Appendix 1, there are four distinct amplitudes for K_{e3} decay

$$\left. \begin{array}{l} f, \text{ the amplitude for } K^0 \rightarrow \pi^- e^+ \nu \\ \bar{f}, \text{ the amplitude for } \bar{K}^0 \rightarrow \pi^+ e^- \bar{\nu} \end{array} \right\} \Delta S = +\Delta Q$$

$$\left. \begin{array}{l} \bar{g}, \text{ the amplitude for } K^0 \rightarrow \pi^+ e^- \bar{\nu} \\ g, \text{ the amplitude for } \bar{K}^0 \rightarrow \pi^- e^+ \nu \end{array} \right\} \Delta S = -\Delta Q$$

and one defines $X = g/f$ and $\bar{X} = \bar{g}/\bar{f}$. All of these functions involve a form factor which depends on q^2 , the square of the 4-momentum transfer between the K and the π . It is known⁽⁸⁾ that this dependence is small and it will be neglected from now on.

The discrete symmetries C,P and T imply relations between these amplitudes as shown in Appendix 1. CPT-invariance implies (* is complex conjugate) $\bar{f} = -f^*$ and $\bar{g} = -g^*$ so that $\bar{X} = X^*$. T-invariance in the transition implies that f, \bar{f}, g and \bar{g} are relatively real so that $\text{Im}X = \text{Im}\bar{X} = 0$. With CPT-invariance, $\text{Im}X \neq 0$ therefore implies direct CP-violation in leptonic K-decay. Sachs⁽³⁾ has suggested that such an effect could be the source of the CP-violation seen in $K_L \rightarrow 2\pi$ decay. This matter is discussed more fully in Appendix 1.

In Appendix 1 the leptonic time distributions are derived for a pure K^0 beam at $t = 0$. Assuming CPT-invariance, so that $\bar{X} = X^*$, one obtains

$$\begin{aligned}
N^{\pm}(t) = C|f|^2 & \left\{ |1 + X|^2 e^{-\Gamma_S t} + |1 - X|^2 e^{-\Gamma_L t} \right. \\
& \pm 2(1 - |X|^2) \cos \Delta m t e^{-\frac{1}{2}(\Gamma_L + \Gamma_S)t} \\
& \left. - 4 \operatorname{Im} X \cdot \sin \Delta m t e^{-\frac{1}{2}(\Gamma_L + \Gamma_S)t} \right\}
\end{aligned}$$

where Γ_S and Γ_L are the K_S and K_L total decay rates and Δm is $(m_{K_L} - m_{K_S})$. In the detailed derivation, CP-violating effects in the $K_L - K_S$ states are taken into account. Such effects are of the order 2×10^{-3} , well below the sensitivity attainable with present experiments and are omitted in the expression for $N^{\pm}(t)$. For $t = 0$, the above expression becomes $N^+(0) = 4|f|^2$, $N^-(0) = 4|f|^2|X|^2$ so that $N^-(0)/N^+(0) = |X|^2$, as one would expect before the $K^0 - \bar{K}^0$ interference comes into effect for $t > 0$.

C. History and Current Status of the $\Delta S = \Delta Q$ Rule

Most checks of the $\Delta S = \Delta Q$ rule have been in Σ^+ and K_{e3} decay. $K_{\mu 3}^0$ decay is considerably more difficult; in bubble chambers there are possible charge asymmetries in μ^+/μ^- identification, and in counter experiments one has to operate at fairly high energies to filter μ 's from hadrons. There is also serious background from $K_S \rightarrow \pi^+ + \pi^-$, with one of the π 's undergoing undetected $\pi \rightarrow \mu\nu$ decay.

The first experimental evidence on the $\Delta S = \Delta Q$ rule was reported at the 1962 CERN Conference⁽⁴⁾ and it placed the rule in serious doubt. First, an example of $\Sigma^+ \rightarrow n \mu^+ \nu$ decay was reported and, secondly, two K_{e3}^0 experiments found evidence for large violation. The Σ^+ -event was found in an emulsion stack exposed to K^- -mesons⁽⁵⁾ and the authors were well aware of the danger of drawing sweeping conclusions from one event. They did not report any examples of the allowed $\Sigma^- \rightarrow n \mu^- \bar{\nu}$ decay mode which would have been helpful in understanding the $\Sigma^+ \rightarrow n \mu^+ \nu$ event.

The K_{e3} experiments^{(6), (7)} had 28 and 22 events respectively and the data was analyzed in terms of $\Gamma_1/\Gamma_2 = (\text{Total } K_1 \text{ leptonic rate} / \text{Total } K_2 \text{ leptonic rate}) = \left| \frac{1+X}{1-X} \right|^2$. CP-conservation was assumed, i.e., $\text{Im}X$ was fixed at zero. If $\Delta S = \Delta Q$ then $\Gamma_1/\Gamma_2 = 1$. The results were $\Gamma_1/\Gamma_2 = 11.9^{+7.5}_{-5.6}$ and $6.6^{+6.0}_{-4.0}$ respectively. The first experiment separated the data into $\pi^+ e^- \nu$ and $\pi^- e^+ \nu$ events to distinguish between

X and $1/X$ and gave $X = 0.55 \begin{smallmatrix} +.08 \\ -.12 \end{smallmatrix}$. The second experiment could not do this but, taking the value of X which was less than unity, they obtained $X = 0.44 \begin{smallmatrix} +0.12 \\ -0.20 \end{smallmatrix}$. Crawford, in his rapporteurs talk to the 1962 conference summarized: "The conclusion is that the $\Delta S = \Delta Q$ rule is probably wrong." However, admixture of $K_S \rightarrow \pi^+ \pi^-$ background in the leptonic decay sample gives $\Gamma_1/\Gamma_2 > 1$ and it is noteworthy that both of these results are in that direction.

In the seven years that elapsed until the 1969 Topical Conference on Weak Interactions at CERN, the $\Delta S/\Delta Q$ problem was attacked with great energy on both the Σ^+ and K_{e3} fronts, the K_{e3} case being given considerable impetus by the discovery of CP-violation in $K_L \rightarrow 2\pi$ decay.

At the 1969 conference, Filthuth⁽⁸⁾ reported a $\Sigma^+ \rightarrow n e^+ \nu$ event and two more $\Sigma^+ \rightarrow n \mu^+ \nu$ events, all three being from H_2 bubble chambers. The electronic event⁽⁹⁾ corresponded to a bubble count 3.6 standard deviations from that expected for a pion, with a 1% probability that the track was not an electron. For the exposure yielding the muonic events,⁽¹⁰⁾ it was calculated that 0.3 background events of the type:

$$\Sigma^+ \rightarrow n \pi^+ \gamma$$

followed by $\pi^+ \rightarrow \mu^+ \nu$ (with decay vertex undetected)

would be present in the sample. Thus the probability of the two candidates being due to this background is $\sim 4\%$. These new events gave totals of $3 \Sigma^+ \rightarrow \mu^+ / 177 \Sigma^- \rightarrow \mu^-$ and $1 \Sigma^+ \rightarrow e^+ / 931 \Sigma^- \rightarrow e^-$ which corresponded to a branching ratio $\Gamma(\Sigma^+ \rightarrow n \ell^+ \nu) / \Gamma(\Sigma^- \rightarrow n \ell^- \nu) \sim .03$. On the

basis of these events it should be noted that the ($\Delta S = -\Delta Q$ rate)/($\Delta S = +\Delta Q$ rate) for muons is 1.5 times that for electrons whereas a naive theory would predict the same ratio for muons and electrons.

Rubbia,⁽⁸⁾ at the same conference, discussed K_{e3} decay and from eight new experiments done since 1962, compiled a world average for X:

$$\text{Re}X = +0.14 \pm 0.05$$

$$\text{Im}X = -0.13 \pm 0.043 .$$

This world average clearly contradicted the evidence for a gross violation displayed at the 1962 conference. The experiments contributing to it are tabulated in the next section.

One other test of the $\Delta S = \Delta Q$ rule is experimentally accessible; the decay $K^+ \rightarrow \pi^+ \pi^- e^+ \nu$ being allowed while $K^+ \rightarrow \pi^+ \pi^+ e^- \bar{\nu}$ is forbidden. The 90% confidence limit for this process is $\Gamma(K^+ \rightarrow \pi^+ \pi^+ e^- \bar{\nu}) / \Gamma(K^+ \rightarrow \pi^+ \pi^- e^+ \nu) < 0.04$ based on 264 K_{e4} $\Delta S = +\Delta Q$ events with no $\Delta S = -\Delta Q$ candidates seen. (Rubbia's talk, Ref. (8).)

This completes the discussion of the direct checks of the $\Delta S = \Delta Q$ rule and the conclusion in 1969 was that the $\Delta S = -\Delta Q$ amplitudes were $< 20\%$ of the $\Delta S = +\Delta Q$ amplitudes. Two indirect implications of $\Delta S = -\Delta Q$ currents will now be discussed.

If the current-current picture has $\Delta S = -\Delta Q$ currents as well as $\Delta S = +\Delta Q$ currents, then these can combine to give $\Delta S = 2$ processes with amplitudes which are first order in the weak interaction coupling constant. Examples of such processes are $\Xi^- \rightarrow n \pi^-$ and $K^0 \leftrightarrow \bar{K}^0$. The observed branching ratio for $\Xi^- \rightarrow n \pi^-$ is $< 1.1 \times 10^{-3}$ (11) and it

is well known that the $K_L - K_S$ mass difference, which is proportional to $\langle K^0 | H | \bar{K}^0 \rangle$, is second order in G ($\Delta m \sim \Gamma_S/2$) indicating that $K^0 \leftrightarrow \bar{K}^0$ transitions are forbidden in first order. The current-current picture would thus need modification to accommodate $\Delta S = -\Delta Q$ currents, if they were found.

The $|\Delta I| = \frac{1}{2}$ rule for semileptonic decays states that the change in the total isospin of the hadrons in such a process is $\frac{1}{2}$. If one defines α_{11} , α_{31} , and α_{33} corresponding to isospin changes $(\Delta I, \Delta I_3) = (1/2, 1/2)$, $(3/2, 1/2)$ and $(3/2, 3/2)$ then the $|\Delta I| = \frac{1}{2}$ rule states that $\alpha_{31} = \alpha_{33} = 0$, whereas the weaker $\Delta S = \Delta Q$ rule states that $\alpha_{33} = 0$ alone. Evidence from K^+ and K_L semileptonic rates gives (see Rubbia's talk, Ref. (8)):

$$\text{Re} \frac{(\alpha_{31} + \sqrt{3} \alpha_{33})}{\alpha_{11}} = (3.4 \pm 13) \times 10^{-3} .$$

Since $\frac{\sqrt{3} \alpha_{33}}{\alpha_{11}} \approx 4.2 X$, a violation of $\Delta S = \Delta Q$ corresponding to $\text{Re} X \gtrsim 2\%$ would require a subtle conspiracy between α_{31} and α_{33} to maintain the above relation.

The conclusion from all available data in 1969 was that there was no definitive evidence for $\Delta S = -\Delta Q$ currents in the weak interactions but the experimental limit on such amplitudes was fairly large. In view of the implications of non-zero X just mentioned and the importance of measuring $\text{Im} X$ accurately to help understand CP-violation, an improvement in the measurement of X by at least an order of magnitude was called for.

D. Experimental Measurement of X

If the expression for $N^{\pm}(t)$ is rewritten with quadratic terms omitted and $\Gamma_L t = 0$, one obtains:

$$N^+(t) = (e^{-\Gamma_S t} + 1) \pm 2 \cos \Delta m t e^{-\frac{1}{2} \Gamma_S t} \quad \text{I}$$

$$+ 2 \operatorname{Re} X (e^{-\Gamma_S t} - 1) \quad \text{II}$$

$$- 4 \operatorname{Im} X \sin \Delta m t e^{-\frac{1}{2} \Gamma_S t} \quad \text{III}$$

In Fig. 2 the features of terms I, II, and III can be seen. Taking $\Delta m \sim \Gamma_S/2$, the wavelength of the periodic terms is $4\pi/\Gamma_S$ which is roughly 12 K_S lifetimes. As they are damped by an exponential these terms are essentially constant after 5 K_S lifetimes. The best way to measure the coefficients of the terms in $N^{\pm}(t)$ is to collect a sample of leptonic decays in flight within the first 10 or so lifetimes, separate them into the two charge states, and fit the parameter X using the time distributions $N^{\pm}(t)$.

Since leptonic decays occur at $\sim 10^{-3}$ times the rate of the usual $K_S \rightarrow \pi^+ \pi^-$ one would expect backgrounds from K_S decay to be a major problem and to be most competitive at short lifetimes. Thus the effect of such an excess of events on the measurement of X should be considered. From the expression for $N^{\pm}(t)$ one finds:

$$\frac{(N^+ + N^-) \text{ at } t = 0}{(N^+ + N^-) \text{ at } t \sim \infty} \sim \frac{2}{1 - 2 \operatorname{Re} X}, \text{ hence an excess of events at}$$

$t = 0$ will give $\operatorname{Re} X > 0$ for both K^0 and \bar{K}^0 initial states, e.g. a 10% excess of $K_S \rightarrow \pi^+ \pi^-$ background will increase $\operatorname{Re} X$ by .05.

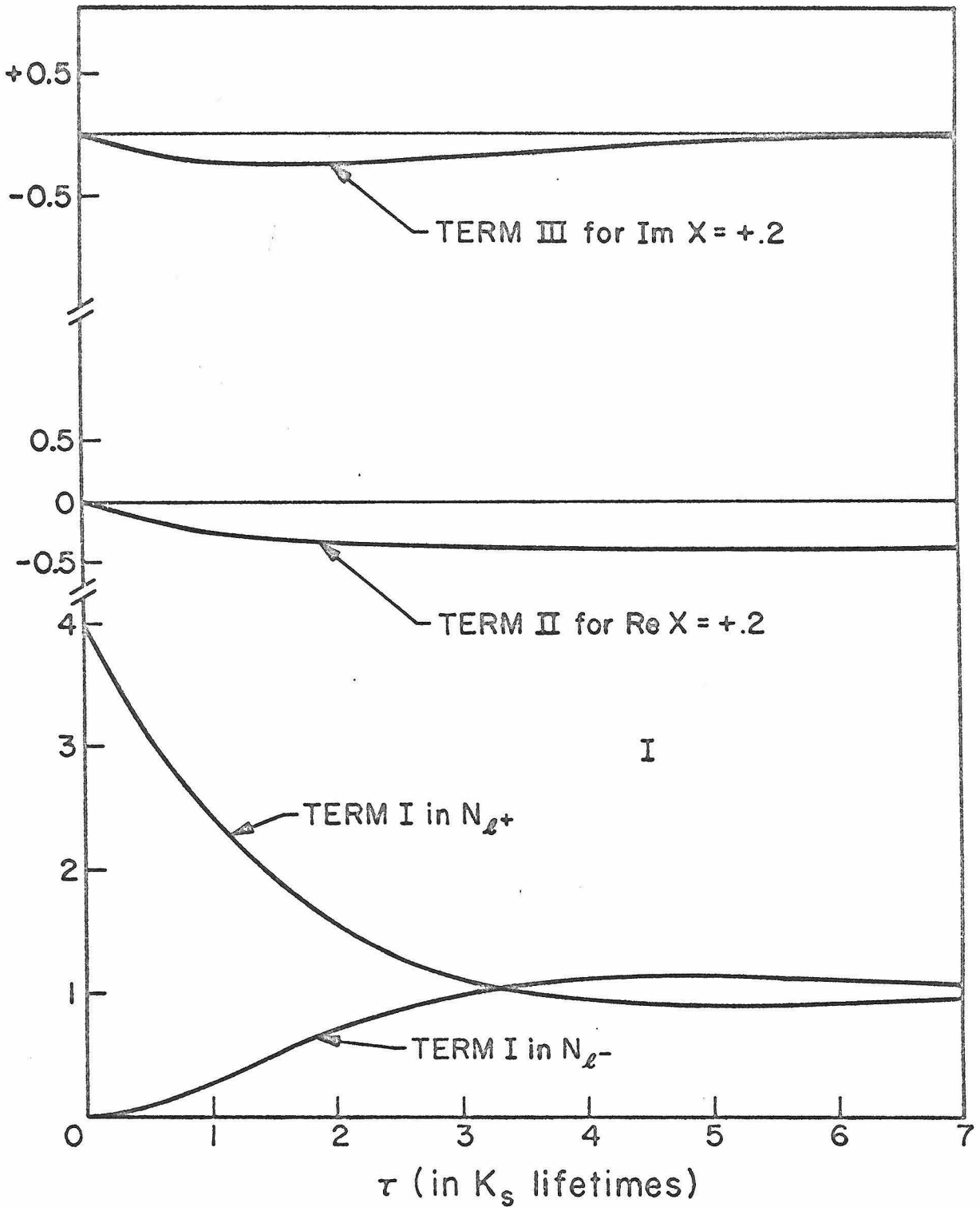


Fig. 2 Terms I, II and III of $N^{\pm}(t)$.

A compilation of all experiments done since 1963 is given in Table 1, with the same results shown on an Argand plot in Fig. 3. It is interesting to note that 7 of the 8 experiments give $\text{Re}X > 0$. Each of the experiments suffers from a small number of events and so has serious difficulties in investigating systematic errors. Therefore, one should not place much faith in an average derived from them, but if this is done for the first eight experiments, the result is $\text{Re}X = +0.14 \pm 0.05$, $\text{Im}X = -0.13 \pm 0.04$. Ref. (20) measured $(1 - |X|^2)/|1 - X|^2$ from the amplitude of oscillation of the charge asymmetry following a regenerator in which the phase was measured. The strongest conclusion to be drawn from these experiments is that $|X| \lesssim 0.2$.

E. This Experiment

In order to place a better limit on X it was desirable to do a high statistics experiment for which the systematic errors could be estimated well within the statistical error. In view of the importance of CP-violation in the $K^0 - \bar{K}^0$ system, it was decided to aim for equal sensitivity in $\text{Im}X$ as for $\text{Re}X$ and so it was necessary to reach high acceptance well within the first K_S lifetime where the charge asymmetry is greatest. It can be shown that the statistical error on X, for $X = 0$, depends on the number of events approximately as follows:

$$\sigma_{\text{Re}X}^2 \approx .8/n'$$

$$\sigma_{\text{Im}X}^2 \approx 1.1/n'$$

$$\text{where } n' = \left. \frac{dN}{dt} \right|_{t=0}, \frac{dN}{dt}$$

TABLE 1. MEASUREMENTS OF X, 1963 - 1969

Group	Method	K_{e3} Events	$ \Delta m $ in Units of Γ_S	ReX	ImX	Ref.
Paris (1965)	Freon/Prop. B.C., $K^+n \rightarrow K^0p$	315	$.47 \pm .20$	$.035^{+.11}_{-.30}$	$-.21^{+.15}_{-.11}$	12
Padua (1965)	do.	152	$.15^{+.35}_{-.50}$	$.06^{+.18}_{-.44}$	$-.44^{+.32}_{-.19}$	13
Columbia/ Rutgers (1965)	H_2 BC \bar{p} -p	109	= .5	$-.08^{+.16}_{-.28}$	$.24^{+.40}_{-.30}$	14
Penn. (1966)	Sp. Chamber $\pi^-p \rightarrow K^0\Lambda$	116	?	$.17^{+.16}_{-.35}$	$.00^{+.25}$	15
Brookhaven /Carnegie (1967)	D_2 BC $K^+n \rightarrow K^0p$	335	= .5	$.17 \pm .10$	$-.20 \pm .10$	16
Berkeley (1968)	H_2 BC $K^-p \rightarrow \bar{K}^0n$	242 (includes $K_{\mu 3}$ events)	= .47	$.22^{+.07}_{-.09}$	$-.08 \pm .08$	17
CERN/ Paris (1968)	H_2 BC \bar{p} -p	121	= .47	$.09^{+.13}_{-.11}$	$.22^{+.29}_{-.37}$	18
San Diego (1969)	Sp. Chamber $K^+Cu \rightarrow K^0$	686	= .46	$.09^{+.14}_{-.16}$	$-.11^{+.10}_{-.11}$	19
Average				$.14 \pm .05$	$-.13 \pm .043$	
CERN/ Columbia (1969)	Counter Reg. K_L Beam	?	= .469	$\frac{1- X ^2}{ 1-X ^2} = .96 \pm .05$		20

(= means input, not a free parameter in fit)

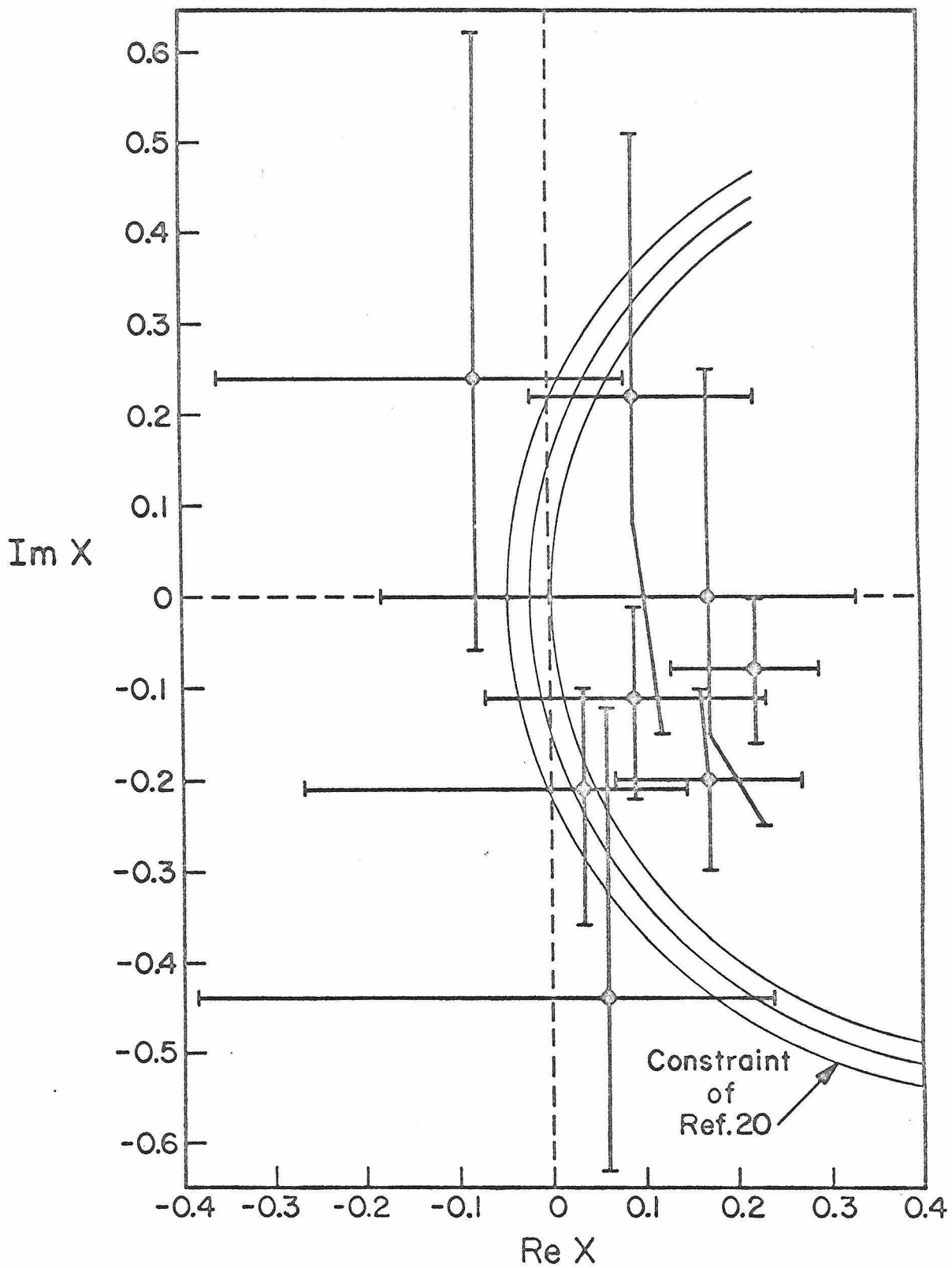


Fig. 3 The nine experimental measurements of X summarized in Table 1.

being the total number of events per K_S lifetime. With $n' = 500$, the error on $\text{Re}X$ is ± 0.04 and on $\text{Im}X$ it is ± 0.047 . The sensitivity to background is such that a 2% admixture of $K_S \rightarrow \pi^+\pi^-$ gives $\text{Im}X = -0.01$, $\text{Re}X = +0.01$ for $X = 0$. So in an experiment with $n' \sim 500$ it is enough to keep this background below 2%.

The method, which is described in detail in the next chapter, was to produce K-mesons in an apparatus that could detect K_{e3} decays from 0.2 to 7.0 K_S lifetimes. The K-mesons were produced by pions in small brass targets in front of a large aperture magnet in which the decay secondaries were momentum analyzed. Sensitivity to electrons and rejection of heavier secondaries was achieved using a combination of gas Cerenkov counter, visual shower chambers and shower counters. The experiment involved taking pictures of some 240K candidates from which a final sample of 1079 K_{e3} events was isolated with a background level of $(2 \pm 1)\%$. The value of X estimated from these events is:

$$\text{Re}X = -0.069 \pm 0.036$$

$$\text{Im}X = +0.108 \begin{array}{l} +0.092 \\ -0.074 \end{array} .$$

The error on $\text{Im}X$ is larger than expected because X is sufficiently far from zero that the above error analysis is only approximate.

This thesis is divided into four more chapters. Chapter II discusses the experimental method and apparatus, Chapter III describes the procedure used to isolate the final sample of K_{e3} 's, Chapter IV deals with the Monte Carlo efficiency calculation and the maximum likelihood fits to the data and Chapter V finishes the thesis with conclusions and outlook for the $\Delta S = \Delta Q$ rule.

II. EXPERIMENTAL APPARATUS

The experiment was executed in 1968 at the Bevatron, a 6 GeV weak focusing proton synchrotron at the Lawrence Radiation Laboratory in Berkeley. As stated in the previous chapter, the object of the experiment was to acquire a sample of K_{e3}^0 decays with known efficiency in time over the first 7 K_S lifetimes and to extract the value of X from this sample by fitting it with the time distributions $N^+(t)$ and $N^-(t)$. This was achieved with an apparatus which was sensitive to decays of neutral particles into an electron and a pion and which determined the charges of the decay products. This chapter is divided into three sections. The first describes the general features of the apparatus, the second gives a more detailed description of the triggering components, and the third describes how data were recorded for the events that satisfied the trigger.

A. General Features of the Apparatus

Since a major goal of the experiment was to get more events than the previous experiments, it was decided to produce the K^0 -mesons from dense target material rather than from hydrogen. This meant that the kinematical constraints of a proton target could not be used to identify the K_{e3}^0 's as was done in the bubble chamber experiments. Instead, the two charged prongs from a neutral decay were identified, one as an electron by its production of Cerenkov radiation and its showering properties in lead, the other as a non-showering, non-Cerenkov-radiating particle which had to be a muon, a pion or a proton. By a process of elimination, the only neutral decays having such a

final state are $\Lambda \rightarrow p + e^- + \bar{\nu}$ and $K^0 \rightarrow \pi^+ + e^- + \nu$. The momenta of the secondaries were measured in a large spectrometer so one was able to eliminate Λ_{β} events by a cut on the $(p e)$ invariant mass.

The technique was based on achieving three goals:

- (1) The ability to isolate neutral decays. The triggering system was designed to favour neutral decays and these could be seen in spark chambers placed throughout the decay region by observing the characteristic two-prong vee of a neutral decay.
- (2) Good differentiation between electrons and heavier particles so that one particle in the final state was an electron and the other a heavier particle. This distinction was made by the pulse height in a 1 atm. Freon Cerenkov counter, by the visual appearance of the particles in three radiation lengths of shower chambers and by their pulse heights in a set of shower counters.
- (3) Enough mass resolution to make necessary mass cuts. The decay secondaries traversed more than 100 Kg-inches of magnetic field, with spark chambers to determine the trajectory. The momenta were determined with $\Delta p/p \sim 5\%$.

Negative pions were used to produce K^0 's by associated production from brass targets. A beam momentum of 2.85 GeV/c was chosen. It was determined that this momentum was roughly optimum for the experimental configuration by consideration of the following four effects:

- (1) Available beam intensity, which decreases with momentum,
- (2) K^0 -production cross section, which also decreases with

momentum,

- (3) Apparatus acceptance, which increases with K^0 -momentum,
- (4) Electron identification by showering, which is better, the higher the electron energy.

At this momentum the beam intensity could be as large as 400K/accelerator pulse with about half of the circulating proton beam striking the target used to produce the pions.

A general sketch of the apparatus is shown in Fig. 4. The largest component is the M-5 spectrometer magnet which has 60" diameter poles and an aperture of 108" (horizontal) x 22" (vertical). The field value at first was 2.0 Kg, and later in the run it was increased to 2.8 Kg. Most of the other components were either attached to the magnet or else placed as close as was physically possible. The pion beam, through S3 and S4, impinged on two brass targets placed inside a set of thin plate spark chambers. Production of a neutral particle was demanded in one of the two targets by the signature $C_i \bar{V}_i$ in either target. The counter, S5, placed after the decay region, was used to trigger on decays occurring in the region. A Freon gas Cerenkov counter, GC, which detected electrons, was placed inside the magnet. There were two hodoscopes, MH at the center of the magnet and RH at the back, which demanded two particles through the magnet aperture into the shower chambers. A set of four spark chambers, SC, inside and at the rear of the magnet was used to record the particle trajectories through the magnetic field region. Finally, at the back of the RH, were the shower chambers and shower counters, in which the showering properties of the decay secondaries were studied in five

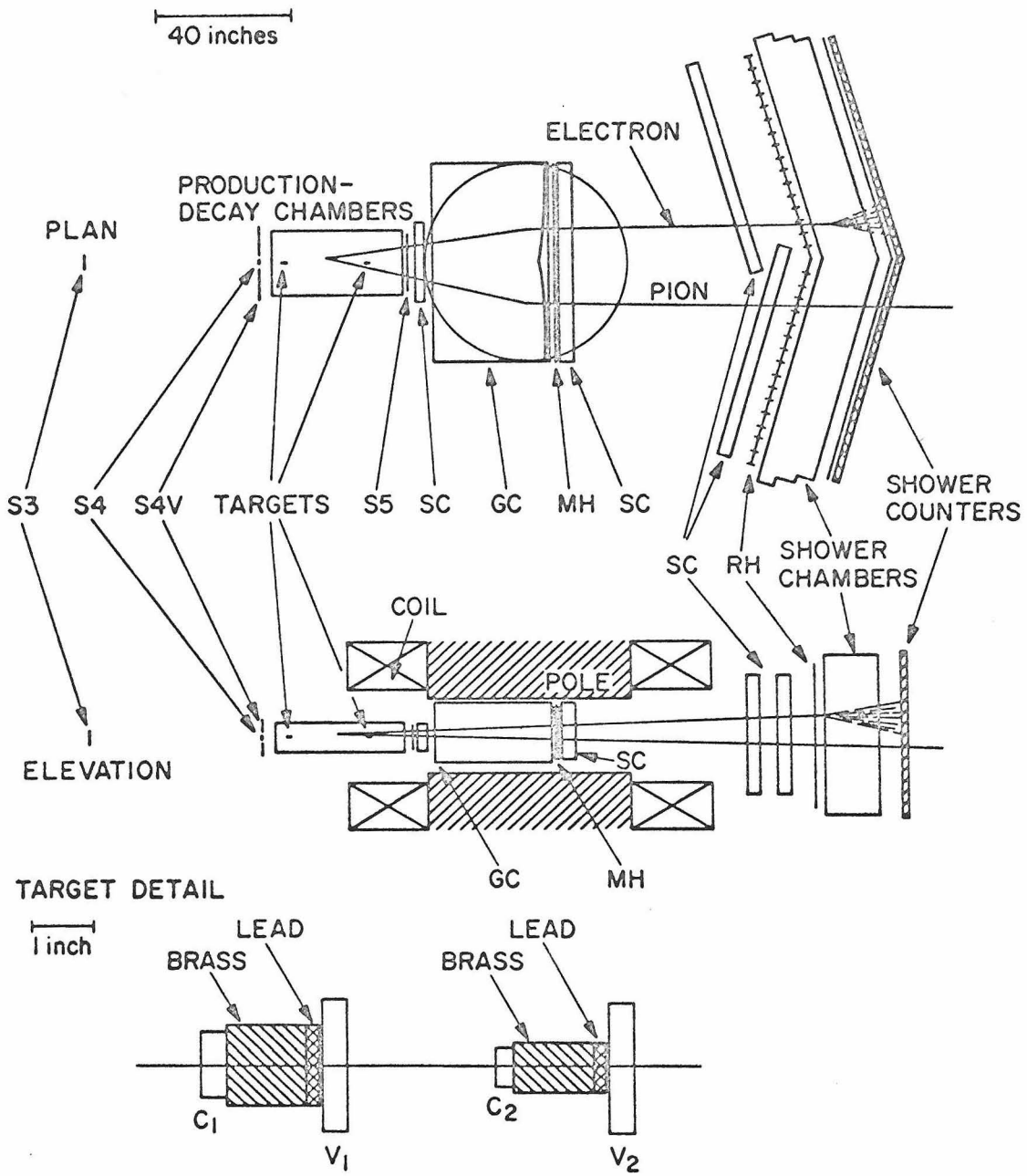


Fig. 4 Experimental apparatus

radiation lengths of lead. All of these components will now be described in the remainder of this chapter. Detailed discussion of the apparatus is contained in Appendices 2-8, and only those features directly affecting the physics will be included here.

B. Triggering Components of the Apparatus

Approximately 1 in 10^7 of the pions interacting in the targets led to a K_{e3} decay accepted by the apparatus so it is clear that selective triggering was needed to reduce the number of events to be recorded for subsequent analysis. This section deals with the components that played a role in this selection process.

Before entering the production region, the beam particle traversed four small counters S1, S2, S3, S4 and a large veto counter S4V which had a hole for the beam and removed off-axis beam particles. A good beam particle had the signature S3.S4. $\overline{S4V}$.

The selection of neutral particles was achieved by producing them in two brass targets T1 and T2, 1.2" long, and placing a veto counter 2.0" in diameter immediately downstream of the target. A pion was required to enter a target by the counters C_1 or C_2 immediately upstream of the targets so a neutral trigger from either target had the signature $C_i \overline{V}_i, i=1,2$. A scintillator 7" x 18" x 1/8", S5, placed 13" downstream from the second target ensured that a decay took place in the region viewed by spark chambers. The first target produced K^0 's that could decay over seven decay lengths which is where the time distributions, $N^\pm(t)$ reach a constant level, whereas the second target had only two K_S decay lengths available for decay, but

K^0 's produced in it had three times more likelihood of being accepted by the apparatus than K^0 's from the first target. The beam was tuned to maximize the counting rates in C_1 and C_2 . About 99% of the beam impinged on C_1 and, after multiple scattering and interacting in the first target, about 36% reached C_2 .

The selection of two charged particles through the magnet aperture was effected by two hodoscopes, MH and RH. The multiples hodoscope, MH, was a horizontal hodoscope at the center of the magnet consisting of fifteen 1" wide counters and the rear hodoscope, RH, had thirty-two 4" wide counters arranged vertically. The MH was helpful in reducing the contamination from small angle electron pairs which did not open out very much in the vertical direction since the magnetic field was in that direction. For the K_{e3} trigger it was demanded that the two charged particles be separated by at least one counter, i.e., at least 1" in space. The RH ensured that two particles reached the rear of the apparatus and had a high probability of entering the shower chambers and shower counters where their interaction in five radiation lengths of lead could be studied. There was no separation requirement here, and the RH trigger was satisfied by any two counters firing.

Decays where one of the decay products was an electron were selected by a threshold gas Cerenkov counter which had a radiator of Freon 12(CCl_2F_2) close to atmospheric pressure, with a pathlength of 30" through the gas. The counter was placed between the poles of the magnet as close to the decay region as possible and had thin mylar windows at both entry and exit. Since the threshold for pions at this

pressure is about 3 GeV/c, the counter was uniquely sensitive to electrons and could only count pions which were accompanied by a γ -conversion or a fast δ -ray. The mean pulse height from electrons in the counter corresponded to about five photoelectrons in the RCA 8575 phototubes which gave an operating efficiency $> 93\%$. From studies of the pulse height spectrum of electrons from different sections of the decay region, it was concluded that the efficiency varied by at most 1.2% over the decay region. The Cerenkov light was reflected by spherical mirrors into two lightpipes, one on each side of the beam. Each lightpipe had three RCA 8575 phototubes. The discriminator threshold to satisfy a GC trigger was set at a very low level to ensure high efficiency. The separate sides were also pulse height analyzed and the pulse heights stored on tape if the K_{e3} trigger was satisfied.

This concludes the discussion of the components in the K_{e3} trigger which was defined as:

S3.S4. $\overline{S4V}$.($C_1\overline{V}_1$ from either target).S5.(two MH counters fire with at least one counter separation).(two RH counters fire).(pulse from GC, set at very low bias).

At the typical intensity of 3×10^5 effective pions per pulse (i.e., usable by the electronics) this trigger gave 0.9 triggers per pulse. The contribution made by the various elements can be judged from the following rates (there are, of course, correlations between the rates). With 3.0×10^5 pions per pulse,

S3.S4. $\overline{S4V}$.C ₁ \overline{V}_1 .S5	180/pulse
S3.S4. $\overline{S4V}$.C ₂ \overline{V}_2 .S5	220/pulse
GC	1.4 x 10 ⁴ /pulse
S3.S4. $\overline{S4V}$.S5.MH	1.0 x 10 ⁴ /pulse
S3.S4. $\overline{S4V}$.S5.RH	2.6 x 10 ⁴ /pulse
S3.S4. $\overline{S4V}$.(C ₁ \overline{V}_1 + C ₂ \overline{V}_2).S5.MH.RH	10./pulse
K _{e3} trigger =	" .GC 0.9/pulse

Another experiment to look for interference effects between $K_S \rightarrow \pi^+ \pi^- \pi^0$ and $K_L \rightarrow \pi^+ \pi^- \pi^0$ ran simultaneously with the K_{e3} data-taking and had a trigger rate of 1.0 per 3×10^5 pions. The overall deadtime with these two triggers was 30%. A general block diagram of the triggering and data recording is shown in Fig. 5.

C. Data Recording Components

Having considered how the apparatus was triggered, the next topic is to describe the remaining components that recorded data from triggering events. These were three separate groups of spark chambers and a set of fourteen shower modules.

Production-decay region chambers

In the region where the K^0 's were produced and in which they later decayed, there were seven spark chamber modules, each 4" x 8" x 18". The targets were placed in the gaps between the first and second, and the fifth and sixth modules. The modules after the targets were placed as close as possible to the veto counters V_1 and V_2 , so that there was

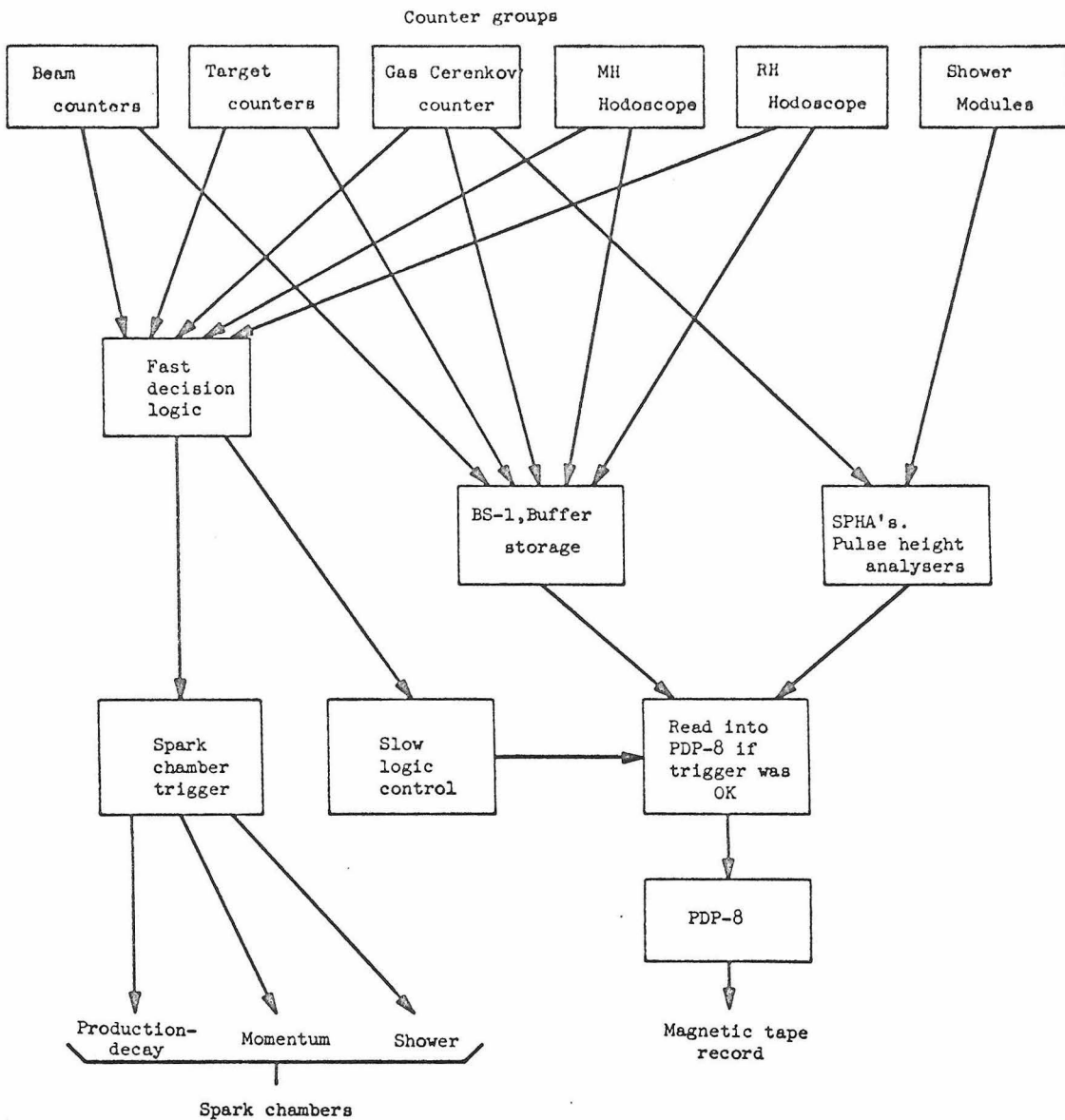


Fig. 5 Block diagram of trigger and data recording logic

an active gap about $3/4$ " from the end of each target. The decay point of a neutral particle could be seen within 1" of its production. At the mean K^0 -momentum of 2.4 GeV/c, this corresponded to $0.2 K_S$ lifetimes. The length of the fiducial volume along the beam in which decays were visible was 34" for the first target and 10" for the second target, corresponding to 7 and $2 K_S$ lifetimes respectively at $P_K = 2.4$ GeV/c. The transverse spatial resolution attained with these chambers was $\sim .1$ " and an angular resolution ~ 10 mr for an average length track. This led to a resolution for the longitudinal coordinate of a typical decay vertex of ~ 0.3 ", which is to be compared with the uncertainty of 0.4" in the K^0 production point. The multi-track efficiency of these chambers was crucial to the detection of neutral decays with uniform efficiency throughout the decay volume. Extra tracks from a target most often tended to be present in the first 5" of chamber after the target. If the chambers were inefficient, decays occurring in this region would be difficult to see, due to the robbing effect of the extra tracks. From looking at the pictures, it appears that the chambers could support up to three tracks well, but four or more tracks became difficult to see, with some tracks robbing energy from the sparks in other tracks.

Momentum chambers

The next chambers encountered by the secondaries in their passage through the magnet was a group of four chambers referred to as momentum chambers because of their momentum determining role. The first was 8" x 24" with six $\frac{1}{16}$ " gaps and it was placed between the S5 counter and the entrance window of the gas counter. The second was

immediately after the MH and was 60" x 18" with four $3/8$ " gaps. Finally, at the rear of the magnet, at 16° to the normal to the beam, were two 36" x 60" chambers, each with six $3/8$ " gaps, one chamber on each side of the center line. These chambers were viewed by excellent optics rigidly bolted to the magnet yoke and gave spatial resolutions of the order .05".

Shower chambers

The interaction of the decay secondaries in three radiation lengths of lead was studied in shower chambers which consisted of a total of six modules, three on each side of the center line. A module was 4' x 6' and had nine plates with $1/4$ " gaps. The plates were formed of an Al-Pb-Al sandwich, .02" Al on either side of .02" Pb, giving 0.1 radiation lengths per plate. The chambers had six active gaps per module so a shower could be studied in eighteen gaps if it penetrated to the back of the array. Shower maximum is reached after three radiation lengths by 0.7 GeV/c electrons which is a fairly typical energy for the electrons of accepted K_{e3} 's. Since the ability of the chambers to distinguish between π 's and e's depends on the scanning criteria used, discussion of the identifying power of the shower chambers will be postponed until the next chapter. The optics used in the photography of these chambers was not as good as that used in the other two sets of chambers since it involved very large mirrors mounted at awkward angles. The spatial resolution attained was ~ 0.2 " in transverse position and ~ 20 mr for angles. This was quite adequate for preliminary track reconstruction which was then refined by

including the momentum chamber measurements in the track fitting.

Shower counters

The final detection components of the apparatus were the fourteen shower counter modules placed immediately behind the shower chambers. Each consisted of a scintillator-lead-scintillator sandwich, the scintillator slab having dimensions 52" x 10" x 3/8". The lead sheet was two radiation lengths thick, so that electrons traversed a total of five radiation lengths of lead in the apparatus. This is shower maximum for 3.1 GeV/c electrons whereas electrons from the accepted K_{e3} 's had an energy spectrum which fell to zero at 2.0 GeV/c. The 28 scintillators were paired in front-rear pairs, with phototubes at opposite ends, and the summed signal from each pair was pulse height analyzed and stored on tape if the K_{e3} trigger was satisfied. It will be seen in the next chapter that this shower pulse height information was used before scanning to reduce the number of pictures looked at by a factor of 4.

As will be shown, this reduction took place by use of a complicated computer program. It would have been advantageous to apply this selection in real time to reduce the triggering rate. However, duplication of the program by electronics is a complicated problem in fast logic, and besides, one would not have the advantage of trial and error if one were to apply the selection in real time.

Magnetic tape recording

The spark chamber data were recorded by three cameras while the electronic data from the counters were stored on magnetic tape.

The two questions asked of the counters in the system were: (a) Digital -- which counters fired, and (b) Analog -- for certain counters, what was the amplitude of the pulse in the counter? In case (a) the fast logic output corresponding to the signal in question went to a buffer storage circuit (BS-1) from which it was read into a PDP-8 computer after the spark chambers had fired. For (b) the pulses were analyzed by slow pulse height analyzers (SPHA's) and then read into the computer in the same way as the BS-1 data. After several events had been accumulated the information in the computer was read out onto magnetic tape. A program, EXPO, controlled the movement of information through the PDP-8 and also histogrammed any desired quantity. These histograms could be observed directly on an oscilloscope while running and provided a very direct check on the performance of the apparatus.

This completes the description of the apparatus. A total of 900K pictures were taken in January-April 1968 of which 240K were with the K_{e3} trigger. The magnetic field was reversed twenty-five times during this data-taking period, with equal amounts of data taken at each polarity. A discussion of running procedures and checks on the stability of the apparatus is given in Appendix 9. The next chapter will discuss how these pictures and magnetic tape records were analyzed to obtain a sample of K_{e3} 's.

III. DATA ANALYSIS AND BACKGROUNDS

Of the 240K pictures taken, it was expected that $\sim 1.5K$ were good K_{e3} 's. This Chapter describes the filtering process which extracted these K_{e3} 's from the raw data and then discusses the background remaining in the sample. Such a process must be able to reduce the background level to $\sim 1\%$ and at the same time introduce no biases, with respect to decay length, on the accepted K_{e3} 's.

As usual, one started with the simplest and crudest selections available and then, with a smaller sample to work on, applied more complex and precise tests to the events. In this case, the first step involved qualitative selections designed to isolate neutral decays from other triggers (using the production-decay region pictures) and π -e from other final states (using the shower chambers and shower counters). To ensure that the π -e seen in the rear of the apparatus came from the decay seen in the front end, the surviving candidates were next measured and their trajectories reconstructed through the magnet. Quantitative selections could then be made on these measurements, e.g., only events that reconstructed reasonably were retained, mass cuts were made on different invariant mass combinations, etc..

This chapter is divided into four sections: (A) Scanning, (B) Measuring and event reconstruction, (C) Final selections and rescan and (D) Remanent background in sample.

A. Scanning

Examples of qualitative features that one would expect a priori of good $K^0 \rightarrow \pi e \nu$ events are:

- (a) A vee visible in production-decay region.
- (b) A showering track and a non-showering straight-through track in the shower chambers.
- (c) In the shower counters, a large pulse height for the electron and a minimum ionizing pulse for the pion.

The 240K triggers were examined for these features in the order (c), (b) and (a). This order was chosen since it went in order of increasing difficulty and sensitivity to biases, e.g., a scanning inefficiency in the decay region is much more direct in its effect on X than a pulse height dependent inefficiency in examining the pulse heights in the shower counters. Each of these steps will now be described and further details are contained in Appendix 10 on scanning procedures.

Tape Scan

The magnetic tape record for each K_{e3} trigger was analyzed by a computer program which examined the pulse heights in the fourteen shower modules and looked for a combination consistent with an electron and a pion. The pulse height distributions of electrons and non-showering tracks, identified in the shower chambers, are shown in Fig. 6. Fig. 7 shows the electron pulse height response for three regions of electron energy. It is clearly reasonable, the average response increasing with P_e although the distribution

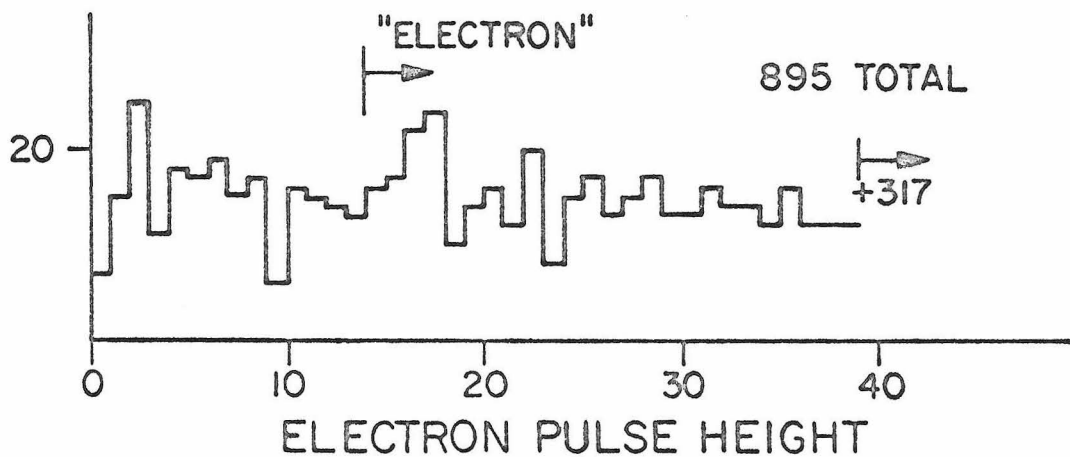
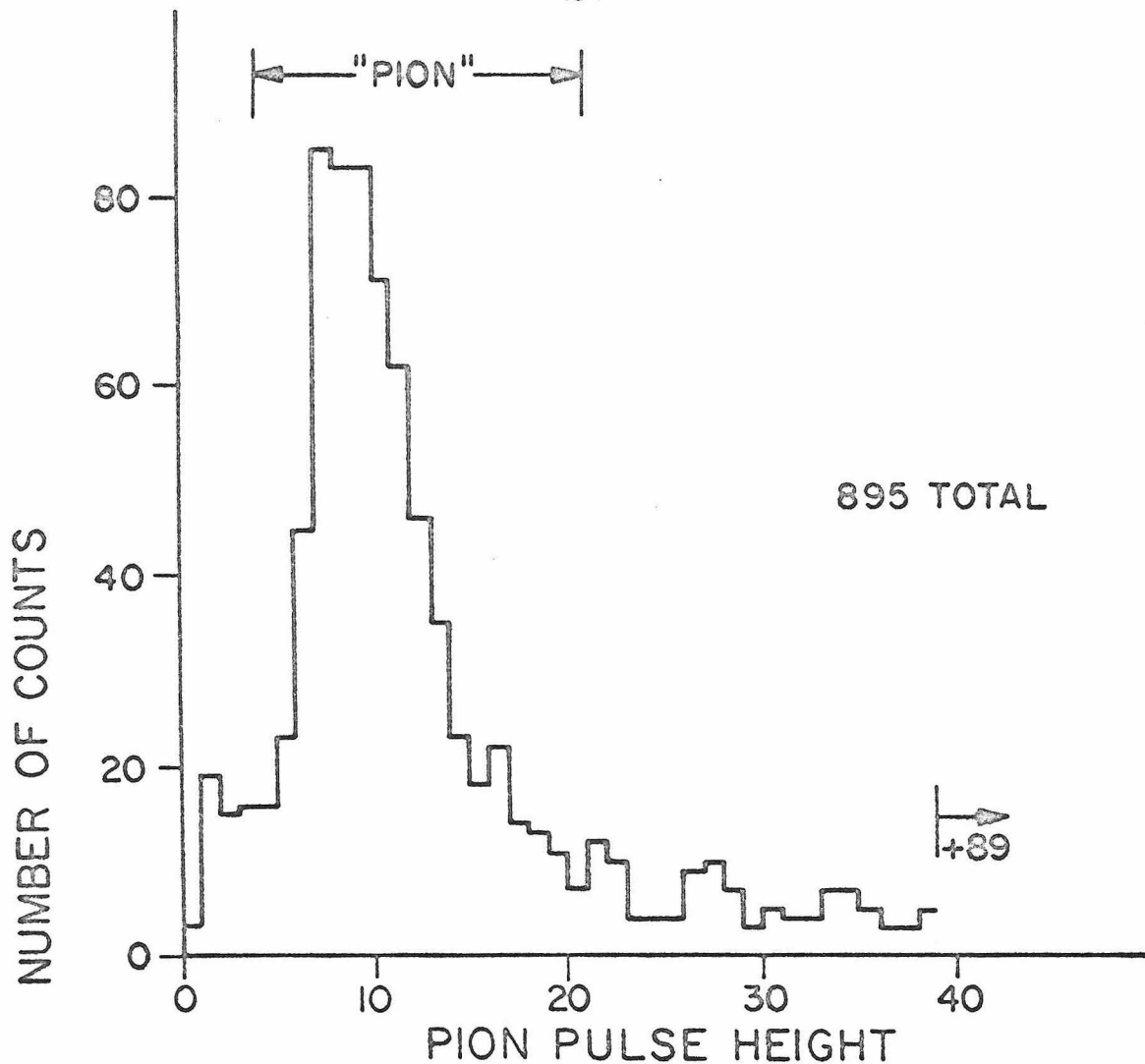


Fig. 6 Shower counter pulse height distributions of electrons and pions

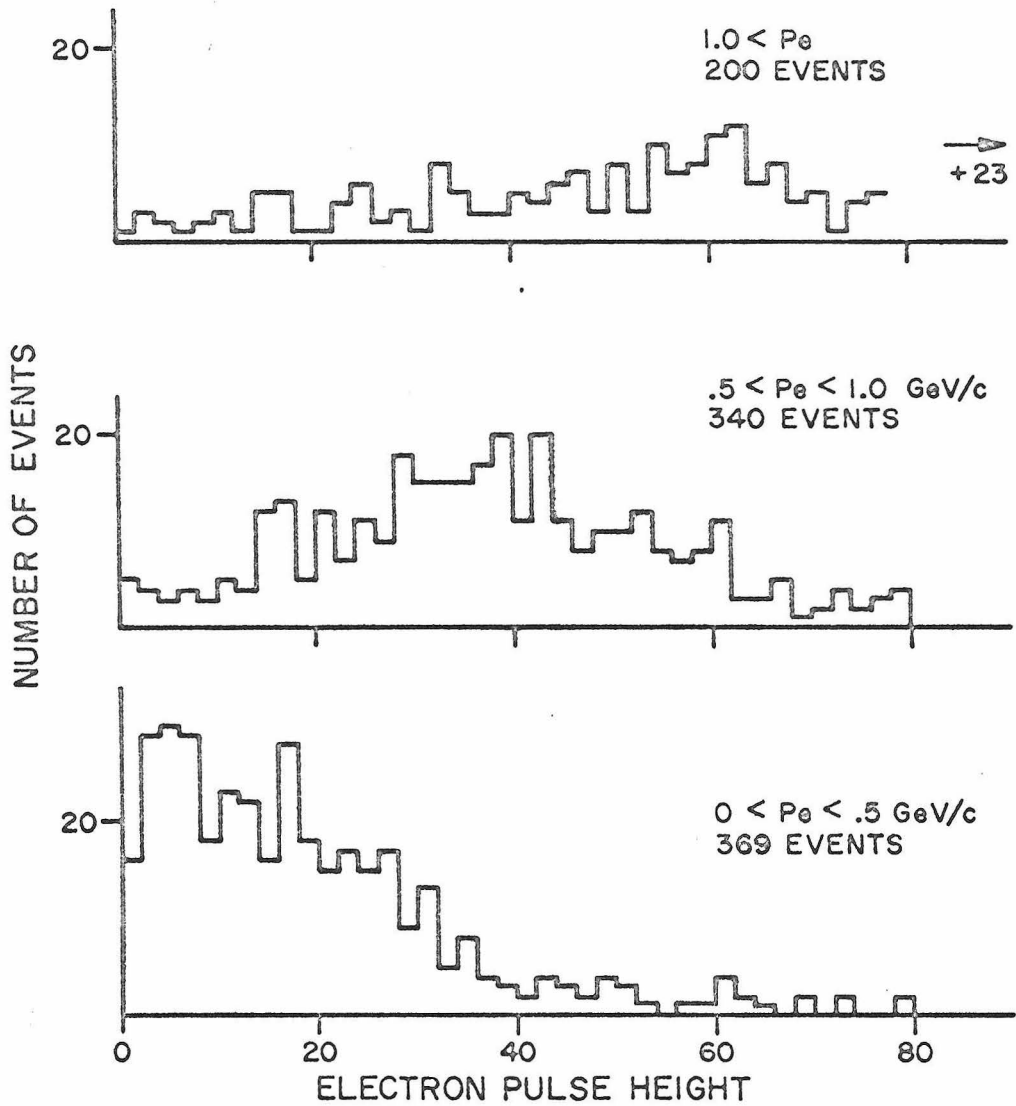


Fig. 7 Electron pulse height in shower counters for three electron energy regions.

broadens with energy. This latter effect is due to the fact that the shower counters sampled the shower at three and at five radiation lengths only and for higher energies, the effect of correlations increases.

In the computer scan, an "electron" was defined as a pulse height $> 1.7 I_{\min}$ in a pair of adjacent modules. A "pion" was defined as a pulse height between $0.5 I_{\min}$ and $2.6 I_{\min}$ in a single module with $< 0.6 I_{\min}$ in the modules on either side. For a given RH counter triggered, three pairs of shower modules behind it were searched for an "electron". If either RH counter in a trigger had an "electron" behind it, then three single modules behind each RH counter were searched for a "pion". The trigger was accepted if an acceptable "electron" - "pion" combination was found. If the RH counters for the trigger were within 4 RH counters of each other then the search for a "pion" was not made and the trigger passed the computer scan with just an "electron". Details of the tape scan and analysis of a sample event are given in Appendix 10. Events passing the tape scan had their serial numbers and other relevant information printed out in the form of a scanning list to be used in the next stage of scanning.

From a sample of 524 K_{e3} 's obtained without any pulse height selections, the tape scan accepted 396 events, giving an overall efficiency of 75%. This should be regarded as a lower limit because many of the 128 events missed are dubious, the K_{e3} sample being preliminary. A more crucial question is whether the

acceptance of the tape scan is a function of decay length or electron charge, thus biasing the K_{e3} time distributions. These matters are investigated in Appendix 10 and no evidence for any bias is found.

The tape scan accepted 67,205 out of the original 240,000 triggers.

Shower Scan

The 67,205 remaining candidates were scanned in the shower chambers for an electron and a non-showering particle. The triggering tracks were distinguished from other tracks by using the RH information which was on the scanning list and also visible on the film. The scanner simply found those tracks that were headed for the triggered RH counters using a scanning template, which had the rear hodoscope marked on it. The tracks were classified as " π " or "e" according to the criteria:

- " π " (a) Straight through track.
 - (b) Track scattering at a definite point, with straight segments.
 - (c) Track with an interaction where a number of straight tracks emanate from a definite vertex.
- "e" Any track which satisfies none of the " π " criteria and is not an obvious stop.

The criteria were kept simple and liberal -- the "e" criteria will accept many low energy pions and protons and many pion and proton interactions. However, the criteria have high efficiency

for good K_{e3} events and it was planned to have all final candidates rescanned by physicists in the shower chambers. If the picture had an acceptable " π " - "e" combination it was retained, events which were " π " - " π " were also accepted in a different sample to be analyzed in parallel with the πe sample. Throughout the thesis, this sample is referred to as the $\pi\pi$ sample but, of course, positive identification of the π was not made and such events could also be πp or $\pi\mu$. Most of the events rejected at this stage were $2e$ events which easily passed the tape scan.

The efficiency for K_{e3} 's was checked on an independently acquired sample and found to be 96%. Most of the events lost were cases where the pion had extra sparks along the track, leading the scanners to interpret the event as a $2e$ event.

One might well ask about the possibility of bias in the events lost. The most likely source would be a correlation between X_V , the decay length, and ΔZ_{Sh} , the horizontal separation of the e and π in the shower chambers, with the scanners tending to miss events when the e and π are beside one another. This matter is investigated in Appendix 10, and no correlation between X_V and ΔZ_{Sh} was seen. Another possibility is that the scanners missed low energy electrons. However, the electron energy spectrum does not change much with position in the front end so any bias would be second order. It was concluded that any dependence of the shower scanning efficiency on the decay vertex position was negligible.

The number of events accepted was 14,613 πe and 6,005 $\pi\pi$.

Production-decay Region Scan

The third phase of qualitative selection was to scan the decay region pictures for the two-prong vee characteristic of a neutral decay. Since the aim of the experiment is to measure the decay distribution of the K_{e3} decay, it is clear that this scan should be highly efficient so that any position dependent biases will be negligibly small. High efficiency was obtained by

- (a) leaving the scan until last so the scanners could spend more time on fewer pictures,
- (b) using the MH information to identify the triggering tracks in the decay region picture, and
- (c) having the pictures double scanned.

The MH information was used by having a template of the appropriate magnification with the MH marked on it. The scanner found those tracks which headed for the triggered MH counters, and the candidate was accepted if these two tracks formed a consistent vee in the plan and elevation views. The scanners noted in which plate the vee first appeared and this was used in comparing scanners and, later, in checking measurements. More details on the decay region scan are given in Appendix 10.

Vees with more than two prongs or with opening angles less than 2° were rejected. This opening angle cut was designed to reject electron-pairs, the major triggering background. From the Monte Carlo calculations, discussed in Chapter 4, it was determined that $(.06 \pm .03)\%$ of the K_{e3} 's have $\theta_{\text{opening}} < 2^\circ$, this fraction

increasing to 1% for $\theta_{\text{opening}} < 4^\circ$. Hence 2° is a safe cut to make, any possible bias being small.

Examples of triggers failing the production-decay region scan are

- (a) Scanner finds a vee, but one of its tracks is not directed at either of the triggered MH counters. Such triggers are probably due to a conversion outside the decay region or else an extra track, visible in the decay region, triggers an MH counter.
- (b) Scanner fails to find a vee anywhere in the decay region. A γ probably converted in S5 and then triggered the gas counter.
- (c) An electron pair (which does not separate into two distinct tracks) and an off axis beam track trigger the apparatus.

For the sample of K_{e3} 's finally accepted, the individual scanning efficiencies were $(96.4 \pm 0.5)\%$ and $(97.3 \pm 0.4)\%$ for the two scanners. The average individual efficiency as a function of decay position is shown in Fig. 8. There is clearly no systematic position dependence so that scanning biases are negligible. If there are no correlations between scanners, so that one is 97% efficient on the 3% missed by the other, then the overall efficiency of the double scan is 99.9%. Correlations were investigated using a previously acquired sample of K_{e3} 's and the double scan missed 1 event out of 300, consistent with the above overall efficiency. This does not close the question since there might be a class of patho-

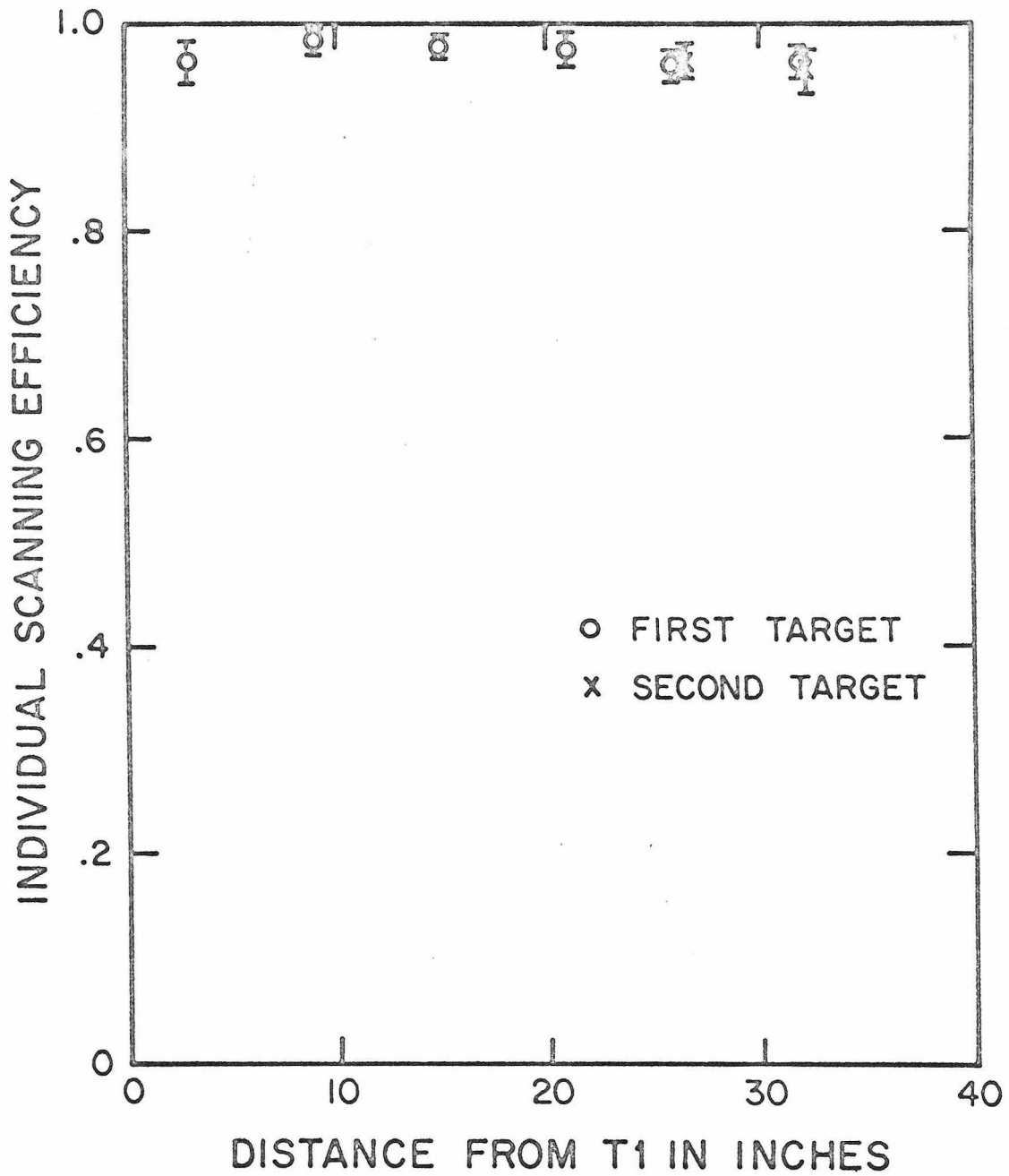


Fig. 8 Average individual scanning efficiency of production-decay region scan

logical events that all scanners would tend to miss. From knowledge of the efficiency of the spark chambers and the geometrical distribution of the K_{e3} vees, however, such low visibility vees can only form a minute fraction of the total.

The number of π -e events surviving this scan was 3,395.

B. Measuring and Event Reconstruction

It had to be established that the electron and the non-showering track identified in the shower chambers came through the magnet from the vee in the decay region and did not interact or scatter on the way. Before entering the shower chambers, the secondaries of a typical decay in the front end had encountered 12.4% of a radiation length, 6.2% of a collision length and lost 6.7 MeV of energy if they were minimum ionizing. To check the continuity of tracks, the 3,395 surviving candidates were measured and the decay secondary trajectories reconstructed in space. The reconstruction was first done using only the decay region and shower frames. Events which fit reasonable trajectories through the magnet were then measured in the momentum chambers and the fit repeated, using this extra information. Details of the measuring and reconstruction process are given in Appendix 11 and only features affecting the analysis directly are included here.

The pictures were measured with digitized protractor measuring machines, digitizing the angle and the position of some point on the track. The resolution on the measuring tables was ± 0.01 " in position and 1 mr. in angle. In real space, this corre-

sponded to $\pm 0.03''$ for position measurements and, again, 1 mr. for angular measurements. The angle and the two coordinates were each encoded and digitized into 5-digit decimal numbers and punched on cards by an IBM 526 Summary Card Punch.

In the decay region picture, the incoming beam track and the two decay prongs had their angles and positions measured in the plan and elevation views; in the shower chambers, the two triggering tracks were measured in the plan and elevation views and the electron was identified. These measurements were then analyzed by a checking program which verified by reconstruction that the tracks were consistent with the MH and RH counters triggered by the event. This check actually duplicates the MH and RH checks in the decay region and shower chamber scans. However, it was very useful in isolating events where the scanner or measurer had made a bookkeeping or measuring error. The decay vertex positions calculated by the program were checked for consistency between the plan and elevation views and also checked against the plate number noted by the decay region scanner. These checks were effective at finding mismeasurements and such events were remeasured and passed through the program again. Three passes through this program were sufficient to clean up incorrect digitizations.

The measurements were then combined with the PDP-8 data tape record and analyzed by a track reconstruction program. A preliminary test was made to see if a line, drawn between the points digitized in the decay region and the shower region, intersected the

the triggered MH counters within a certain tolerance. This check is more demanding than the MH check previously mentioned because it ties together information in the decay region and the shower region by interpolating between them, whereas the previous check merely extrapolated from the decay region to the MH. Tracks which headed for the triggered MH counter, but subsequently scattered in the vertical direction, for example, would fail this test. Events outside the tolerance, $\sim 23\%$ of the total, were removed from the sample. The successful tracks were fit to orbits in the magnetic field and constrained to intersect at a unique vertex in space. This procedure found reasonable fits for 76.5% of the measured events, the remainder almost all failing the MH test. The distribution of χ^2 for a track is shown in Fig. 9 for all tracks; there were three degrees of freedom per track.

All events for which the χ^2 of each track was less than 100 were then measured in the momentum chambers. The momentum chamber measurements were checked for consistency with the MH and RH counters and mistakes corrected. These measurements, along with the results of the decay region-shower reconstruction, were submitted to a fitting program and the trajectory fit performed using all chambers in which the track was visible. This more refined fit used up to five segments of the track, whereas the previous fit used only two. The tracks were constrained to a unique vertex in space, as before. If the fit could be improved by dropping any of the chambers (except the decay region, which was needed to reconstruct the vertex),

then this was allowed.

The geometrical reconstruction was checked using a large sample of straight through tracks, photographed with the magnetic field off. The momentum fitting procedure was checked with $K_S \rightarrow \pi^+ \pi^-$ and $\Lambda \rightarrow p \pi$ events, from calibration data, by looking at the K and Λ masses calculated for the 2-body decays. Fig. 10 shows histograms of these masses separately for each target from a sample of successfully reconstructed calibration events. $M_{p\pi}$ is the invariant mass calculated assuming that the positive particle is a proton, the negative a pion. The distribution in this quantity is shown for all events. Then a cut of $M_{p\pi} > 1.160$ GeV is imposed and the $M_{\pi\pi}$ distribution of the remaining events shown. This order was chosen since the K-background under the Λ peak is less than the Λ background under the K-peak. Almost all events are consistent with K or Λ decay.

Fig. 11 shows a histogram of $\chi^2/\text{degree of freedom}$ for all tracks of the πe sample. This quantity, rather than χ^2 , is plotted, as the number of degrees of freedom in the fit depends on the number of chambers from which measurements were used in the fit. This plot shows that for good tracks above the flat background, the assigned errors in the reconstruction program were reasonable. The flat background contains, for example, tracks which interacted in the apparatus and poor fits resulting from attempts at fitting uncorrelated tracks to the same trajectory.

Fig. 12 shows a histogram of the difference in vertex position along the beam, as calculated by the fitting program (X_{fit})

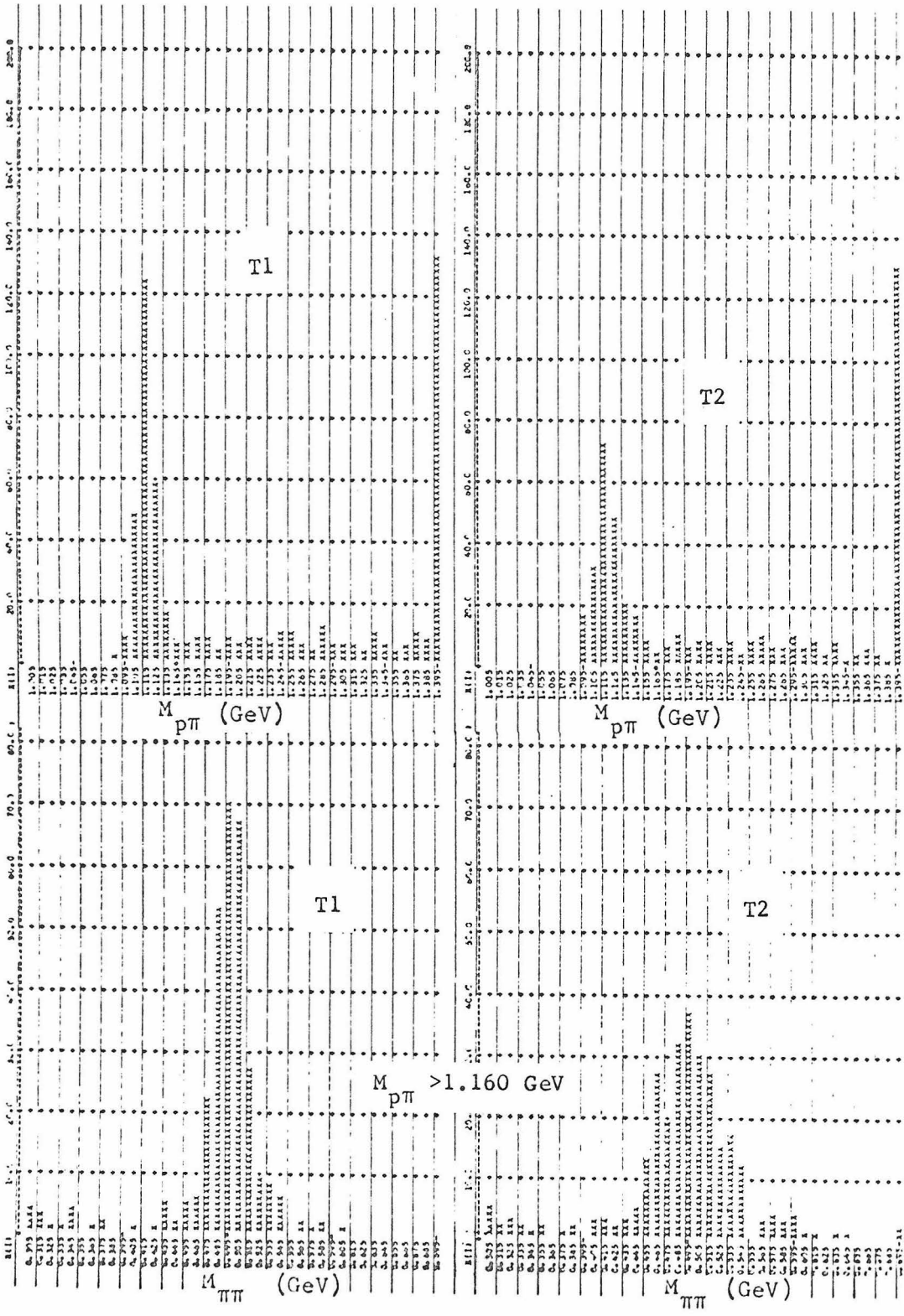
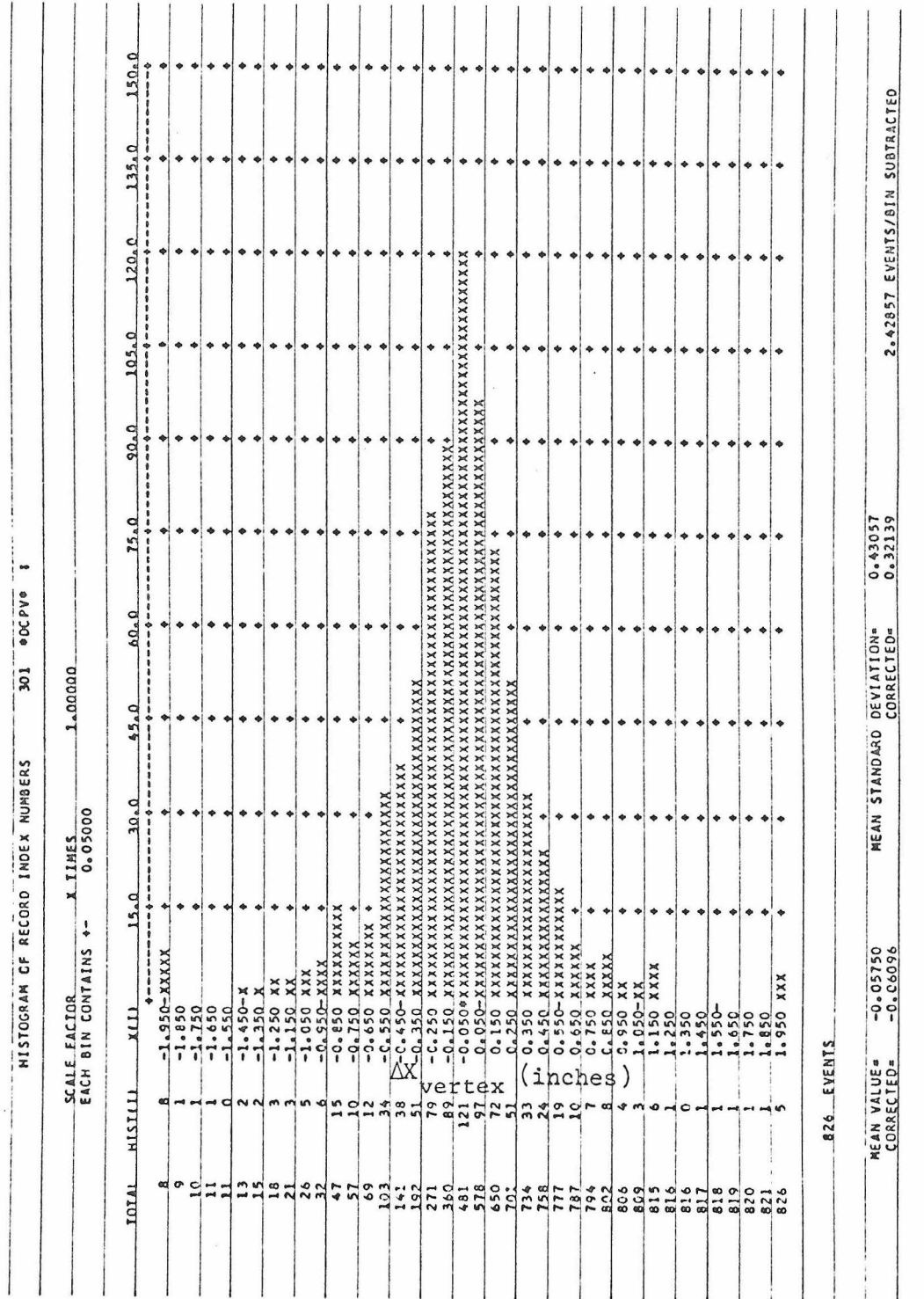


Fig. 10 $M_{p\pi}$ and $M_{\pi\pi}$ distributions from each target

06/01/70



5 EVENTS GREATER THAN MAXIMUM
8 EVENTS LESS THAN MINIMUM

Fig. 12 Distribution of $\Delta X_{\text{vertex}} = (X_{\text{plate}} - X_{\text{fit}})$

and as determined from the plate number estimate of the decay region scanner (X_{pl}). The sample in the histogram is that obtained after the cuts of section (C) of this chapter. The width of the distribution implies that the resolution in longitudinal vertex position is $\leq .3''$, which is what was expected from the transverse position and angular resolutions.

Of the 3,395 K_{e3} candidates measured, 2,226, i.e., $\sim 66\%$, reconstructed reasonably. Of the 34% rejected, 23% were previously removed by the MH interpolation test. The remaining 11% were events where the χ^2 of either track was greater than 100 in the front end-shower fit. Some of these events were traced by hand, and it was seen that the separate track segments were at angles such that a single orbit could not fit the segments consistently. Such events arise from scattering in the horizontal direction or from fitting track segments of different particles to the same orbit.

The discussion will next center on the selections made to obtain the final sample used to fit the K_{e3} time distributions.

C. Final Selections

Fig. 13 shows e^+ and e^- decay position distributions from each target for the 2,226 events which survived the reconstruction. It is evident that there is a substantial charge asymmetry, characteristic of a K_{e3} signal if $|X| \lesssim .2$. This meant that the background was at a fairly low level and it remained to make the final selections to reduce it even further. It consisted of two basically different kinds of background:

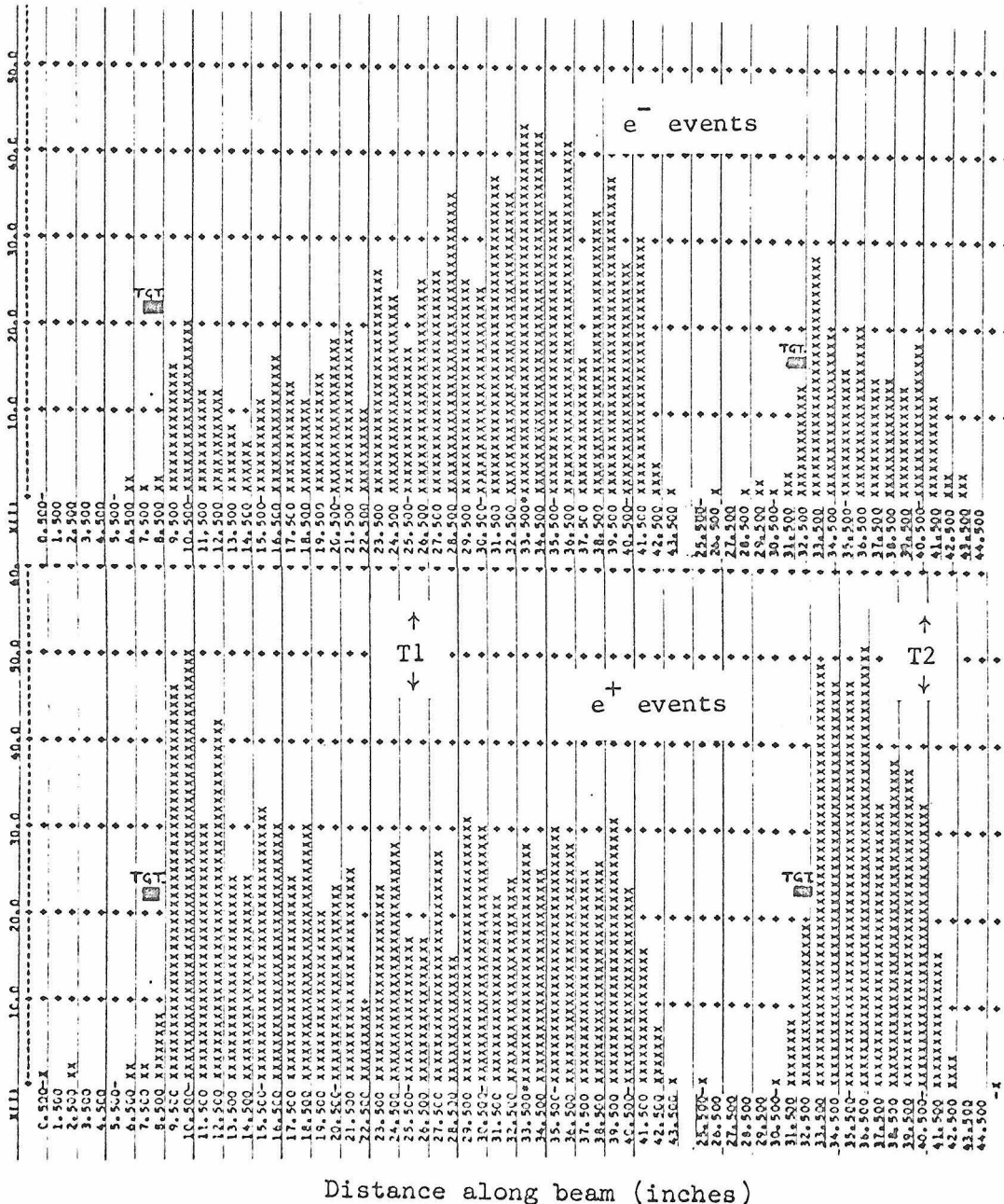


Fig. 13 Decay position distribution of all events passing reconstruction

- (a) Events which still show features in their reconstruction, not characteristic of tracks continuous through the magnet aperture.
- (b) Events where the " π " and "e" in the shower chambers both come from the vee in the front end without interaction or scattering, but where the " π " or the "e" is misidentified, i.e., the event is really 2π or $2e$.

To reduce (a) and (b), quantitative cuts were first imposed and then all survivors were rescanned in the shower and decay region chambers.

Quantitative Cuts

The following seven cuts were imposed on the 2,226 remaining candidates. Of these cuts, discussed below, (1) - (5) were directed at eliminating (a), while (6) and (7) were aimed at (b).

- (1) Charged prongs were required to be contained within the production-decay chambers over their length because if they exit through the sides they would encounter an excessive amount of material. This requirement was actually imposed at the scanning level for later data so it is not meaningful to quote how many measured events were rejected by it. It is clearly a reasonable cut, particularly since, on one side, an exiting particle would encounter the dense material of the spark chamber electrical hardware.
- (2) From the Monte Carlo calculations of the electron and pion momentum distributions (Fig. 24, in Chapter 4), it can be

seen that there are few events with either secondary momentum above 2.0 GeV/c. A cut at 3.0 GeV/c is reasonable and any decay secondary with a momentum > 3.0 GeV/c is probably a result of a scattering which gave a smaller apparent bending angle.

- (3) The reconstructed position at the MH and RH counters was required to be within one counter of the triggering counters. The MH and RH information has already been exploited in checking the tracks. However, for a small number of events, it was possible for the vertex fitting procedure to move the orbit outside the counter in its attempt to find a unique vertex in space. If the reconstructed orbit is consistent with the orbit actually followed by the particle, then the MH and RH counters intersected by it should be those triggered by the event. The resolution for this was determined by looking at the distance of all reconstructed tracks from the center of the triggered counter, in the appropriate dimension. This requirement demanded that the reconstructed track be no more than 1" from the edge of the triggered MH counter and no more than 3" from the edge of the triggered RH counter.
- (4) The χ^2 per degree of freedom of all tracks in the sample was required to be less than 5.0. From Fig. 11, where this quantity is histogrammed, it is evident that a cut at 5.0 is conservative for the signal which peaks at 0.8.

- (5) The tracks were required to have opposite charges since it was impossible to tell which charge was wrong when an event came out of the fit with both secondaries having the same charge.
- (6) The pulse height of the electron shower in the shower counters was required to be greater than 1.2 times minimum ionizing. Now that the electron trajectory was exactly known from the reconstruction, its position at the shower counters could be calculated and the pair of counters containing the shower known precisely. This requirement simply demanded that the pulse height in these counters be consistent with the computer scan. π - π events, where a low energy pion was accepted as an electron, would tend to fail this test.
- (7) The gas counter trigger configuration was required to be consistent with the orbits of the electron and pion. The counter had two mirrors, each reflecting light into a set of three phototubes, and the pulse height of each set was separately recorded. Most orbits had the electron shining its Cerenkov light into one side only and for these it was demanded that the pulse heights be consistent with the orbits. Electron orbits were chosen for which the tangent at any point of the trajectory, when extended to the plane of the mirrors, did not intersect within 1.0" of the other mirror. For such events, it was demanded that (a) the side

receiving the Cerenkov light have pulse height > 0 and that its BS-1 bit be on (see Appendix 5), and (b) that the pulse height of the side not receiving Cerenkov light be < 3 . or its BS-1 bit be off. This test removed $e^+ - e^-$ events where the electrons were separated enough to shine on opposite sides and $\pi^+ - \pi^-$ events where one of the pions was considered an electron in the shower chambers but the opposite side of the Cerenkov counter had the trigger.

Table 2 shows the number of events removed by each of these cuts separately and also the number removed by one cut, but passing all others. Selection (1) is not included in this table. These cuts reduced the sample to 1,673. Decay position distributions of the 553 events removed are shown in Fig. 14.

Shower Chamber Rescan

In order to establish conclusively that the two tracks in the shower chambers were those of a $\pi e(\rho e)$ event and to reduce backgrounds of type (b), the 1,673 candidates were looked at by a physicist who had access to all parameters of interest from the computer reconstruction of the event. The appearance of the electron and the pion was carefully scrutinized. The electron was scanned for any large angle tracks characteristic of a strong interaction, the pion for excessive multiple scattering which is characteristic of low energy electrons. The shower counter pulse heights were next checked to see if any extra tracks actually gave a pulse height in the counter into which the track extrapolated. If so, it could be in

TABLE 2. EFFECT OF QUANTITATIVE SELECTIONS ON THE π -c SAMPLE

Rejection Criterion	Total rejected for this reason	Number which would get into final sample if this cut were dropped but all others kept
$\chi^2/\text{d.f.} > 5$, (4)	129	25
Same charge (5)	111	9
Either momentum greater than 3.0 GeV/c (2)	65	6
Misses MH by more than $\frac{1}{2}$ counter (3)	52	3
Misses RH by more than $\frac{1}{2}$ counter (3)	106	7
Electron pulse height < $1.2 I_{\text{min}}$ (6)	124	8
GC pulse height incon- sistent with orbits (7)	163	16

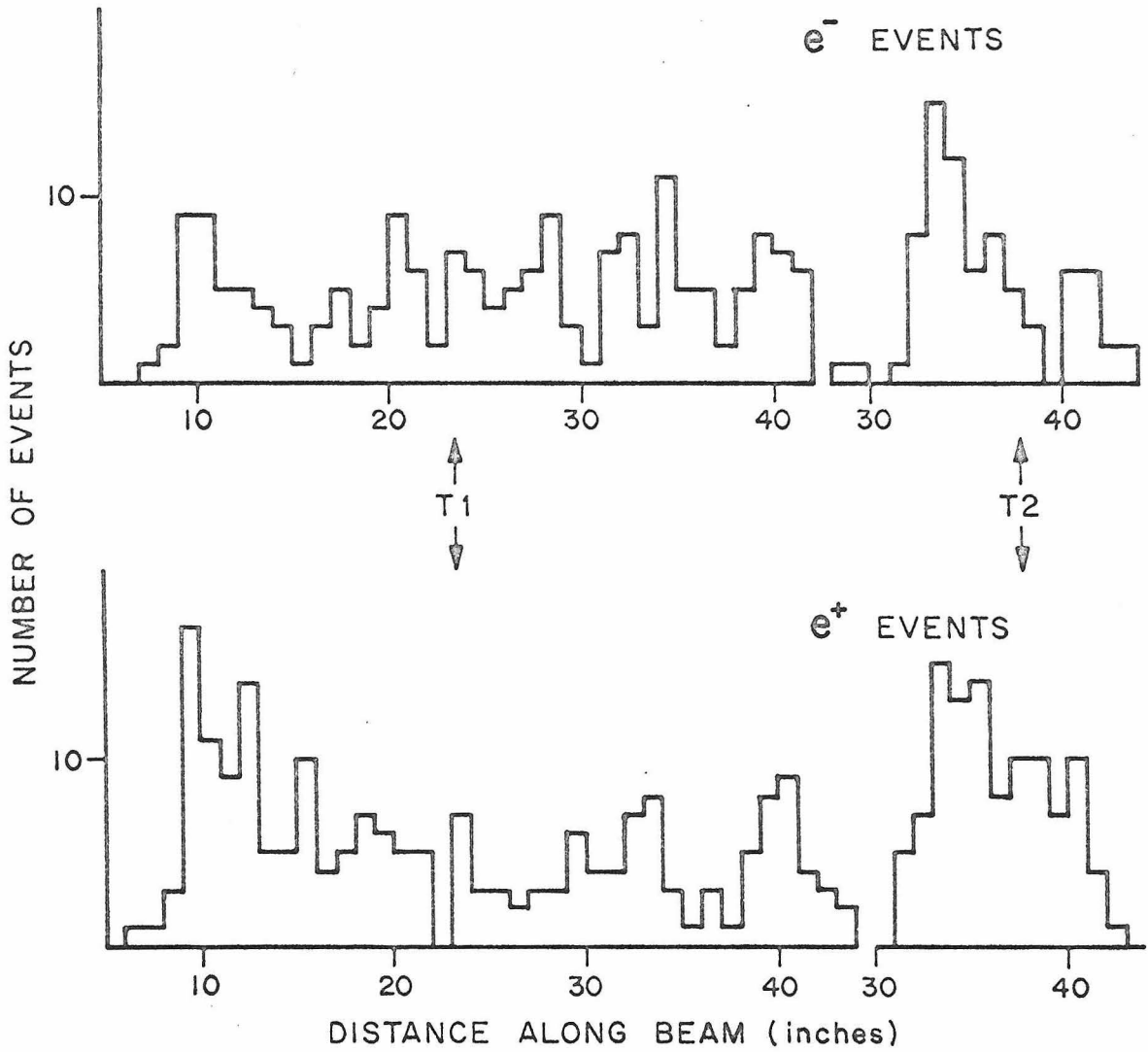


Fig. 14 Decay position of events rejected by quantitative selections (1)-(7)

coincidence with the π -e and the event was rejected since the extra track could be due to the secondaries interacting on their way through the apparatus. Most of the extra tracks visible were, of course, within the 500ns. live time of the shower chambers, but usually not within the 50ns. gate opened for the shower counters. As a result of this scan, 289 events were removed from the π -e sample, some of which were put into the 2π sample. Fig. 15 shows the decay position distribution of these rejects for each charge state and each target. There is clearly not much asymmetry between e^+ and e^- indicating that the rejects are largely background.

Decay Region Rescan

All remaining candidates were examined in the production decay region by a physicist. Dubious vees or events with more than 2 prongs from vertex were removed. A total of 47 events were rejected leaving 1,337 in the sample.

D. Estimation of Remanent Background.

In this section the following backgrounds will be considered:

- (1) Neutron stars
- (2) $K_S \rightarrow \pi^+ \pi^-$, $\Lambda \rightarrow p \pi^-$
- (3) $e^+ - e^-$ pairs
- (4) Λ β -decay ($\Lambda \rightarrow p e^- \bar{\nu}$)
- (5) \bar{K}^0 - production in the targets

1. Neutron Stars

The material density in the decay region was kept low to

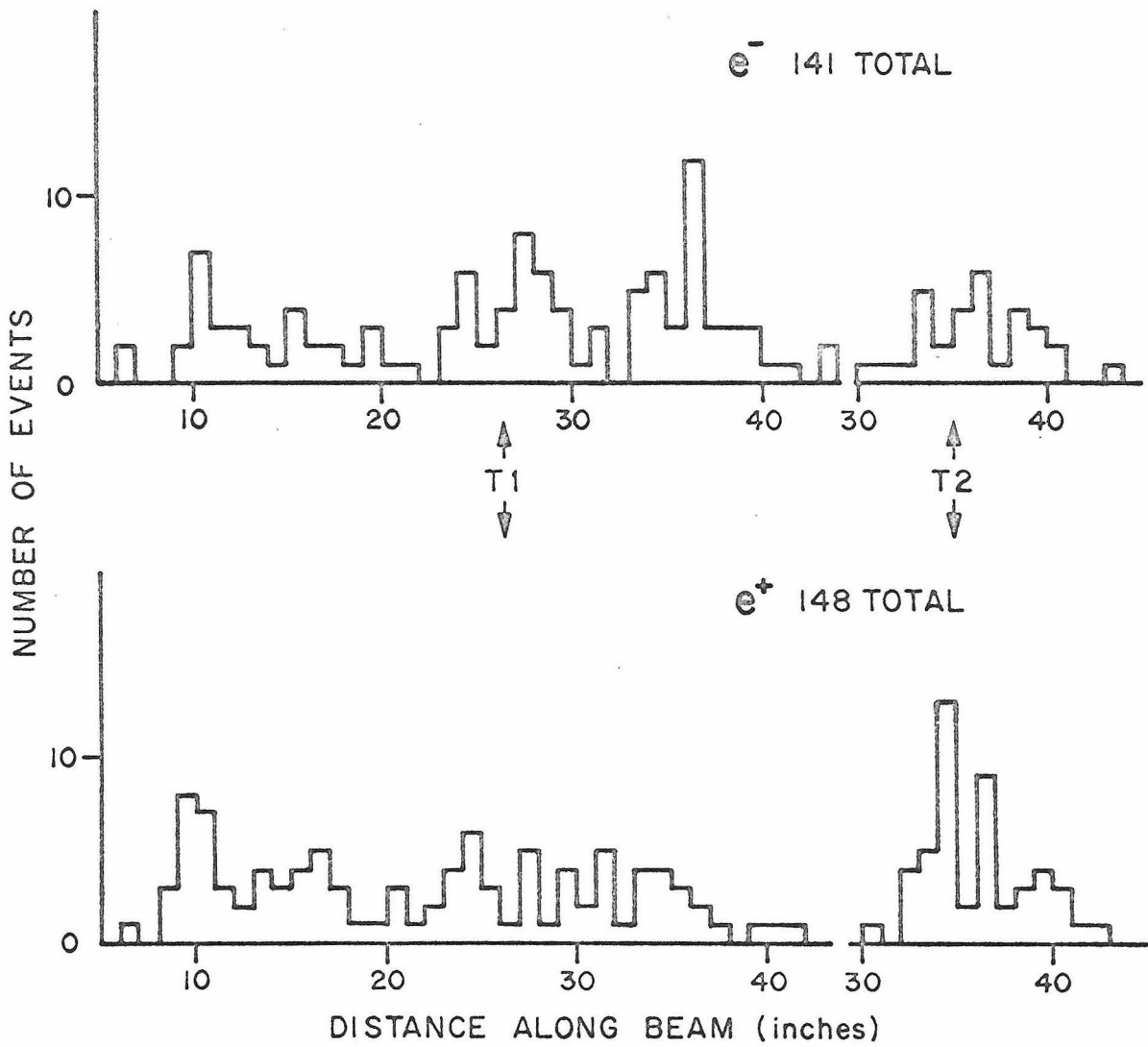


Fig. 15 Decay position distributions of events rejected in shower chamber rescan.

avoid background from neutron stars and γ -conversions. The material was mostly aluminum with some epoxy and mylar gas seals. It corresponded to .003 collision lengths and .01 radiation lengths per K_S lifetime. In order for a neutron to produce an event in the final sample, the vee must contain an electron and a pion with no visible evidence for another electron. The two charged prongs must in addition be energetic enough to get through the magnet ($p \gtrsim 150$ MeV/c). As an experimental check that neutron stars were not a background in the final sample, it was determined that the excess of accepted vees, produced in the first target, that appeared to decay inside the second target was 0.5 ± 2.0 events. By extrapolating to the spark chamber volume, correcting for relative densities and solid angles, the total neutron star background from the spark chamber plates was estimated to be 0.05 ± 0.20 events per K_S lifetime. This gives about 1.0 ± 3.0 events from all material in the decay region in the final sample. In the data used to fit the time distributions it was required that a space of at least one spark chamber gap separate the target veto counter from the visible decay vertex. This excluded any events which might have materialized in the veto counter.

$$2. \quad \underline{K_S \rightarrow \pi^+ \pi^-, \Lambda \rightarrow p \pi^-}$$

$K_S \rightarrow \pi^+ \pi^-$ and $\Lambda \rightarrow p \pi^-$ have decay rates 10^3 times that of $K \rightarrow \pi e \nu$ and to reach a background level of 1%, it is necessary to have a rejection ratio of $\sim 10^5/1$. This rejection came from three sources:

- (a) Gas Cerenkov counter, used in the trigger.
- (b) Shower counters, pulse heights examined in the computer scan.
- (c) Shower chambers, scanned for an electron.

In more detail:

- (a) The gas counter was used in the trigger as described in the last chapter. The pulse height threshold was set as low as possible, just above the noise. From the number of $K_S \rightarrow \pi\pi$ in the K_{e3} trigger relative to the number in the more general calibration trigger, where GC was relaxed, the rejection of the gas counter was estimated to be $(69 \pm 7)/1$.
- (b) The computer scan discriminated against $\pi\pi$ and $p\pi$ final states since, without interacting, these would give two minimum-ionizing pulses in the shower counters. If the RH's were separated by more than four counters, there would not be a pulse height acceptable as an electron to the program. From a sample of $K_S \rightarrow \pi^+\pi^-$ and $\Lambda \rightarrow p\pi^-$ picked up in the general trigger, it was calculated that the rejection of the computer scan was $(3.7 \pm 0.3)/1$.
- (c) The visual shower scan gave the largest rejection of the three. A series of runs with the general calibration trigger was scanned and measured with no requirements on the appearance of tracks in the shower chambers. Events were chosen which had invariant masses consistent with either $K_S \rightarrow \pi^+\pi^-$ or $\Lambda \rightarrow p\pi$ hypotheses and these were scanned

for πe by the same criteria used in the K_{e3} shower scan. A total of four events survived from a sample of 584, giving a rejection of $(146 \pm 73)/1$.

The fact that the rejections (b) and (c) may not be independent has to be taken into account if the three are combined to find the overall rejection. For example, a pion which is shower-like in the shower chambers is likely to give a big pulse in the shower modules. So the overall rejection will be a bit less than the product of (a), (b), and (c) which is $(3.7 \pm 2.0) \times 10^4$. However, there are more direct ways of estimating the K and Λ background, as will now be seen, and the preceding was just to give a feeling for the discrimination of the apparatus against this background and show that it had the correct order of magnitude.

Direct measurement of the K and Λ backgrounds was performed by comparing the π -e sample to the π - π (π -p) sample collected in the shower chamber scan. Fig. 16 shows comparisons of different distributions for these two samples. The π - π events peak at low GC pulse height and have prominent K and Λ mass peaks, whereas the π -e events have a broad GC distribution and show no evidence of K or Λ peaks. In order to measure the small K and Λ contamination in the π -e sample, it was necessary to make selections which enhance such backgrounds. This was done as follows:

- (a) Select events with GC pulse height ≤ 8 , and
- (b) select events with decay lengths $\leq 10''$.

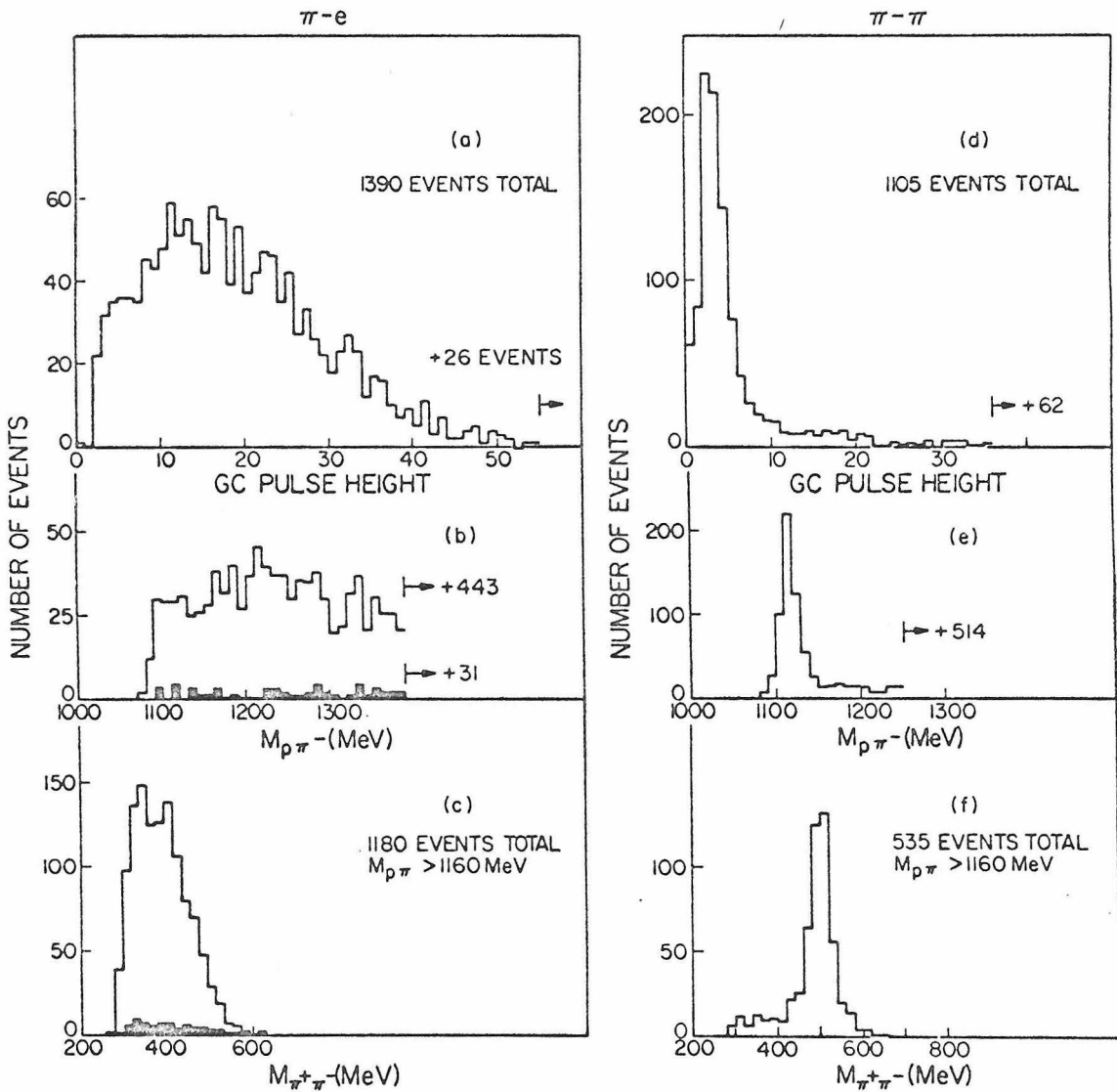


Fig. 16 Comparison of π e sample with $\pi\pi$ sample. The shaded events have GC < 8 and are within the first two K_S lifetimes. The absence of events with pulse height < 2 in (a) and (d) is due to the trigger bias.

Sixty percent of $\pi\pi$ events satisfy (a) and (b), whereas only 2% of the π -e events fall in this region, giving an enhancement factor of 30. Histograms of $m_{\pi\pi}$ and $m_{p\pi}$ for such π -e events are shown as shaded histograms in Fig. 16. It is reasonable to assume that the mass distributions of good π -e events satisfying (a) and (b) are the same as those for the total sample, since there are only weak correlations between mass and GC pulse height or between mass and decay length. Using this assumption, a subtraction was made to isolate whatever $K \rightarrow \pi\pi$ or $\Lambda \rightarrow p\pi$ signal was present. For the $m_{p\pi}$ spectrum an excess of (-3.1 ± 4.3) was found in the Λ region and for $m_{\pi\pi}$ an excess of (7.8 ± 4.3) in the K region, giving a total of (4.7 ± 6.1) events. Since the procedure is 60% efficient on background, this leads to a total background in the sample of (7.8 ± 10.0) events. This number was independently estimated from the total number of $\pi\pi$ events picked up in the K_{e3} trigger (after the tape scan) and the measured rejection of the shower chambers. This gave $1164/(146 \pm 73) = (8 \pm 4)$ events, consistent with the (7.8 ± 10.0) estimated above.

The K, Λ background can be reduced further by a factor of 3 by demanding GC pulse ≥ 8 simultaneous with $m_{p\pi} > 1160$ and $m_{\pi\pi} < 440$. The sensitivity of X to this cut will be discussed in the next chapter.

3. Electron Pairs

This background falls into two categories:

- (a) External conversions: $\gamma + Z \rightarrow e^+ + e^- + Z$
- (b) Dalitz conversions: $K_S^0 \rightarrow \pi^0 + \pi^0$, followed by

$$\pi^0 \rightarrow e^+ + e^- + \gamma.$$

For (a) and (b) the expected invariant mass distributions of the electron pair peaks at very low mass. Fig. 17 shows the invariant mass distribution of the π -e sample under the hypotheses that both charged particles are electrons. For comparison, the $m_{e^+e^-}$ distribution is shown for events taken with a 0.25 radiation length lead converter placed in the decay region and where the two charged particles in the shower chambers showered (process (a)). The shape of the latter implies that there are ≤ 9 events from process (a) in the uncut sample. A cut of 30 MeV on $m_{e^+e^-}$ reduces this background by 30.

Data taken with the lead converter were scanned in the shower counters and shower chambers like real data to determine the rejection of the π -e scanning for $e^+ - e^-$ pairs. It was determined that the rejection of the scanning on $e^+ - e^-$ pairs was $(43.5 \pm 11.3)/1$. Using the Monte Carlo program (described in Chapter 4), it was calculated that 880 events of type (b) would be in the final π -e sample with no shower or mass selections. Using the shower rejection of 43.5, this number reduces to 20 Dalitz conversions before cuts on $m_{e^+e^-}$. A cut at 30 MeV reduces this to 12. In order to demonstrate sensitivity of the final result to such background, a cut of 60 MeV can be imposed to reduce it further by a factor of 4.8, as will be done in Chapter 4.

4. Lambda Beta Decay

$\Lambda \rightarrow p + e^- + \bar{\nu}$ gives e^- events at early times where $X = 0$

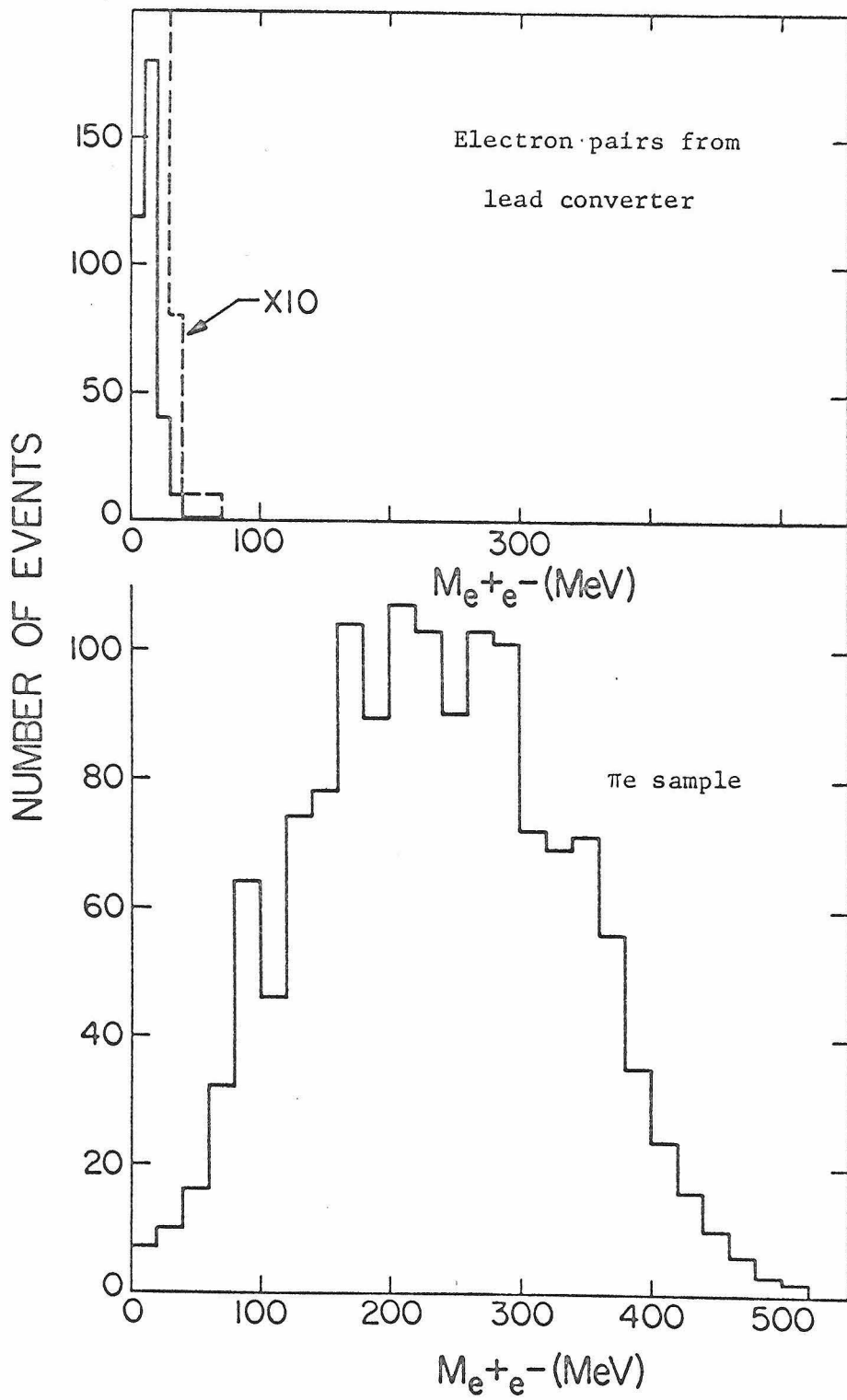


Fig. 17

$M_{e^+e^-}$ distributions from lead converter and πe sample

predicts few events. Fig. 18 shows the distribution of m_{ep} for e^+ and e^- events, for decay lengths $< 5''$ to enhance the Λ_β signal. This signal was expected to be visible in the n_{e^-} distribution for $m_{ep} < 1115$ MeV. The n_{e^+} distribution was used to calculate the number of events with $m_{ep} < 1115$ MeV if there were only K_{e3} 's in the n_{e^-} distribution, with no Λ_β contamination. A subtraction was then made as follows:

$$n_{\Lambda_\beta} = n_{e^-} (< 1115) - n_{e^-} (> 1115) \cdot \frac{n_{e^+} (< 1115)}{n_{e^+} (> 1115)}.$$

Inserting numbers from the histograms gave $n_{\Lambda_\beta} = 14 \pm 4.5$.

Correcting for the fact that the histograms are for the first $5''$ from each target, this gave a total of 19 ± 6 Λ_β events in the π sample. To ensure that this background was eliminated, it was required that $M_{ep} > 1115$ MeV, the maximum p-e mass possible in Λ_β decay. The cut was imposed on both charge combinations to preserve charge symmetric treatment of the data.

5. \bar{K}^0 - production

It was estimated from π^-p bubble chamber data⁽²¹⁾ that the total cross section for \bar{K}^0 - production is less than 10% of K^0 - production at 2.85 GeV/c. The momentum distribution of the \bar{K}^0 will peak somewhat lower than the K^0 and its angular distribution will be less peripheral. From the acceptance of the apparatus as a function of K^0 - momentum and angle, it was estimated that the average relative acceptance of \bar{K}^0 to K^0 into the apparatus was $< 10\%$. This

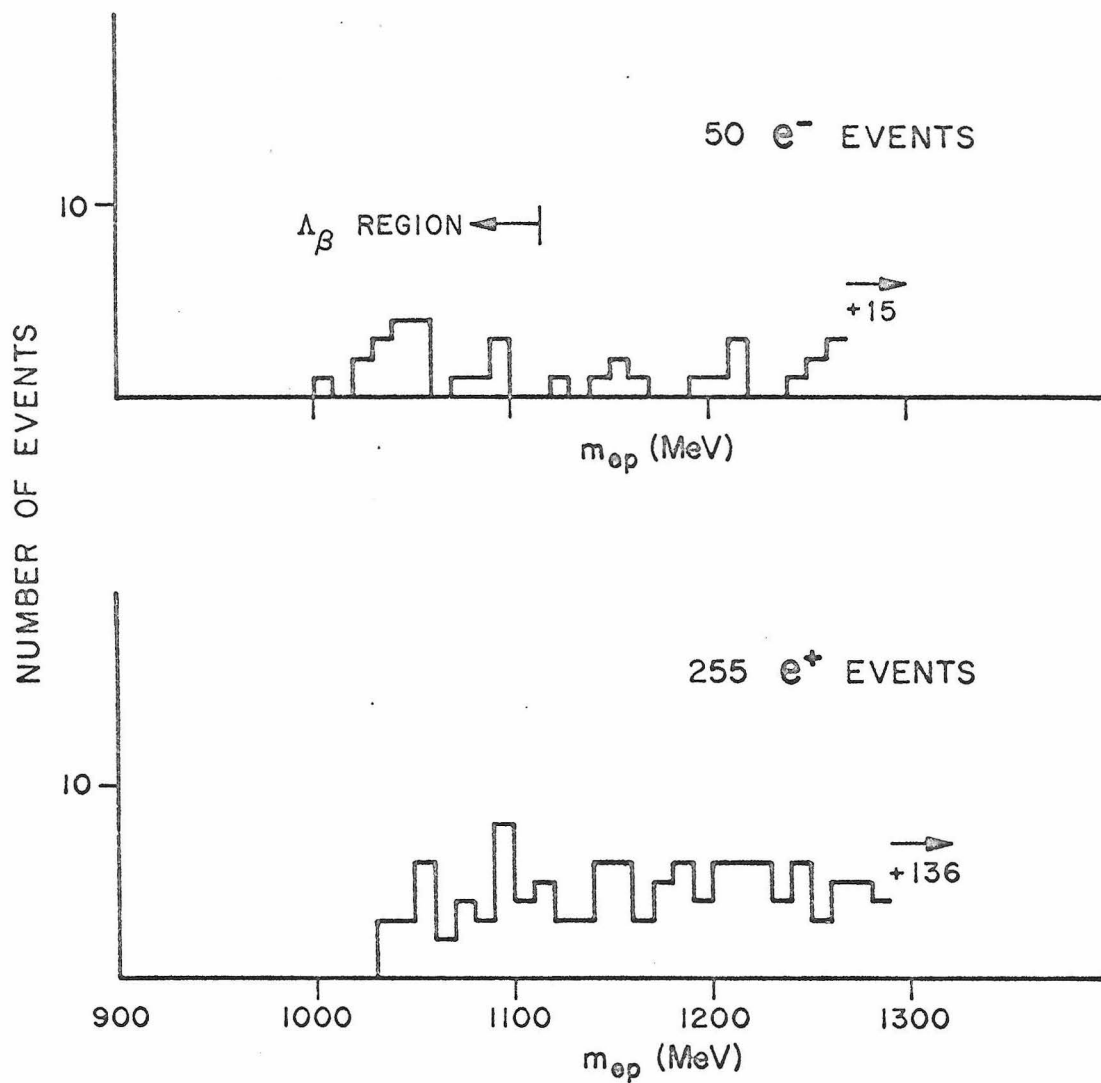


Fig. 18 m_{ep} distributions for e^+ and e^- events with decay lengths $< 5''$

means that less than 1% of the K_{e3} data came from pion production of \bar{K}^0 . As mentioned in Appendix 2 on the pion beam, the K^- contamination in the beam was measured to be $\sim 0.1\%$ of the pion flux. $\sigma(K^- p \rightarrow \bar{K}^0 n)$ is estimated to be $500\mu\text{b}$.⁽²²⁾ whereas $\sigma(\pi^- p \rightarrow K^0 \Lambda) \sim 100\mu\text{b}$. at 2.85 GeV/c. This means that $\sim 0.5\%$ of the events come from K^- - produced \bar{K}^0 . This gives an overall limit of 1.5% to the \bar{K}^0 - production fraction. As will be seen in Chapter 4, when a fit is made with the fraction of initial \bar{K}^0 relative to K^0 as a free parameter, the 3-parameter fit gives \bar{K}^0 - fraction = $0.6\% \begin{matrix} +1.9\% \\ -0.6\% \end{matrix}$, consistent with the above estimates.

In summary, the following background-reducing cuts have been made in this section:

- (a) $M_{ep} > 1115$ MeV, 163 events fail.
- (b) $M_{ee} > 30$ MeV, 8 events fail.
- (c) At least one spark chamber gap visible upstream of the decay vertex, 34 events fail.

The total number of events after these cuts was 1,137; a summary of the background analysis is contained in Table 3.

This Chapter has shown how a sample of K_{e3} events, with background $< 2\%$, was obtained between 0.2 and 7.0 K_S lifetimes. It remains to calculate the acceptance as a function of decay length for these events and to fit them with the parameter X.

TABLE 3. BACKGROUNDS IN THE π -e SAMPLE

Type of Background	Number present before cut	Cut imposed on final sample	Estimated background after cut
Neutron stars	1.0 ± 3.0	NO cut	1.0 ± 3.0
$K_S \rightarrow 2\pi, \Lambda \rightarrow p\pi$	7.8 ± 10.0	NO cut	7.8 ± 10.0
Electron pairs:			
a) External Conversions	≤ 9	$m_{e^+e^-} > 30 \text{ MeV}$	≤ 0.3
b) Dalitz pairs	20 ± 5		12 ± 3
Lambda beta decay, $\Lambda \rightarrow p + e^- + \bar{\nu}$	24 ± 16	$m_{ep} > 1.115 \text{ GeV}$	0.0
\bar{K}^0 - production			
a) $\pi^- p \rightarrow \bar{K}^0 K^0 n$	< 11		< 11
b) $K^- p \rightarrow \bar{K}^0 n$	$\sim 5 \pm 2$	NO cut	$\sim 5 \pm 2$
Total background in 1137 events			26 ± 11 < 11 from $\bar{K}^0 K^0$ production

IV. EFFICIENCY CALCULATION AND MAXIMUM LIKELIHOOD FITS

The last chapter concluded with a sample of 1137 K_{e3} events. In this chapter, these data are fit to X , the $\Delta S = \Delta Q$ rule violation parameter. The function used to fit the data is a product of the decay distributions derived in Chapter 1 and $\epsilon_{K_{e3}}(x_K)$, the efficiency for K_{e3} detection at a given decay length, x_K . This chapter first discusses the Monte Carlo calculation of $\epsilon_{K_{e3}}(x_K)$ and concludes with the maximum likelihood fitting of the data.

A. K_{e3} Efficiency Calculation

In fitting the decay position distributions to X , the likelihood function that is maximized has the general form:

$$\mathcal{L} = \prod_i f(x_i) \epsilon(x_i) \quad \text{where } f(x) \text{ is the decay distribution}$$

function and $\epsilon(x)$ is the acceptance efficiency for an event whose decay length is x . In the Monte Carlo calculation of $\epsilon(x)$ for K_{e3} decay, it is necessary to know the momentum spectrum and angular distribution of the decaying K^0 's. Alternatively, one could reconstruct p_K and θ_K for each event and then use $\epsilon_{K_{e3}}(p_K, \theta_K, x)$ in calculating \mathcal{L} , where $\epsilon_{K_{e3}}(p_K, \theta_K, x)$ is the efficiency calculated at fixed p_K and θ_K , without folding in their distributions. The K^0 - momentum in K_{e3} decay can be calculated up to a quadratic ambiguity by measuring θ_K and the momenta and angles of the decay secondaries. In most cases, this ambiguity can be resolved by

appealing to independent knowledge of the spectrum of p_K .

However, in this experiment, the measurement of θ_K was poor and it was not possible to find p_K , as indicated, for each event. This meant that one could not use $\epsilon_{K_{e3}}(p_K, \theta_K, x)$ to weight the events individually in the maximum likelihood calculation. The approach taken was to find the production distribution of p_K and θ_K , $D(p_K, \theta_K)$, from $K_S \rightarrow \pi^+\pi^-$ events for which p_K and θ_K were known for each event. $D(p_K, \theta_K)$ was then used as input in the K_{e3} Monte Carlo calculation of $\epsilon_{K_{e3}}(x)$ where:

$$\epsilon_{K_{e3}}(x) = \iint dp_K d\theta_K D(p_K, \theta_K) \epsilon_{K_{e3}}(p_K, \theta_K, x) \quad .$$

For a large sample, little information is lost by using the latter approach except that it involves more dependence on Monte Carlo calculations. This section will first discuss how $D(p_K, \theta_K)$ was extracted from the $K_{\pi 2}$ data and then show how the final K_{e3} efficiency was arrived at. Details of the Monte Carlo program are contained in Appendix 12.

1. Calculation of $D(p_K, \theta_K)$

The production distribution of K^0 - mesons from the brass targets, $D(p_K, \theta_K)$, was assumed to be the same from the two targets, any differences in observed distributions being due only to the acceptance difference between targets. It was further assumed that p_K and θ_K were uncorrelated in the laboratory so that $D(p_K, \theta_K) = f(p_K) \cdot g(\theta_K)$. These assumptions are justified by the consistency

achieved in fitting momentum and angle distributions from both targets with the single distribution $f(p_K) \cdot g(\theta_K)$. For fitting, f and g were parameterized as follows:

$$f(p) = e^{-\frac{1}{2}\left(\frac{p-A}{B}\right)^2} \cdot R(p; C, D); \text{ 4 parameters}$$

$$g(\theta) = \theta \cdot e^{-\frac{1}{2}\left(\frac{\theta-S}{T}\right)^2}; \text{ 2 parameters}$$

where $R(p; C, D)$ is a ramp function, designed to make the p_K - spectrum fall faster than a Gaussian at the high momentum end:

$$R = 1; p < C$$

$$R = (D-p)/(D-C); C \leq p \leq D$$

$$R = 0, p > D$$

In the actual six parameter fit the momentum resolution $S(p-p')$ was included; its Gaussian parameter σ is .16 GeV/c for T1, .30 GeV/c for T2 at $p_K = 2.4$ GeV/c, the mean K^0 - momentum.

A sample of clean $K_S \rightarrow 2\pi$ decays was obtained from a set of calibration runs by demanding:

- (a) The same reconstruction criteria that were imposed on the final sample of K_{e3} 's.
- (b) $m_{p\pi} > 1.160$ GeV
- (c) $m_{\pi\pi} > .440$ GeV.

Since $K_S \rightarrow 2\pi$ is a 2-body decay, p_K and θ_K can be calculated from the momenta and angles of the secondaries alone, unlike the case of

3-body K_{e3} . The observed p_K, θ_K distribution of this sample was then fit to a distribution function of the form:

$$\zeta(p_K, \theta_K) = \int dp' S(p_K - p') f(p') g(\theta_K) \epsilon_{K_{\pi 2}}(p', \theta_K)$$

where $\epsilon_{K_{\pi 2}}(p', \theta_K)$ was calculated by generating $K_S \rightarrow 2\pi$ decays exponentially in time. The fit gave the best values:

$$A = 2.48 \begin{array}{l} + .03 \\ - .08 \end{array}$$

$$B = 0.82 \begin{array}{l} + .13 \\ - .03 \end{array}$$

$$C = 2.68 \begin{array}{l} + .04 \\ - .07 \end{array}$$

$$D = 2.86 \begin{array}{l} + .01 \\ - .00 \end{array}$$

$$S = -1.0 \begin{array}{l} + .9 \\ - 1.4 \end{array}$$

$$T = 9.0 \pm .6$$

A sketch of the resulting $f(p)$ and $g(\theta)$ is shown in Fig. 19. The procedure was checked by generating $K_S \rightarrow 2\pi$ decays with $f(p_K) \cdot g(\theta_K)$ from the best fit as input. The Monte Carlo and data were compared for p_K and θ_K distributions. Fig. 20 shows these comparisons for T1 and T2. Fig. 21 shows the comparison for $K_S \rightarrow 2\pi$ decay position distributions. In all cases the agreement is good. The decay position comparison gives a non-trivial check on the calculation of $\epsilon_{K_{\pi 2}}(p_K, \theta_K, x)$ as a function of x .

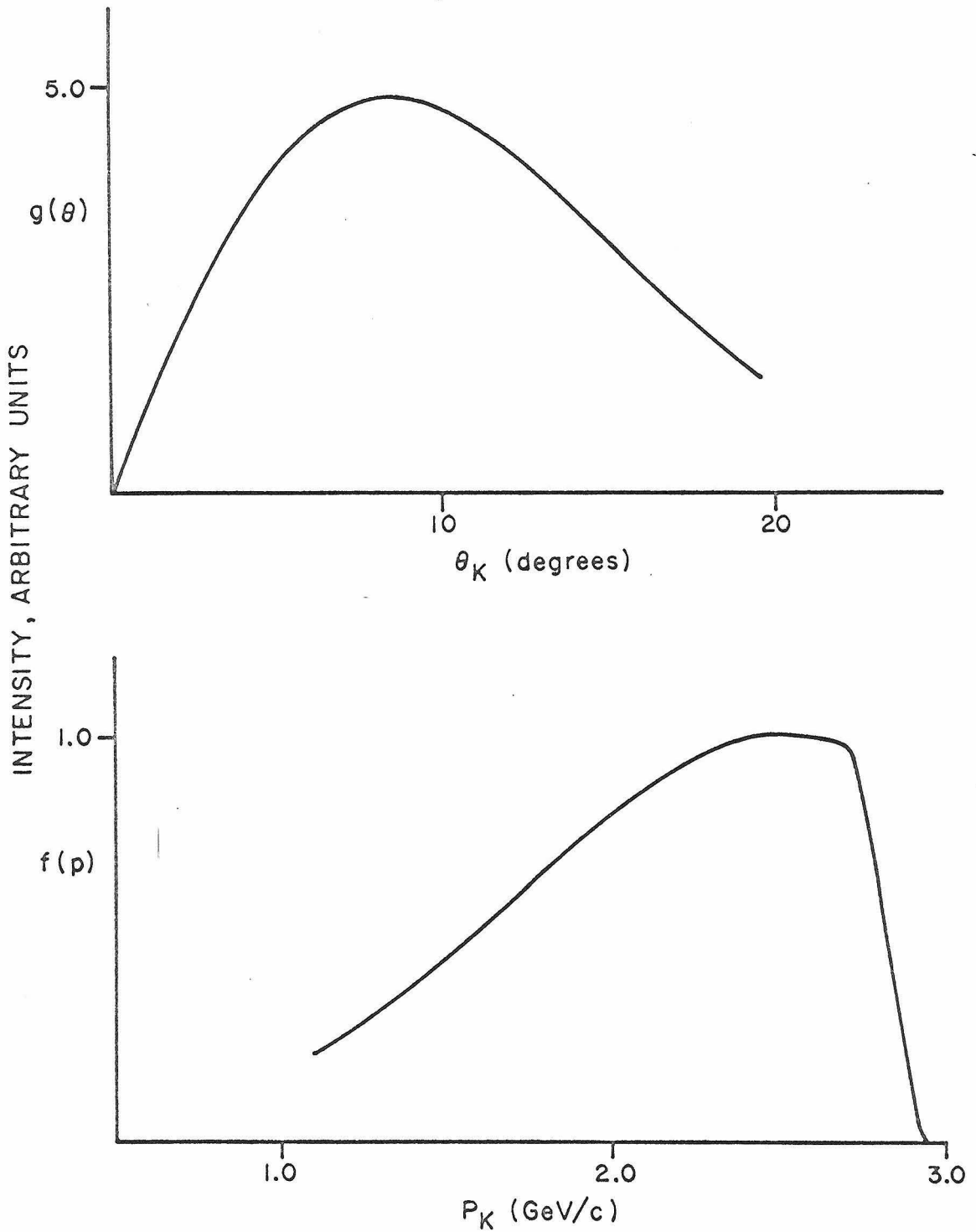


Fig.19 Sketch of K^0 -production distributions, $f(p)$ and $g(\theta)$

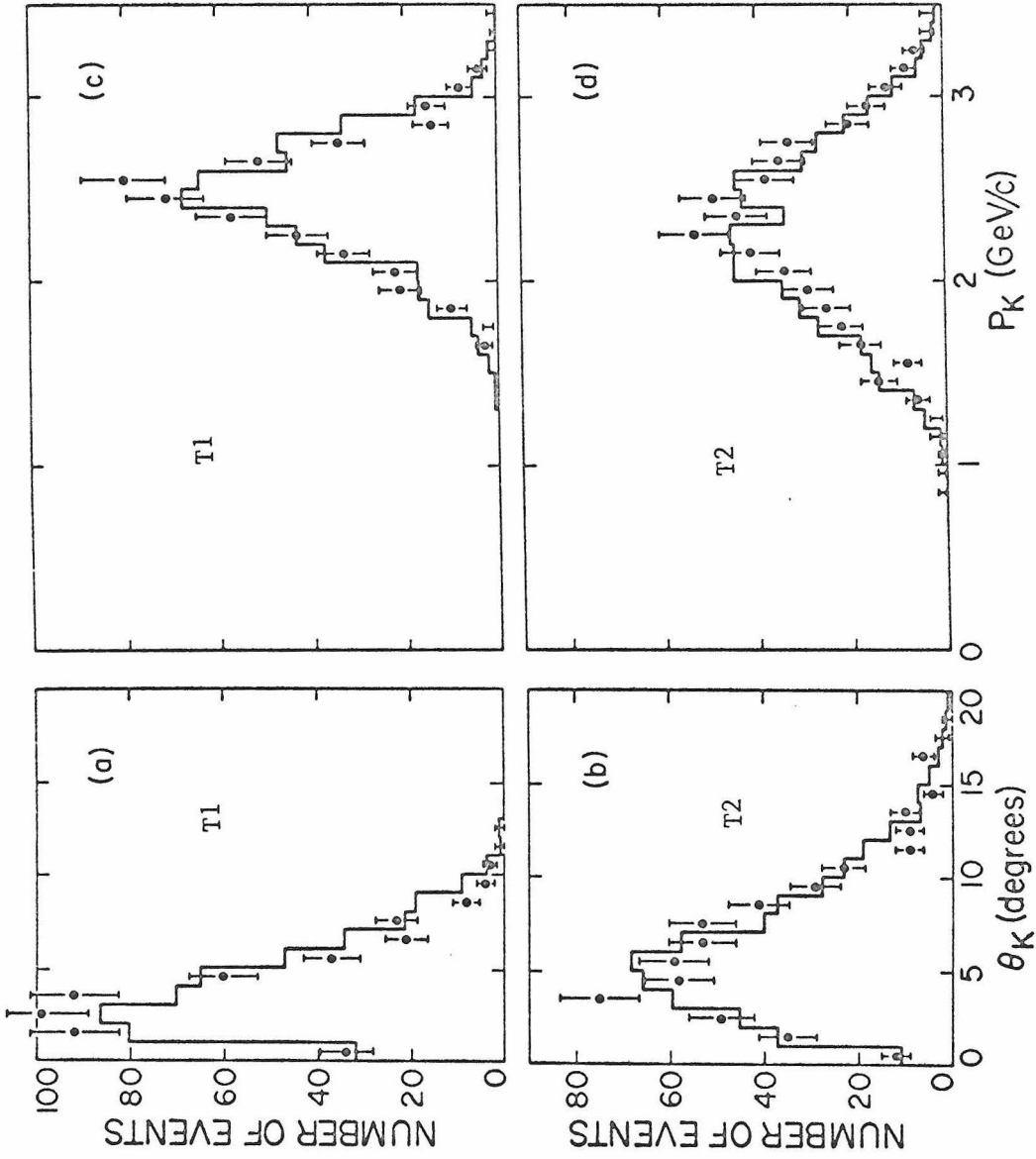


Fig. 20 Comparison of calibration data (points) and Monte Carlo (histograms) for momentum and angle distributions from each target

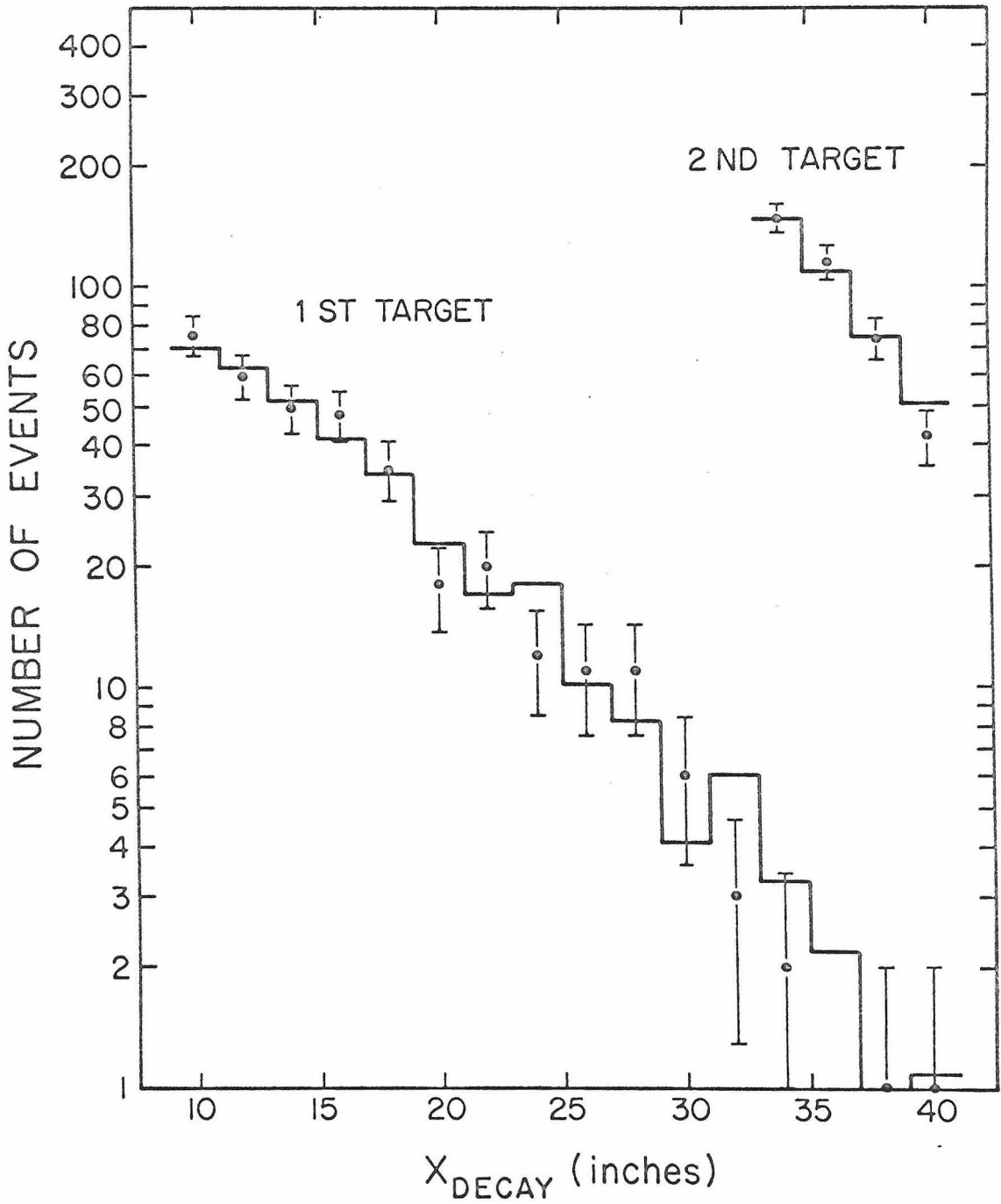


Fig. 21 Comparison of decay position distribution for calibration data (points) and Monte Carlo (histograms) from each target

2. Calculation of $\epsilon_{K_{e3}}(x)$

The distributions of $f(p_K)$ and $g(\theta_K)$ were then used as input in generating K_{e3} 's to determine $\epsilon_{K_{e3}}(x)$ at fixed values of decay position, x . For the first target, six positions were chosen at 5" intervals and for the second, two positions were chosen, also 5" apart. In order that the conditions producing these M.C. events be the same as those that produced the K_{e3} data in Chapter 3, it was necessary to make extra selections whose effects are summarized in Table 4. The selections were:

- (a) As seen in Appendix 10, Fig. 45, the computer tape scan had an energy dependent efficiency for accepting electrons, since it demanded a $1\frac{1}{2}$ times minimum-ionizing pulse in the shower counters. This efficiency was imposed on the Monte Carlo successes.
- (b) For events where the electron shone its Cerenkov light on a particular part of one of the gas counter mirrors, it was found that there was a deficiency of events in the data compared to the Monte Carlo. This effect was corrected for in the M. C. events.
- (c) The mass cuts $m_{ep} > 1.115$ GeV and $m_{ee} > 30$ MeV were imposed on the M. C. successes.

From Table 4 it is evident that these corrections mostly lower the level of the efficiency and only make slight changes to the slope as a function of x .

TABLE 4. CORRECTIONS TO K_{e3} EFFICIENCY FUNCTION

Field, Target	Decay Position X (inches)	Efficiency Without Correction	Electron Pulse Height (a)	Gas Counter Mirror (b)	Mass Cuts (c)	Final Efficiency	Overall % Change	Lower f(p) by 100 MeV/c
Low, T1 (Target Center 8.0")	10	.0242	-21%	-1%	-13%	.0165	-32%	-15%
	15	.0294	-20%	+1%	-14%	.0204	-27%	-11%
	20	.0393	-22%	-2%	-13%	.0265	-33%	-14%
	25	.0475	-23%	+2%	-13%	.0326	-31%	-17%
	30	.0578	-24%	+1%	-14%	.0380	-34%	-12%
	35	.0662	-25%	+1%	-15%	.0428	-35%	-9%
	40	.0739	-25%	+2%	-14%	.0485	-34%	-10%
Low, T2 (Target Center 32.2")	35	.0941	-25%	+3%	-14%	.0630	-33%	-7%
	40	.0997	-25%	+5%	-13%	.0683	-31%	-5%
High, T1	10	.0224	-20%	0%	-14%	.0155	-31%	-14%
	15	.0267	-21%	+1%	-10%	.0191	-28%	-15%
	20	.0393	-21%	0%	-11%	.0277	-30%	-13%
	25	.0442	-21%	+1%	-10%	.0313	-29%	-11%
	30	.0539	-24%	+3%	-16%	.0354	-34%	-12%
	35	.0621	-25%	+2%	-13%	.0416	-33%	-11%
	40	.0691	-24%	+3%	-15%	.0457	-34%	-10%
High, T2	35	.0837	-24%	+3%	-14%	.0565	-32%	-5%
	40	.0934	-25%	+5%	-14%	.0640	-31%	-6%

% change due to these
corrections

A possible position-dependent bias in the apparatus would arise if the gas counter efficiency were decay position dependent. Fig. 22 shows the mean pulse height for TL K_{e3} 's as a function of decay position. The solid line is the best straight-line fit. From the mean and width of the pulse height distributions, it was estimated that the overall efficiency of the counter for K_{e3} 's was $> 93\%$. From the straight-line fit, it was estimated that the variation in this efficiency between the extremes of decay position was $\sim 1.2\%$ and so of negligible effect on the K_{e3} efficiency.

The efficiency functions for the two targets $\epsilon_1(x)$ and $\epsilon_2(x)$ were derived by fitting the data in the seventh column of Table 4 ; $\epsilon_1(x)$ was fit to $A_0 + A_1 x + A_2 x^2$ and $\epsilon_2(x)$ to $B_0 + B_1 x$. The efficiency was calculated and fit at the two magnetic field settings, 2.0 and 2.8 Kg; Fig.23 shows 2.8 Kg fit, also fit when $f(p)$ was displaced by 100 MeV/c in calculating ϵ .

Comparisons of data to M.C. were made for: (a) pion momentum distribution, (b) electron momentum distribution, and (c) π -e resultant momentum distribution. These are shown in Fig. 24, the pion M. C. histogram has been corrected for pion decay, which has a visible effect for $p_\pi < 500$ MeV/c. Fig. 25 shows the comparison of data to M. C. for the invariant mass of the π -e combination, $m_{\pi e}$. The agreement is good in all cases. Further checks on the Monte Carlo calculations are discussed in Appendix 12.

The efficiency functions $\epsilon_1(x)$ and $\epsilon_2(x)$ will now be used in the maximum likelihood fitting in the next section.

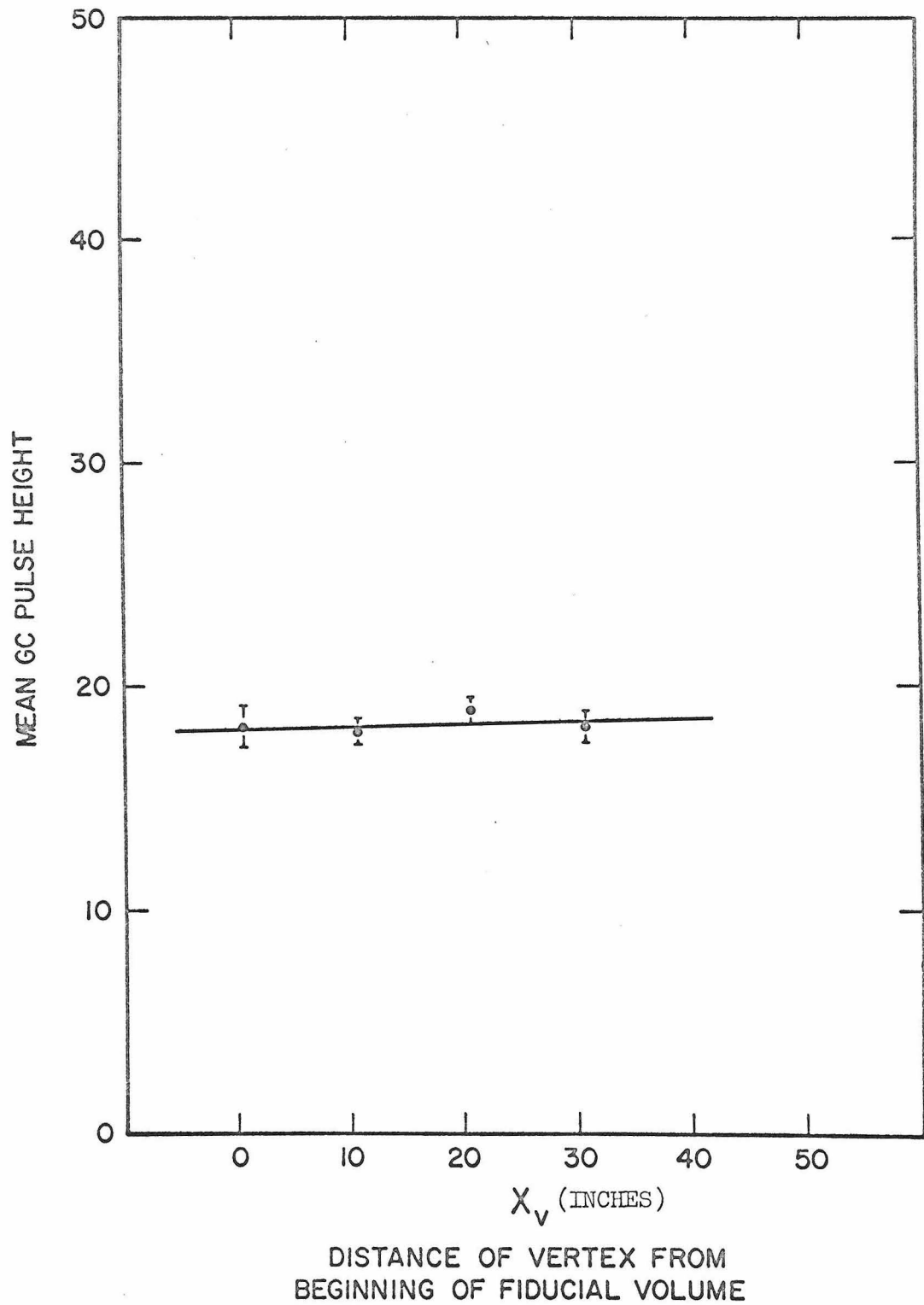


Fig. 22 Mean GC pulse height as a function of decay position for $Tl \pi e$ data. Smooth curve is best straight line fit.

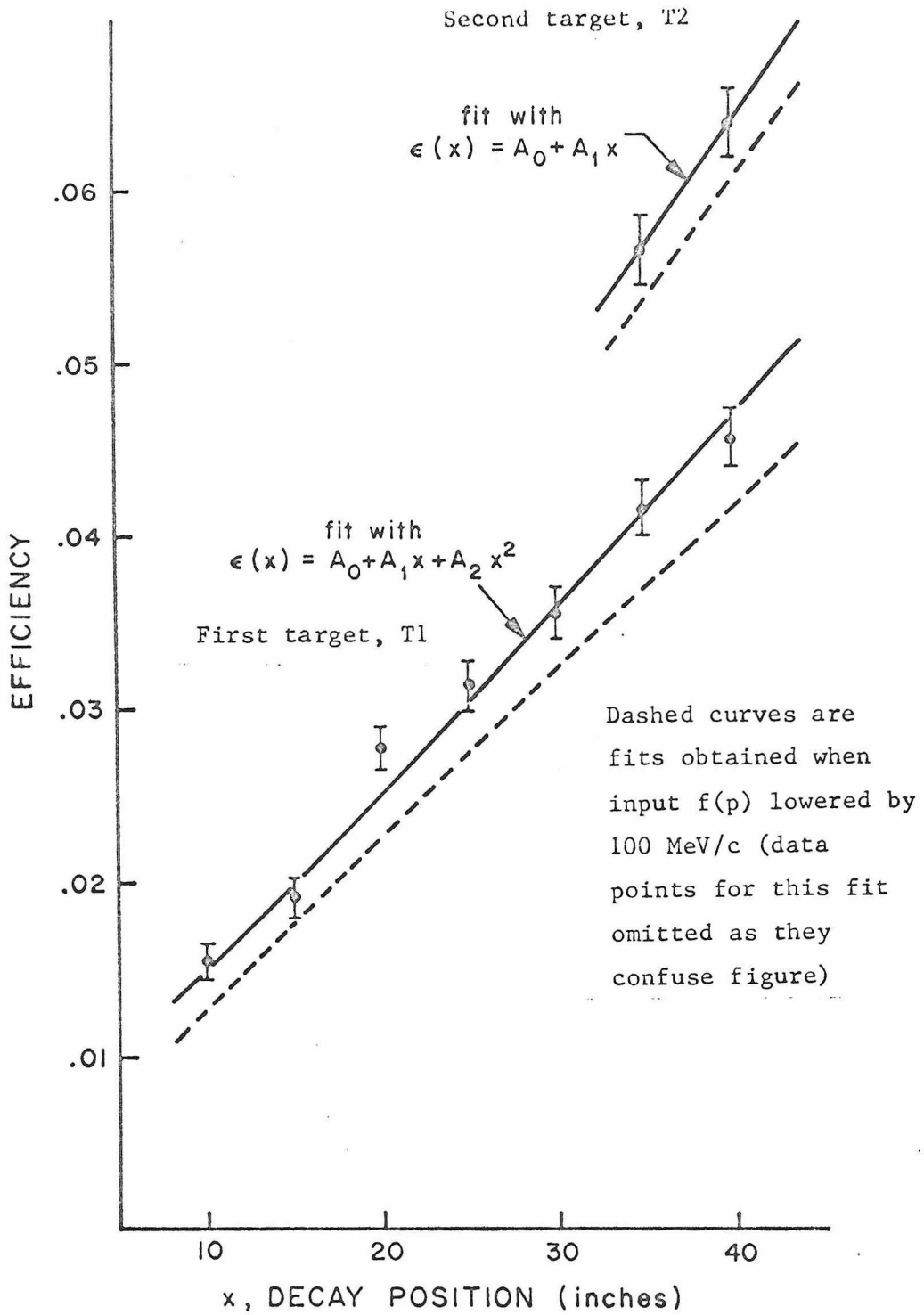


Fig. 23 Efficiency functions at 2.8 Kg.
Errors are from M.C. statistics.

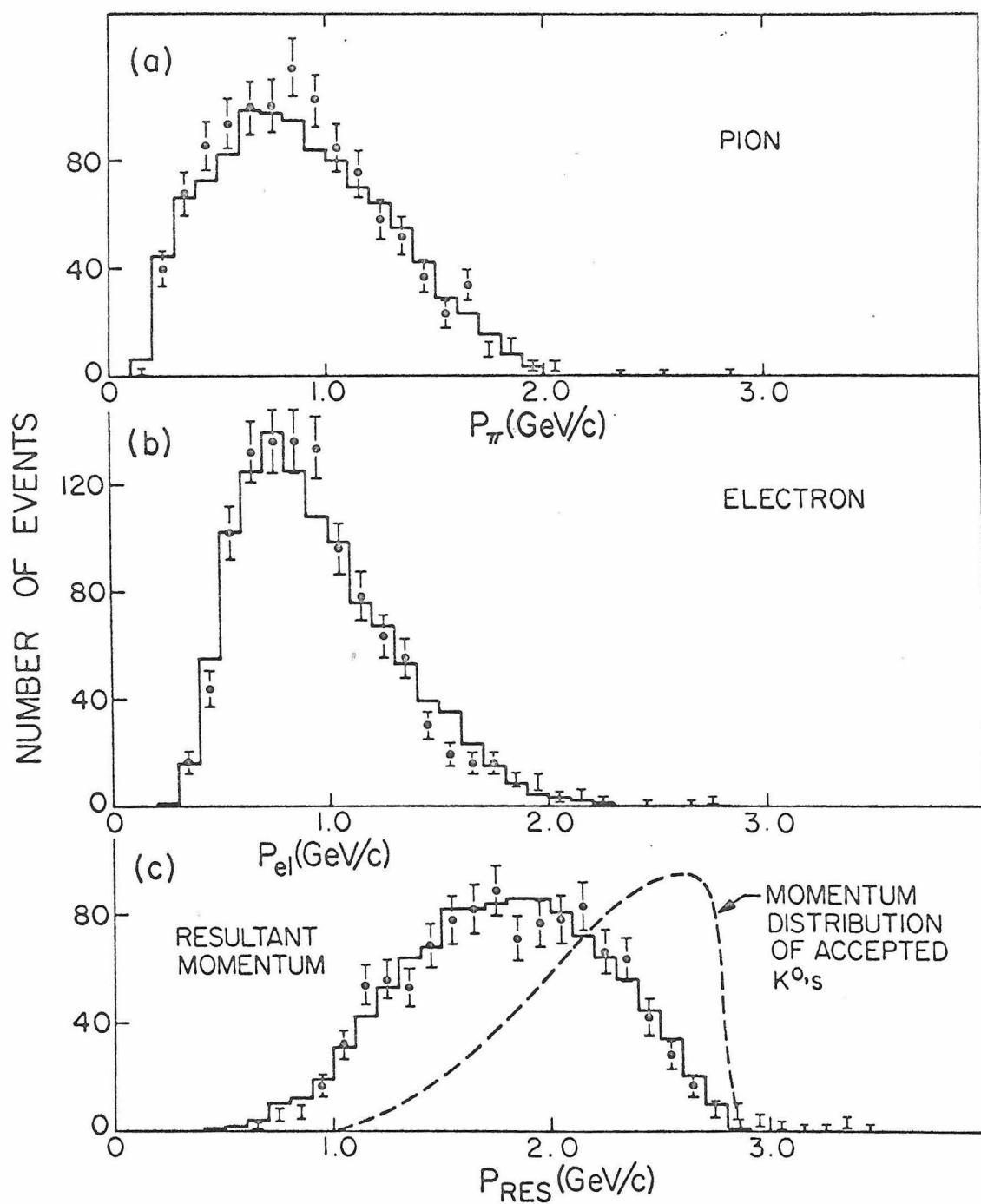


Fig. 24 Comparison between πe data (points) and Monte Carlo (histograms) for : (a) pion momentum, (b) electron momentum and (c) π -e resultant momentum.

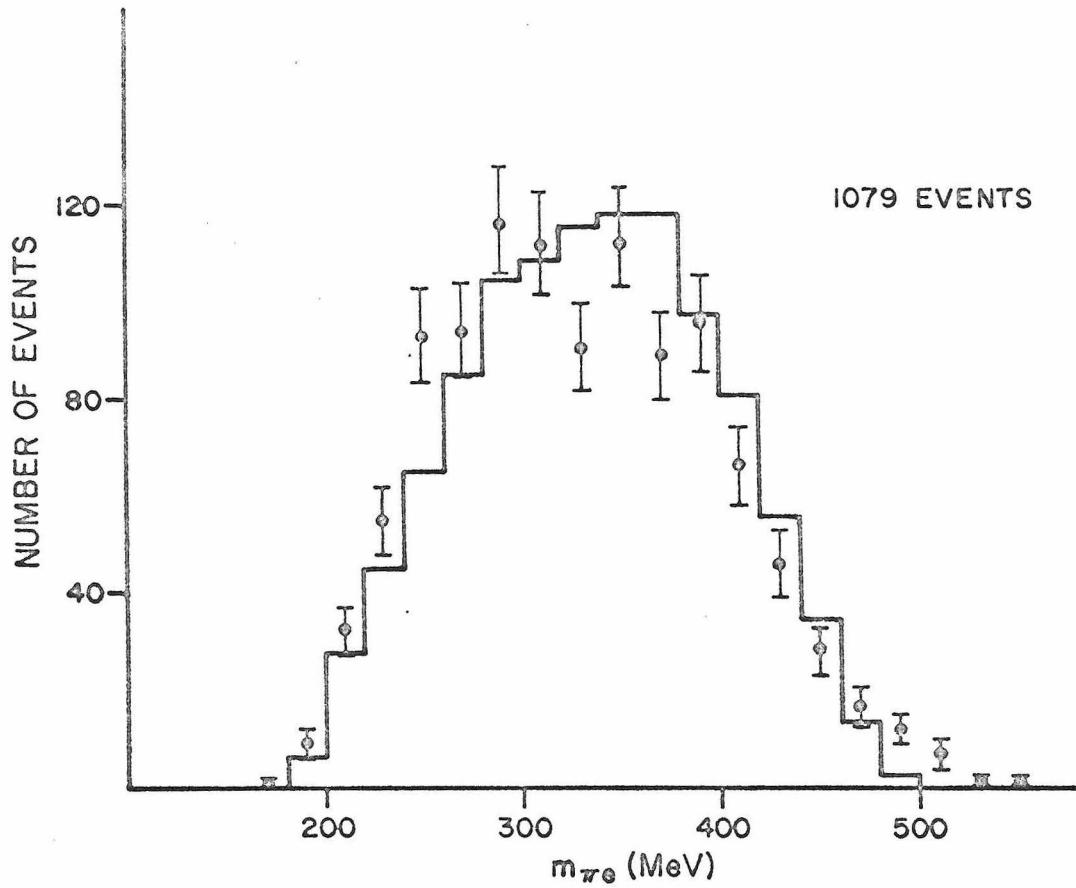


Fig. 25 Comparison between πe data (points) and Monte Carlo (histogram) for $m_{\pi e}$, the invariant mass of the πe

B. Maximum Likelihood Fitting of Data

This section will first outline the fitting procedure, then make fits to the data and finally investigate the sensitivity of the result to variations in input parameters and to cuts on the data.

1. Details of Maximum Likelihood Calculation

The best value for the parameter X was determined in a program that maximized the likelihood function

$$\mathcal{L} = \prod_{i=1}^{n_1^+} G_1^+(t_i) \cdot \prod_{i=1}^{n_1^-} G_1^-(t_i) \cdot \prod_{i=1}^{n_2^+} G_2^+(t_i) \cdot \prod_{i=1}^{n_2^-} G_2^-(t_i)$$

where, for example

$$G_1^+(t_i) = \frac{N^+(t_i) \epsilon_1(t_i)}{\int_{T_1}^{T_2} (N^+(t) + N^-(t)) \epsilon_1(t) dt} \quad \begin{array}{l} \text{for } e^+ \text{ events from} \\ \text{the first target,} \end{array}$$

$N^+(t)$ are the time distributions discussed in Chapter 1,

$\epsilon_1(t)$ is the K_{e3} detection efficiency from target 1 at proper time t , at the appropriate field value,

n_1^+ is the total number of e^+ events from target 1

T_1 and T_2 are the fiducial volume limits from the target in question

t_i is the proper time assigned to event i .

The proper time for an event is related to the decay position by the relation $t = \frac{x_D - x_P}{\beta_x c} \cdot m_K$, where x_P is the pro-

duction point, x_D the decay point, and p_x^K is the K-momentum projected in the x direction. The target length of 1.2" and K-momentum spectrum FWHM of 900 MeV/c cause an uncertainty in the proper time for an individual event, which is usually, however, a fraction of a K_S lifetime. This uncertainty is minimized if one takes for x_P the center of the target and uses the average $\langle 1/p_x^K \rangle$ for $1/p_x^K$ in calculating the proper time of each event. $1/\langle 1/p_x^K \rangle$ was 2.28 GeV/c for T1 and 2.22 GeV/c for T2. The smearing effect of the x_P - and p_K -distributions on the time distribution $N^+(t)$ is investigated in Appendix 13. The time distributions $N^+(t)$ used in calculating \mathcal{L} were corrected to take into account moments up to the second. It is shown in Appendix 13 that the effect of higher moments changes $|X|$ by < 0.01 .

In calculating time distributions, the following quantities were taken from Ref. 11:

$$\tau_S = 0.862 \times 10^{-10} \text{ sec.}$$

$$\tau_L = 0.538 \times 10^{-7} \text{ sec.}$$

$$\Delta m \tau_S = 0.469$$

The maximum likelihood procedure was checked by generating K_{e3} time distributions with different values of X and then using them as input to the fitting program. The resulting fits were:

2000 events, with input $X = (-.069, +.108)$;

$$\text{fit gave } X = \begin{pmatrix} -.060 & +.024 \\ & -.032 \end{pmatrix}, \begin{pmatrix} .080 & +.048 \\ & -.044 \end{pmatrix}$$

2000 events, with input $X = (0.0, 0.0)$;

$$\text{fit gave } X = \left(0.000 \begin{array}{l} +.024 \\ -.038 \end{array}, 0.000 \begin{array}{l} +.036 \\ -.034 \end{array} \right)$$

which are within the expected limits.

2. Fitting of the Data

The 1137 events which survived all the selections of Chapter III were reduced to 1079 by a fiducial volume cut which removed the last 2" of the downstream end of the decay region. It was felt that vees from this region were more difficult to identify in the scanning and hence prone to bias. When these 1079 events were fit by the maximum likelihood program, the result was:

$$\text{ReX} = -.069 \pm .036$$

$$\text{ImX} = +.108 \begin{array}{l} +.092 \\ -.074 \end{array}$$

Fig. 26 shows the time distributions of the data with smooth curves corresponding to a) best fit, b) $X = 0$, c) $X = (+.14, -.13)$, the world average given in Chapter I. A notable feature is that the error in ImX is more than twice that for ReX , in apparent contradiction to the statements made in Chapter I, where it was stated that $n' = 500$ would give errors of $\pm .04$ for both ReX and ImX . This larger error occurs because there are non-linear terms coming into effect as one moves away from $X = 0$ and the estimate of errors given in Chapter I assumed $X = 0$.

The likelihood contours for the fit are shown in Fig. 27.

The relative probability of $X = 0$, relative to the best fit is 0.25

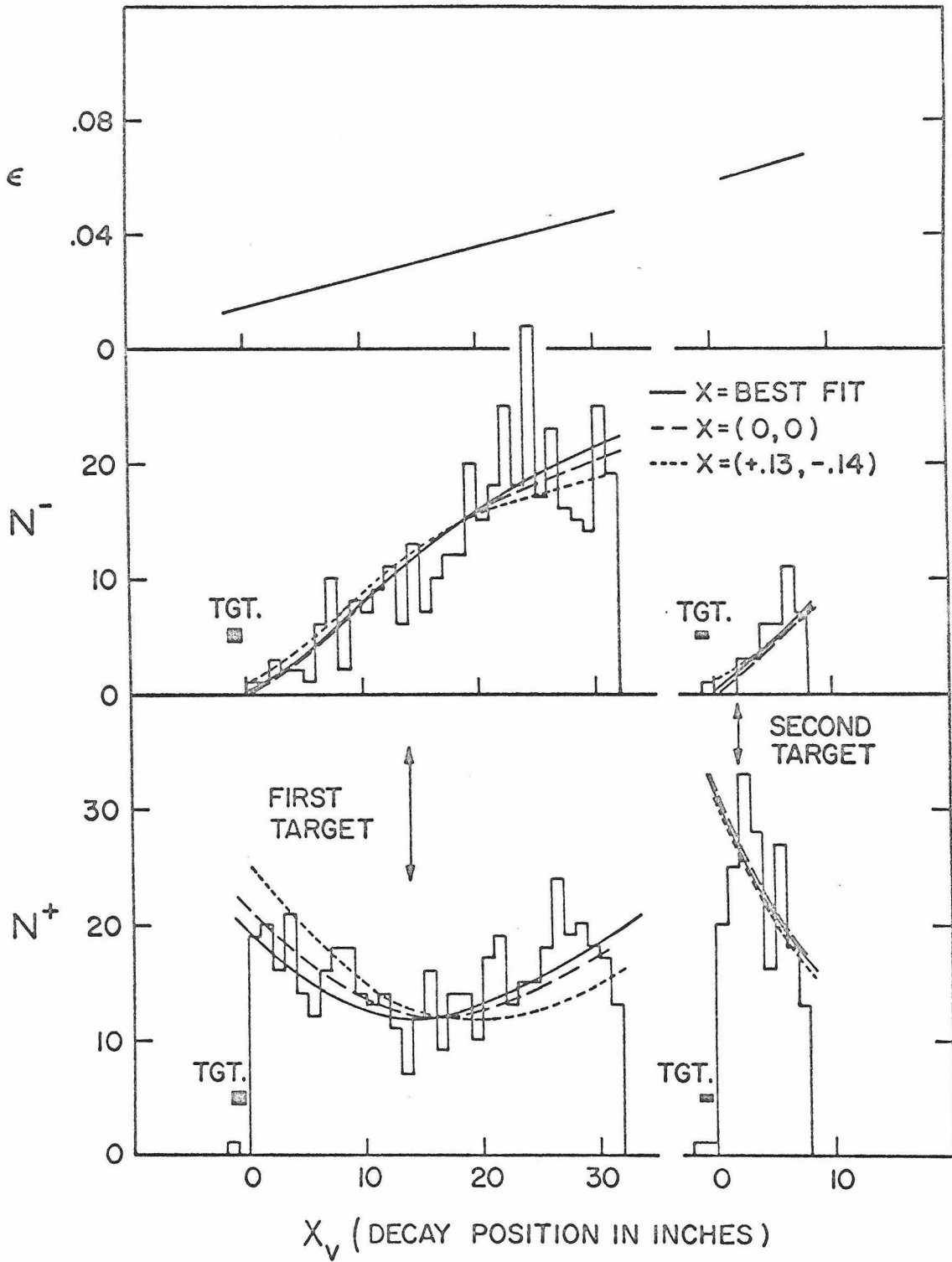


Fig. 26 Final decay position distributions of π^- sample.

(a) Efficiency functions; (b) N^- distribution from each target; (c) N^+ distributions.

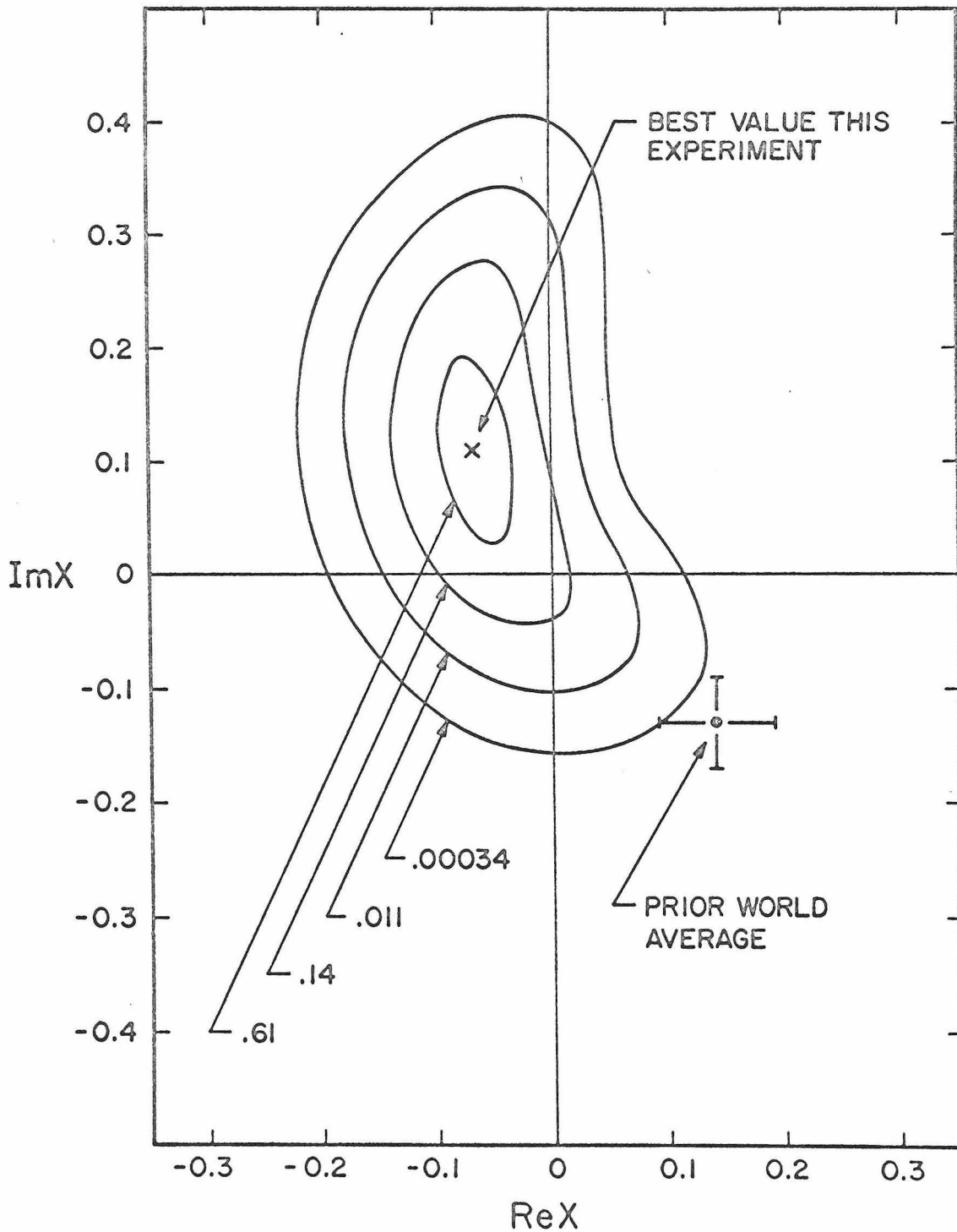


Fig. 27 The best value of X from this experiment. Also shown are the contours corresponding to the 1,2,3,4 standard deviation limits, showing the probability relative to the best result.

while that of the world average relative to the best fit is $< e^{-8} = 3.3 \times 10^{-4}$. Hence, the best fit and the world average are inconsistent with one another but both are consistent with $X = 0$.

If one assumes CP conservation in the decay ($\text{Im}X = 0$ in the fit), the best fit gives

$$\text{Re}X = \begin{matrix} -.036 & +.036 \\ & -.044 \end{matrix} .$$

Conversely, if one assumes maximal CP-violation in the breakdown of $\Delta S = \Delta Q$, i.e., $\text{Re}X = 0$ in the fit, the best fit gives

$$\text{Im}X = \begin{matrix} +.02 & +.058 \\ & -.060 \end{matrix} .$$

Both of these results are clearly consistent with $X = 0$.

3. Sensitivity of the Result

In this section the sensitivity to variations in the input parameters and cuts on the data will be investigated.

(a) $K_L - K_S$ mass difference

The mass difference $m_L - m_S$ was allowed to vary as a free parameter in the M.L. fit, giving:

$$\text{Re}X = \begin{matrix} -.081 & +.034 \\ & -.036 \end{matrix}$$

$$\text{Im}X = \begin{matrix} +.101 & +.094 \\ & -.088 \end{matrix}$$

$$\Delta m \tau_S = \begin{matrix} +.424 & +.052 \\ & -.048 \end{matrix}$$

The last is in good agreement with the accepted value of

$$+.469 \pm .015^{(11)}$$

The time dependence of $N^+ - N^-$, the difference of the e^- time distributions, depends only on τ_S , Δm and $\epsilon(t)$, i.e.,

$$N^+(t) - N^-(t) \propto e^{-t/2\tau_S} \cdot \cos \Delta m t \cdot \epsilon(t).$$

It was hoped that a χ^2 fit of $N^+ - N^-$ to this time dependence would place some restrictions on $\epsilon(t)$ and hence make a direct check on $\epsilon(t)$ from the data. However, the fit is relatively insensitive to $\epsilon(t)$ since $N^+ - N^-$ goes through zero at $\Delta m t = \pi/2$ which corresponds to about three K_S lifetimes. A wide range of slopes in $\epsilon(t)$ will still give a good fit to $N^+ - N^-$.

(b) \bar{K}^0 fraction

As an independent check that produced \bar{K}^0 's were not a problem, the fraction of \bar{K}^0 at $t = 0$, $\eta_{\bar{K}^0}$, was allowed to vary as a free parameter by using the time distributions

$$N^+(t) = (1 - \eta_{\bar{K}^0}) N_{K^0}^+(t) + \eta_{\bar{K}^0} N_{\bar{K}^0}^+(t)$$

$$N^-(t) = (1 - \eta_{\bar{K}^0}) N_{K^0}^-(t) + \eta_{\bar{K}^0} N_{\bar{K}^0}^-(t) \quad \text{where, for example,}$$

$N_{\bar{K}^0}^+(t)$ is the same as $N_{K^0}^-(t)$ except that the term with $\text{Im}X$

occurs with an opposite sign. The best fit gave:

$$\text{Re}X = \begin{array}{l} -.056 \quad +.036 \\ \quad \quad \quad -.038 \end{array}$$

$$\text{Im}X = \begin{array}{l} +.116 \quad +.082 \\ \quad \quad \quad -.080 \end{array}$$

$$\eta_{\bar{K}^0} = \begin{array}{l} .006 \quad +.019 \\ \quad \quad \quad -.006 \end{array}$$

in agreement with the fraction estimated in Chapter III.

(c) Fiducial volume variation

Table 5 shows a series of fits in which the limits of the fiducial volume were varied at both the upstream and downstream ends of the decay region. The variations are consistent with statistical fluctuations and the limits finally chosen were 9.28" (Plate 2) to 41.00" for T1 and 33.43" (Plate 2) to 41.00" for T2.

(d) Mean momentum, mean production point and K_{e3} efficiency function

Table 6 summarizes the effects of varying these inputs. The mean K-momentum of accepted K_{e3} 's was varied by ± 50 MeV/c, corresponding to $2\frac{1}{2}$ times the standard deviation on the mean momentum calculated from the $K_S \rightarrow 2\pi$ data. The mean production point was changed by ± 0.25 ", corresponding to a position distribution of production points which falls to zero at one edge of the target. The latter is an extreme assumption and it is hard to conceive of a mechanism which could give such a strong variation in K^0 - acceptance between ends of the 1.2" targets. Sensitivity to the efficiency function $\epsilon(x)$ was investigated by varying the parameters of the K^0 momentum and angle distributions used as input in the K_{e3} Monte Carlo program. $f(p_K)$ was displaced by 100 MeV/c and $g(\theta_K)$ was derived from each target

TABLE 5. FITS WITH VARIATIONS IN FIDUCIAL VOLUME

The standard fiducial volume is defined from Plate 2 -- 41".

In this table it is varied at both ends.

Conditions	Number of Events	ReX	ImX
Pl.2 -- 42"	1123	-0.053 $\begin{matrix} +.034 \\ -.036 \end{matrix}$	+0.064 $\begin{matrix} +.092 \\ -.074 \end{matrix}$
Pl.2 -- 41.5"	1102	-0.061 $\begin{matrix} +.032 \\ -.038 \end{matrix}$	+0.096 $\begin{matrix} +.094 \\ -.078 \end{matrix}$
Pl.2 -- 41"	1079	-0.069 $\begin{matrix} +.036 \\ -.036 \end{matrix}$	+0.108 $\begin{matrix} +.092 \\ -.074 \end{matrix}$
Pl.2 -- 40.5"	1054	-0.069 $\begin{matrix} +.034 \\ -.036 \end{matrix}$	+0.128 $\begin{matrix} +.088 \\ -.080 \end{matrix}$
Pl.2 -- 40"	1024	-0.066 $\begin{matrix} +.034 \\ -.036 \end{matrix}$	+0.153 $\begin{matrix} +.082 \\ -.084 \end{matrix}$
Pl.2 -- 39.5"	978	-0.065 $\begin{matrix} +.036 \\ -.034 \end{matrix}$	+0.132 $\begin{matrix} +.084 \\ -.090 \end{matrix}$
Pl.2 -- 39"	949	-0.065 $\begin{matrix} +.034 \\ -.038 \end{matrix}$	+0.156 $\begin{matrix} +.082 \\ -.096 \end{matrix}$
Pl.2 -- 38.5"	919	-0.065 $\begin{matrix} +.034 \\ -.040 \end{matrix}$	+0.168 $\begin{matrix} +.084 \\ -.092 \end{matrix}$
Pl.2 -- 38"	880	-0.065 $\begin{matrix} +.038 \\ -.036 \end{matrix}$	+0.172 $\begin{matrix} +.080 \\ -.102 \end{matrix}$
Pl.3 -- 41"	1061	-0.061 $\begin{matrix} +.036 \\ -.038 \end{matrix}$	+0.096 $\begin{matrix} +.086 \\ -.072 \end{matrix}$
Pl.4 -- 41"	1047	-0.053 $\begin{matrix} +.040 \\ -.038 \end{matrix}$	+0.099 $\begin{matrix} +.080 \\ -.072 \end{matrix}$
Pl.5 -- 41"	1034	-0.052 $\begin{matrix} +.036 \\ -.042 \end{matrix}$	+0.108 $\begin{matrix} +.092 \\ -.080 \end{matrix}$

TABLE 6. FITS WITH VARIATIONS IN MEAN MOMENTUM, MEAN PRODUCTION POINT AND K_{e3} EFFICIENCY FUNCTION

Conditions of Fit	ReX	ImX	
Increase $\langle 1/p_K \rangle^{-1}$ by 50 MeV/c	-0.078 +.034 -.036	+0.112 +.080 -.088	
Decrease $\langle 1/p_K \rangle^{-1}$ by 50 MeV/c	-0.061 +.034 -.036	+0.108 +.086 -.080	
Move Average Production Point Upstream 25"	-0.049 +.034 -.036	+0.104 +.092 -.074	
Move Average Production Point Downstream by .25"	-0.085 +.032 -.038	+0.096 +.092 -.078	
Variations in inputs to K_{e3} efficiency	Use T2 Angular Distribution	-0.066 +.036 -.034	+0.104 +.092 -.078
	Use T1 Angular Distribution	-0.065 +.032 -.038	+0.132 +.080 -.092
	Lower $f(p)$ by 100 MeV/c in Efficiency Calculation	-0.042 +.034 -.036	+0.072 +.110 -.070

separately and used as input. In all cases the variations are small compared to the statistical error.

(e) Cuts on the data

Table 7 shows a summary of additional fits made in an attempt to demonstrate the presence of background or some systematic bias from the apparatus. The final result is shown for reference. The second and third entries are fits to the sum $N^+ + N^-$ and to the asymmetry $(N^+ - N^-)/(N^+ + N^-)$, the latter being independent of efficiency. Fig.'s 28 and 29 show the likelihood contours for these two fits and they are clearly consistent. As mentioned in Chapter III, in the discussion on background, there are extra cuts which can reduce the $K_S \rightarrow 2\pi$, $\Lambda \rightarrow p\pi$ and Dalitz $e^+ - e^-$ backgrounds by substantial factors. These are made in the fourth and fifth entries and show no effect, confirming the estimates of background made in Chapter III. Possible charge asymmetry was checked by dividing the data into the two magnetic field polarities used. Entries 6 and 7 are statistically consistent. The effect of a position dependent bias in the gas counter was investigated by dividing the data into two samples, one with GC pulse < 18 , the mean pulse height, and the other with GC pulse > 18 . In entries 8 and 9 the two samples give consistent results in agreement with the conclusion reached earlier in this Chapter, that the gas counter efficiency is not position dependent. Entries 10 and 11 show fits for the first and second targets separately, in agreement

TABLE 7. FITS MADE INVESTIGATING BACKGROUNDS AND BIASES IN DATA

Run Condition	Number of Events	ReX	ImX
Final Result	1079	$-.069 \pm .036$	$+.108 \begin{matrix} +.092 \\ -.074 \end{matrix}$
Sum Only (neglect charge)	1079	$-.076 \begin{matrix} +.086 \\ -.118 \end{matrix}$	$+.100 \begin{matrix} +.092 \\ -.112 \end{matrix}$
Asymmetry Only	1079	$-.068 \begin{matrix} +.036 \\ -.038 \end{matrix}$	$+.181 \begin{matrix} +.110 \\ -.160 \end{matrix}$
Reduce $K^0 \rightarrow \pi^+ + \pi^-$ $\Lambda^0 \rightarrow p + \pi^-$ background by factor of 3 (see Text, p.64)	1031	$-.065 \begin{matrix} +.034 \\ -.038 \end{matrix}$	$+.092 \begin{matrix} +.104 \\ -.068 \end{matrix}$
Reduce Dalitz background by factor of 4.8 (see Text, p.65)	1066	$-.069 \begin{matrix} +.034 \\ -.036 \end{matrix}$	$+.108 \begin{matrix} +.096 \\ -.070 \end{matrix}$
Magnetic Field Up	516	$-.057 \pm .050$	$+.099 \begin{matrix} +.120 \\ -.096 \end{matrix}$
Magnetic Field Down	563	$-.081 \begin{matrix} +.046 \\ -.052 \end{matrix}$	$+.123 \begin{matrix} +.140 \\ -.116 \end{matrix}$
Large Cerenkov Pulse (> 18)	487	$-.037 \begin{matrix} +.046 \\ -.050 \end{matrix}$	$+.137 \begin{matrix} +.104 \\ -.110 \end{matrix}$
Small Cerenkov Pulse (≤ 18)	592	$-.085 \begin{matrix} +.052 \\ -.056 \end{matrix}$	$+.043 \begin{matrix} +.120 \\ -.086 \end{matrix}$
First Target Only	868	$-.053 \begin{matrix} +.048 \\ -.046 \end{matrix}$	$+.164 \begin{matrix} +.098 \\ -.120 \end{matrix}$
Second Target Only	211	$-.045 \begin{matrix} +.056 \\ -.062 \end{matrix}$	$-.004 \begin{matrix} +.130 \\ -.080 \end{matrix}$
Positive Electrons Only	672	$-.077 \pm .072$	$+.016 \begin{matrix} +.160 \\ -.190 \end{matrix}$
Negative Electrons Only	407	$-.045 \begin{matrix} +.054 \\ -.068 \end{matrix}$	$+.168 \begin{matrix} +.084 \\ -.102 \end{matrix}$

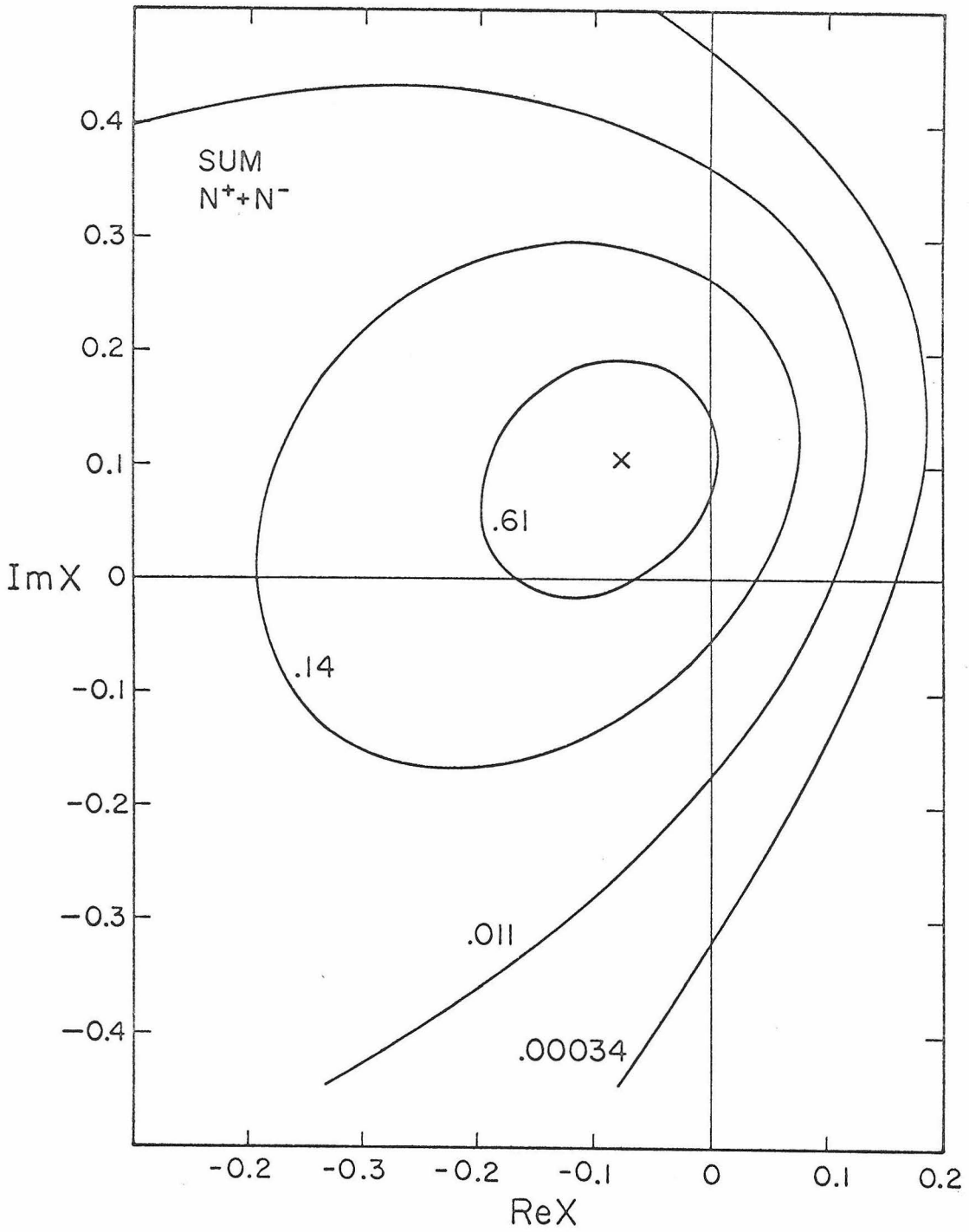


Fig. 28 Likelihood contours for fit to sum

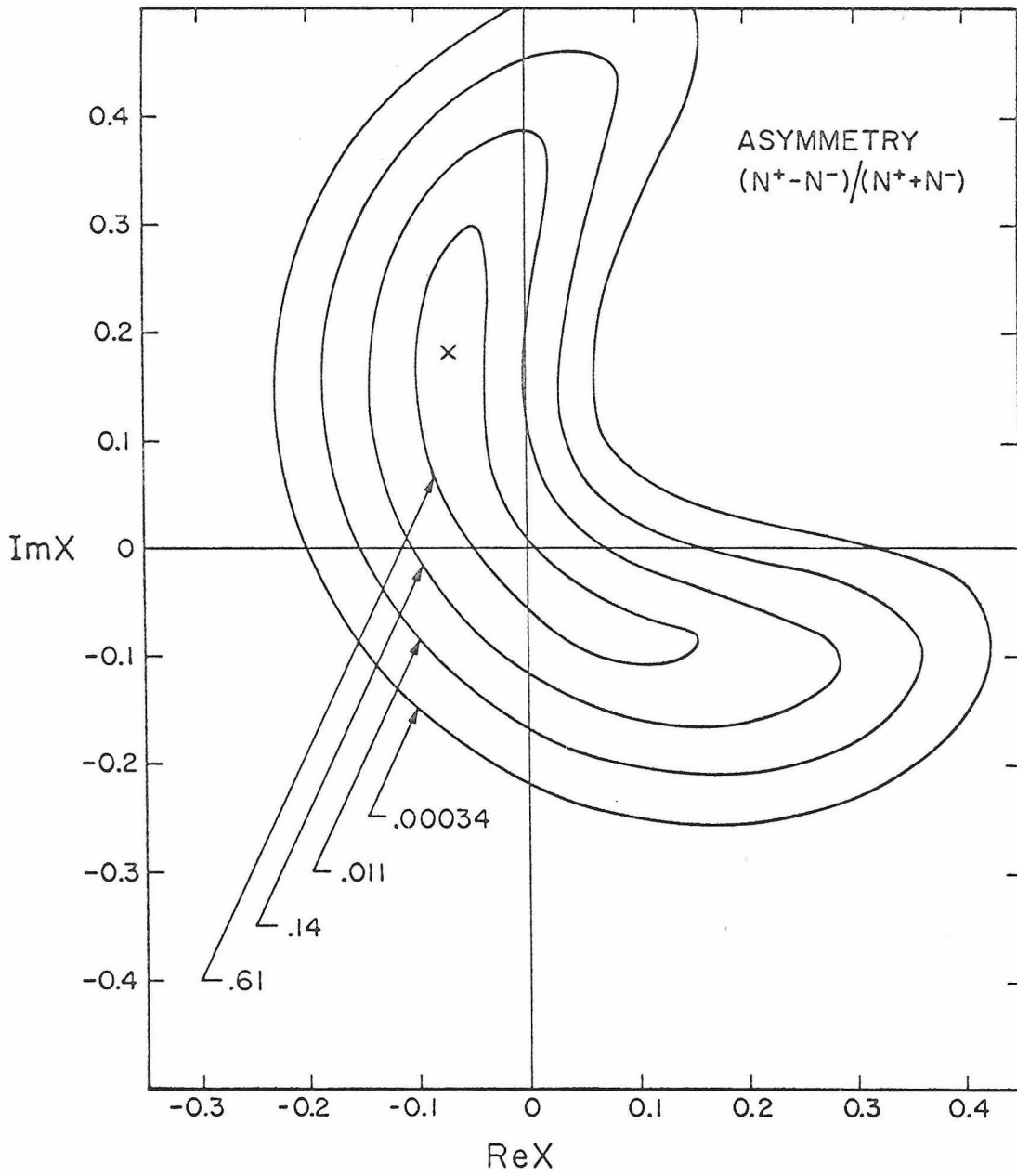


Fig. 29 Likelihood contours for fit to asymmetry

with each other. Entries 12 and 13 show the effect of fitting to e^+ and e^- data separately. Before CPT-invariance is assumed, there are two independent parameters X and \bar{X} , one occurring in the e^+ time distribution and the other in the e^- time distribution. If one assumes CPT-invariance these satisfy $\bar{X} = X^*$. From the last two fits $|X - \bar{X}| = .155 \pm .219$, consistent with CPT-invariance.

In conclusion, all of these tests, a) through e), show no reason to include any systematic error in the final error quoted for X .

V. CONCLUSIONS AND OUTLOOK

The final result for this experiment is:

$$\text{Re}X = -.069 \pm .036$$

$$\text{Im}X = +.108 \begin{matrix} +.092 \\ -.074 \end{matrix} .$$

The difference in the logarithm of the likelihood function for this best value and for $X = 0$ is $\Delta \log \mathcal{L} = 1.38$ so the relative probability that $X = 0$ is correct is $e^{-1.38} = 0.25$. The previous world average,

$$\text{Re}X = +.14 \pm .05$$

$$\text{Im}X = -.13 \pm .043$$

while inconsistent with the above result (relative probability $< e^{-8} = 3.3 \times 10^{-4}$), is consistent with $X = 0$. If the present result is incorporated into the world average, the latter becomes:

$$\text{Re}X = +.002 \pm .029$$

$$\text{Im}X = -.080 \pm .038$$

which implies that $|X| < .16$ with 90% confidence. One can be legitimately suspicious of the errors in the old world average and the 90% confidence limit on $|X|$ would be lower than .16 if the error on $\text{Im}X$, $\pm .043$, were increased to include systematic errors.

At this stage the reader is likely to ask the following questions:

- a) If the experiment were to be repeated with the same boundary conditions, e.g., beam time, major equipment, etc., what changes would optimize the experiment?
- b) With existing accelerators and techniques, how should a high precision measurement of X be made?

In answer to (a), the following hindsight remarks are relevant. By spending about six months modifying the apparatus it would have been possible to: (1) lower the triggering rate by reducing the amount of material available for γ -conversions in the front end, e.g., by using wider gap chambers and (2) increase the acceptance of the apparatus by moving the production-decay region further into the center of the magnet. Of course, there was considerable pressure to finish the run and six months of further work on the apparatus was an unattainable luxury.

The question of further experiments posed by (b) is a less academic question. Such an experiment should:

- (1) Use a K^+ -beam which gives a higher yield of K^0 's per incident beam particle, lowering the trigger rate per K^0 produced,
- (2) Work at high energies where the efficiency for K^0 -detection is greater for a given aperture and electron detection by shower technique is easier,
- (3) Use wire chambers to facilitate data analysis,
- (4) Use hodoscopic gas Cerenkov counters so that Cerenkov radiation properties of both π and e are examined,

- (5) Reduce the amount of material in the decay region to the lowest possible level to cut down on the triggering rate,
- (6) Collect $\sim 100,000$ events at which level the systematic errors will tend to exceed the statistical but with careful design should be surmountable.

At the time of writing an experiment to collect 30,000 K_{e3} 's is being run at the CERN PS by a CERN-Orsay-Vienna collaboration. Another K_{e3} experiment, of comparable statistical accuracy, is scheduled to begin in late 1970 at the ANL ZGS, to be performed by a University of Chicago group. These two experiments incorporate many of the features (1) - (6) but are sufficiently different in technique that one would hope them to be sensitive to different systematic errors. When these experiments are analyzed, the parameter X should be known to $< .01$ in both $\text{Re}X$ and $\text{Im}X$ for the K_{e3} case.

With the advent of high energy, high intensity neutrino beams at NAL, study of the reactions:

$$\bar{\nu} + n \rightarrow \Sigma^- + \mu^+ \quad (\Delta S = +\Delta Q)$$

$$\nu + n \rightarrow \Sigma^+ + \mu^- \quad (\Delta S = -\Delta Q)$$

will become possible in heavy liquid bubble chambers. At high energies the cross section of the allowed $\bar{\nu} + n \rightarrow \Sigma^- + \mu^+$ is expected to be no more than an order of magnitude less than the cross sections of the quasi-elastic reactions $\nu + n \rightarrow p + \mu^-$, $\bar{\nu} + p \rightarrow n + \mu^+$. A high precision $\Delta S = \Delta Q$ rule test by this method is quite feasible.

VI. APPENDICES

Appendix 1: Theoretical Supplement

The notation used in describing the $K^0 - \bar{K}^0$ system is that of Lee and Wu⁽²³⁾ who define the states:

$$|K_S^0\rangle = ((1 + \epsilon_1)|K^0\rangle + (1 - \epsilon_1)|\bar{K}^0\rangle) [2(1 + |\epsilon_1|^2)]^{-\frac{1}{2}}$$

$$\text{and } |K_L^0\rangle = ((1 + \epsilon_2)|K^0\rangle - (1 - \epsilon_2)|\bar{K}^0\rangle) [2(1 + |\epsilon_2|^2)]^{-\frac{1}{2}}$$

they also define $\epsilon = \frac{1}{2}(\epsilon_1 + \epsilon_2)$ and $\delta = \frac{1}{2}(\epsilon_1 - \epsilon_2)$. $\delta = 0$ if CPT-invariance holds and both δ and ϵ vanish if CP-invariance is also true.

The most general amplitude for $K \rightarrow \pi + \ell + \nu$ consistent with Lorentz invariance and a V-A leptonic current, has the form

$$\langle \pi \ell \nu | K \rangle \propto [f_+(q^2)(P+Q)_\mu + f_-(q^2)(P-Q)_\mu] \cdot \bar{\Psi}_\ell \gamma_\mu (1 + \gamma_5) \Psi_{\nu_\ell}$$

where $f_+(q^2)$ and $f_-(q^2)$ are Lorentz scalars depending only on $(P-Q)^2$, P and Q being the K and π 4-momenta respectively. It can be shown (Ref. 24, p. 342) that the form factor $f_-(q^2)$ enters with a coefficient (m_ℓ/m_K) and so, for K_{e3} decay, can be neglected. In general, $f_-(q^2)$ can have different SU(3) properties from $f_+(q^2)$ and so $K_{\mu 3}^0$ decay could exhibit different behavior from K_{e3}^0 with respect to the $\Delta S = \Delta Q$ rule. However, study of $K_{\mu 3}^0$ with counters and spark chambers is very difficult due to the background $K_S^0 \rightarrow \pi^+ \pi^-$ with either π decaying to the normal $\mu\nu$ mode. It will be assumed that K_{e3} is being

considered and f_+ is written f .

In general, there are four distinct amplitudes, writing the whole amplitude as f ,

$$\left. \begin{array}{l} f, \text{ the amplitude for } K^0 \rightarrow \pi^- + e^+ + \nu \\ \bar{f}, \text{ the amplitude for } \bar{K}^0 \rightarrow \pi^+ + e^- + \bar{\nu} \end{array} \right\} \Delta S = + \Delta Q$$

$$\left. \begin{array}{l} \bar{g}, \text{ the amplitude for } K^0 \rightarrow \pi^+ + e^- + \bar{\nu} \\ g, \text{ the amplitude for } \bar{K}^0 \rightarrow \pi^- + e^+ + \nu \end{array} \right\} \Delta S = - \Delta Q$$

and one defines $X = g/f$ and $\bar{X} = \bar{g}/\bar{f}$. The q^2 -dependence of f and \bar{f} is known to be small (see for example Ref. 8, p. 232) and possible q^2 -dependence of X and \bar{X} will henceforth be neglected.

The discrete symmetries C, P and T imply relations between these amplitudes. Rewriting in full:

$$\langle \pi e \nu | K \rangle \propto f(q^2) (P+Q)_\mu \cdot \bar{\Psi}_e \gamma_\mu (1 + \gamma_5) \Psi_{\nu_e} .$$

Since there are no strong interactions in the final state $\pi e \nu$, the phase difference between $|\pi e \nu \rangle_{\text{in}}$ and $|\pi e \nu \rangle_{\text{out}}$ is electromagnetic so that $|\pi e \nu \rangle_{\text{in}} \approx |\pi e \nu \rangle_{\text{out}}$. CPT-invariance implies $\bar{f} = -f^*$, $\bar{g} = -g^*$ so that $\bar{X} = X^*$. The negative sign in $\bar{f} = -f^*$ comes about as follows (see, for example, Ref. 24, p. 401): the hadronic part of the amplitude transforms like a 4-vector and does not change sign under CPT, the leptonic part changes sign since:

$$(CPT)^{-1} (\bar{\Psi}_a O_i \Psi_b) CPT = -(\bar{\Psi}_a O_i \Psi_b) \text{ for } O_i = V \text{ or } A. \text{ The}$$

complex conjugate enters since T is an anti-linear operator.

T-invariance alone implies that Γ , $\bar{\Gamma}$, g and \bar{g} can all be chosen relatively real:

$$\begin{aligned} \text{out} \langle B|H|A \rangle_{\text{in}} &= \text{out} \langle A|H|B \rangle_{\text{in}} , \text{ statement of T-invariance} \\ &= \text{in} \langle B|H|A \rangle_{\text{out}}^* , \text{ since H is Hermitian} \\ &= \text{out} \langle B|H|A \rangle_{\text{in}}^* , \text{ since } |\pi\nu\rangle_{\text{in}} \approx |\pi\nu\rangle_{\text{out}} \\ &\quad \text{and } |K^0\rangle_{\text{in}} = |K^0\rangle_{\text{out}} . \end{aligned}$$

Hence, T-invariance implies $\text{Im}X = \text{Im}\bar{X} = 0$.

With CPT-invariance, $\text{Im}X \neq 0$ implies direct CP violation in the leptonic K-decay. Sachs has suggested that such an effect could be the source of the CP-violation seen in $K_L \rightarrow 2\pi$ decay. If one writes for ϵ (see Ref. 25 for details), previously defined for the K_L and K_S states:

$$\epsilon = \epsilon_T + \epsilon_M = \frac{\Gamma_{12} - \Gamma_{12}^*}{(\Gamma_S - \Gamma_L) - 2i\delta m} + i \frac{M_{12} - M_{12}^*}{(\Gamma_S - \Gamma_L) - 2i\delta m}$$

then the contribution to ϵ_T from leptonic decay modes is:

$$\begin{aligned} \epsilon_T(\text{lept}) &= \frac{2 \Gamma_L(\text{leptonic})}{(\Gamma_S - \Gamma_L) + 2i(m_S - m_L)} \cdot \frac{i \text{Im}X}{|1-X|^2} \\ &= \text{Im}X((1.7 \pm .4) \times 10^{-3}) e^{i(132.9^\circ \pm 1.0^\circ)} . \end{aligned}$$

Since $\epsilon \sim 2 \times 10^{-3}$ and $\phi_\epsilon \sim 45^\circ$, if one assumes $|X| \lesssim 0.2$, then one has

to look to ϵ_M if one wishes to attribute the $K_L \rightarrow 2\pi$ CP-violation solely to leptonic sources. ϵ_M involves off-mass-shell matrix elements whose values are not restricted by experiment. The ϵ_T (lept) term is also 90° out of phase with the experimental ϵ .

Without assuming CPT for the present, one obtains from the K_L, K_S states above, dropping terms of order $\epsilon^2 \sim 5 \times 10^{-6}$,

$$|K^0\rangle = (1-\epsilon_2)|K_S^0\rangle + (1-\epsilon_1)|K_L^0\rangle$$

$$|t; \text{pure } K^0 \text{ at } t=0\rangle = (1-\epsilon_2)e^{i(-m_S+i\Gamma_S/2)t}|K_S^0\rangle + (1-\epsilon_1)e^{i(-m_L+i\Gamma_L/2)t}|K_L^0\rangle$$

reexpressing in K^0, \bar{K}^0 states

$$\begin{aligned} &= e^{i(-m_S+i\Gamma_S/2)t} \left[(1-\epsilon_2)(1+\epsilon_1)|K^0\rangle + (1-\epsilon_2)(1-\epsilon_1)|\bar{K}^0\rangle \right] \\ &\quad + e^{i(-m_L+i\Gamma_L/2)t} \left[(1-\epsilon_1)(1+\epsilon_2)|K^0\rangle - (1-\epsilon_1)(1-\epsilon_2)|\bar{K}^0\rangle \right]. \end{aligned}$$

From this the transition amplitudes to decay to $\pi e \nu$ are:

$$\begin{aligned} \langle \pi^- e^+ \nu | t; K^0 \text{ at } t=0 \rangle &= e^{i(-m_S+i\Gamma_S/2)t} (f(1+2\delta) + g(1-2\epsilon)) \\ &\quad + e^{i(-m_L+i\Gamma_L/2)t} (f(1-2\delta) - g(1-2\epsilon)) \end{aligned}$$

$$\begin{aligned} \langle \pi^+ e^- \bar{\nu} | t; \bar{K}^0 \text{ at } t=0 \rangle &= e^{i(-m_S+i\Gamma_S/2)t} (\bar{g}(1+2\delta) + \bar{f}(1-2\epsilon)) \\ &\quad + e^{i(-m_L+i\Gamma_L/2)t} (\bar{g}(1-2\delta) - \bar{f}(1-2\epsilon)). \end{aligned}$$

Next replace $f(1+2\delta) + g(1-2\epsilon)$ by $f(1+y)$ where $y = 2\delta + X(1-2\epsilon)$.

Then since:

$$|e^{iat}(1+y) + e^{ibt}(1-y)|^2 = |1+y|^2 + |1-y|^2 + 2(1-|y|^2) \cos(a-b)t \\ - 4 \operatorname{Im} y \sin(a-b)t$$

one finds

$$N^+(t) = |f|^2 \left\{ e^{-\Gamma_S t} |1+y|^2 + e^{-\Gamma_L t} |1-y|^2 \right. \\ \left. + e^{-\frac{\Gamma_L + \Gamma_S}{2} t} \left[2(1-|y|^2) \cos(m_S - m_L)t + 4 \operatorname{Im} y \sin(m_S - m_L)t \right] \right\}.$$

A similar expression holds for $N^-(t)$ if one extracts \bar{g} and defines $y = 2\delta + (1-2\epsilon) \cdot (\bar{f}/\bar{g})$. Reinserting for y , we get

$$N^+ = |f|^2 \left\{ e^{-\Gamma_S t} |1+2\delta + X(1-2\epsilon)|^2 + e^{-\Gamma_L t} |1-2\delta - X(1-2\epsilon)|^2 \right. \\ \left. + e^{-\frac{\Gamma_S + \Gamma_L}{2} t} \left[2(1-|2\delta + X(1-2\epsilon)|^2) \cos(m_S - m_L)t \right. \right. \\ \left. \left. + 4 \operatorname{Im}(2\delta + X(1-2\epsilon)) \sin(m_S - m_L)t \right] \right\}$$

$$\begin{aligned}
N^- = & |\bar{f}|^2 \left\{ e^{-\Gamma_S t} |(1+2\delta)\bar{X} + (1-2\epsilon)|^2 + e^{-\Gamma_L t} |(1-2\delta)\bar{X} - (1-2\epsilon)|^2 \right. \\
& + e^{-\frac{\Gamma_S + \Gamma_L}{2} t} [2(|\bar{X}|^2 - |2\delta\bar{X} + (1-2\epsilon)|^2) \cos(m_S - m_L)t \\
& \left. + 4 \operatorname{Im} \bar{X}^* (\bar{X}2\delta + (1-2\epsilon)) \sin(m_S - m_L)t] \right\}
\end{aligned}$$

If CPT is assumed for both decay and state so that $|\bar{f}| = |f|$,

$\bar{X}^* = X$ and $\delta = 0$, these expressions become, writing $\Delta m = m_{K_L} - m_{K_S}$,

$$r = 1 - 2\epsilon.$$

$$\begin{aligned}
N^+ = & |f|^2 \left\{ e^{-\Gamma_S t} |1+Xr|^2 + e^{-\Gamma_L t} |1-Xr|^2 \right. \\
& \left. + e^{-\frac{\Gamma_L + \Gamma_S}{2} t} [2(1-|Xr|^2) \cos \Delta mt - 4 \operatorname{Im} Xr \sin \Delta mt] \right\}
\end{aligned}$$

$$\begin{aligned}
N^- = & |f|^2 \left\{ e^{-\Gamma_S t} |X^* + r|^2 + e^{-\Gamma_L t} |X^* - r|^2 \right. \\
& \left. + e^{-\frac{\Gamma_L + \Gamma_S}{2} t} [2(|X|^2 - |r|^2) \cos \Delta mt - 4 \operatorname{Im} Xr \sin \Delta mt] \right\} .
\end{aligned}$$

For $t \gg 1/\Gamma_S$, one obtains $\frac{N^+}{N^-} = \frac{|1-Xr|^2}{|X^*-r|^2} = 1 + 4 \operatorname{Re} \epsilon \cdot \frac{1-|X|^2}{|1-X|^2}$.

This quantity has been measured in the K_L charge asymmetry experiments. (26), (27), (28) Since these experiments show that

$(1 - r) \sim 4 \times 10^{-3}$ its effect on the time distributions at early

times cannot be seen until the coefficients of the time-dependent terms are measured to 0.5%, well below present day sensitivity, which is an order of magnitude worse. If r is set to unity, the time distributions become:

$$N^+(t) = |f|^2 \left\{ e^{-\Gamma_S t} |1+X|^2 + e^{-\Gamma_L t} |1-X|^2 \right. \\ \left. + 2 e^{-\frac{(\Gamma_S + \Gamma_L)}{2} t} \cdot (1-|X|^2) \cdot \cos \Delta mt \right. \\ \left. - 4 e^{-\frac{(\Gamma_S + \Gamma_L)}{2} t} \operatorname{Im} X \cdot \sin \Delta mt \right\}$$

In the final fitting of the data from this experiment to the parameter X , the above form of N^+ was used. A more precise experiment could extract X , ϵ and δ from the leptonic time distributions.

Appendix 2: Pion Beam

The particle beam used to make K^0 's in the apparatus was an unseparated π^- beam produced at O^0 to the internal circulating beam of the Bevatron. The nominal beam momentum was 2.85 GeV/c with a nominal spread of $\pm 1\%$. The beam was designed to have its first focus between the bending magnets M1 and M2 as shown in Fig. 30 with a second focus at the apparatus between the two targets. Q1A, Q1B, Q2A, Q2B are the usual quadrupole doublets required for each focus, M1 and M2 achieve the overall 17° of bending and Q4 compensates the fringe field of the Bevatron.

The beam counters were S1, S2, S3, S4, and S4V. S1 and S2 were 3" x $1\frac{1}{2}$ " scintillators used for beam tuning; S3 was a 3" x 3" one-quarter inch thick scintillator; S4 was a 0.8" diameter $\frac{1}{4}$ " scintillator; and S4V had a hole 0.9" in diameter and was 0.4" thick. All these counters had RCA 7850 phototubes whose last few dynodes were boosted by a condenser bank to handle the high rates. The fast logic which analyzed their signals is shown in Fig. 31. The transistorised fast logic modules used in all fast logic are described in Appendix 7.

The useful beam intensity was 3×10^5 per 10^{12} protons steered onto the internal target. This intensity was at a level that gave one extra beam track in the production-decay chambers for about 50% of the pictures. Any increase in intensity would have made scanning these pictures more difficult.

Of vital interest to the K_{e3} experiment is the K^- contamination in the beam since a K-minus can charge-exchange to \bar{K}^0 and give

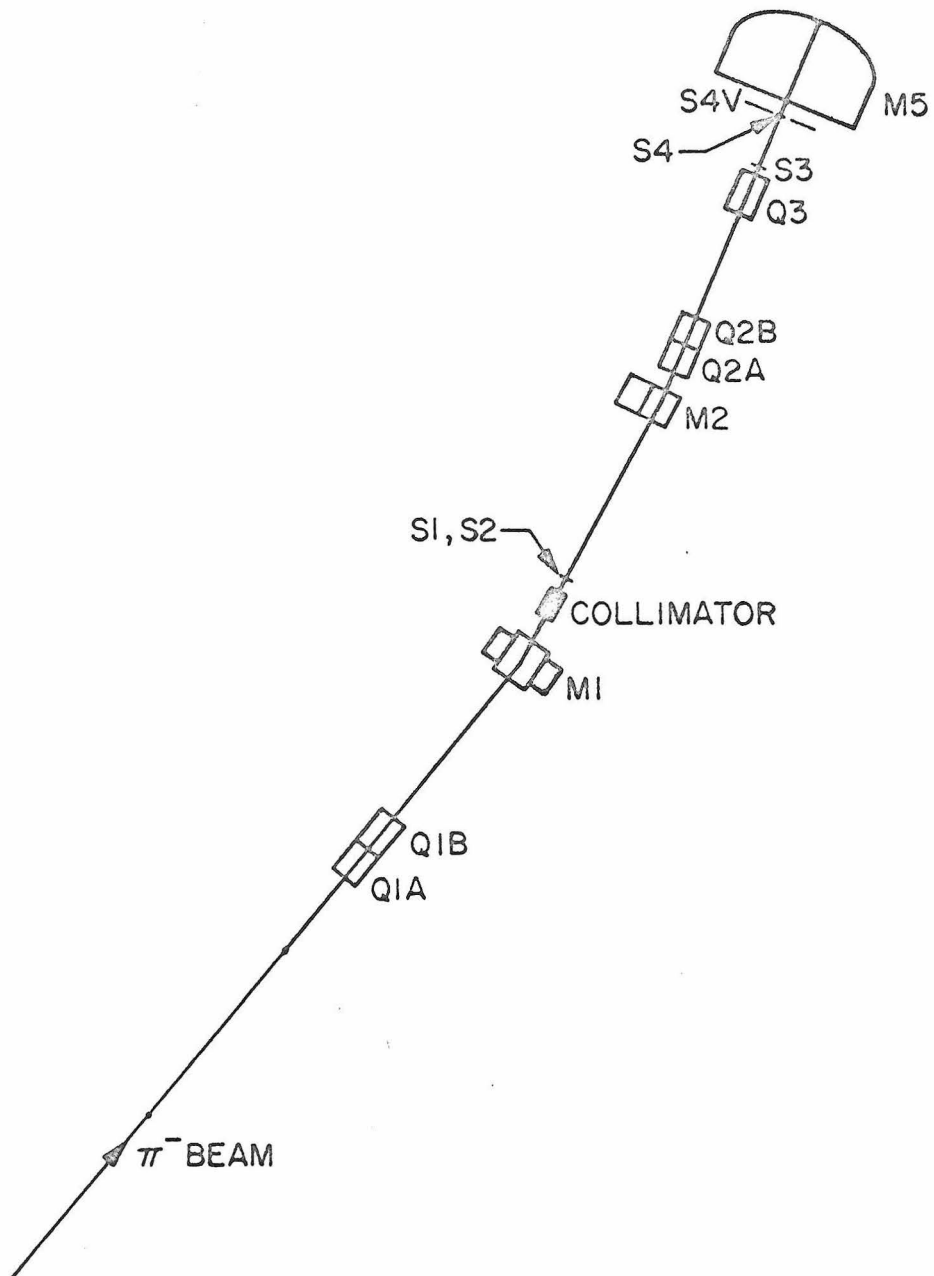


Fig. 30

Sketch of π^- beamline

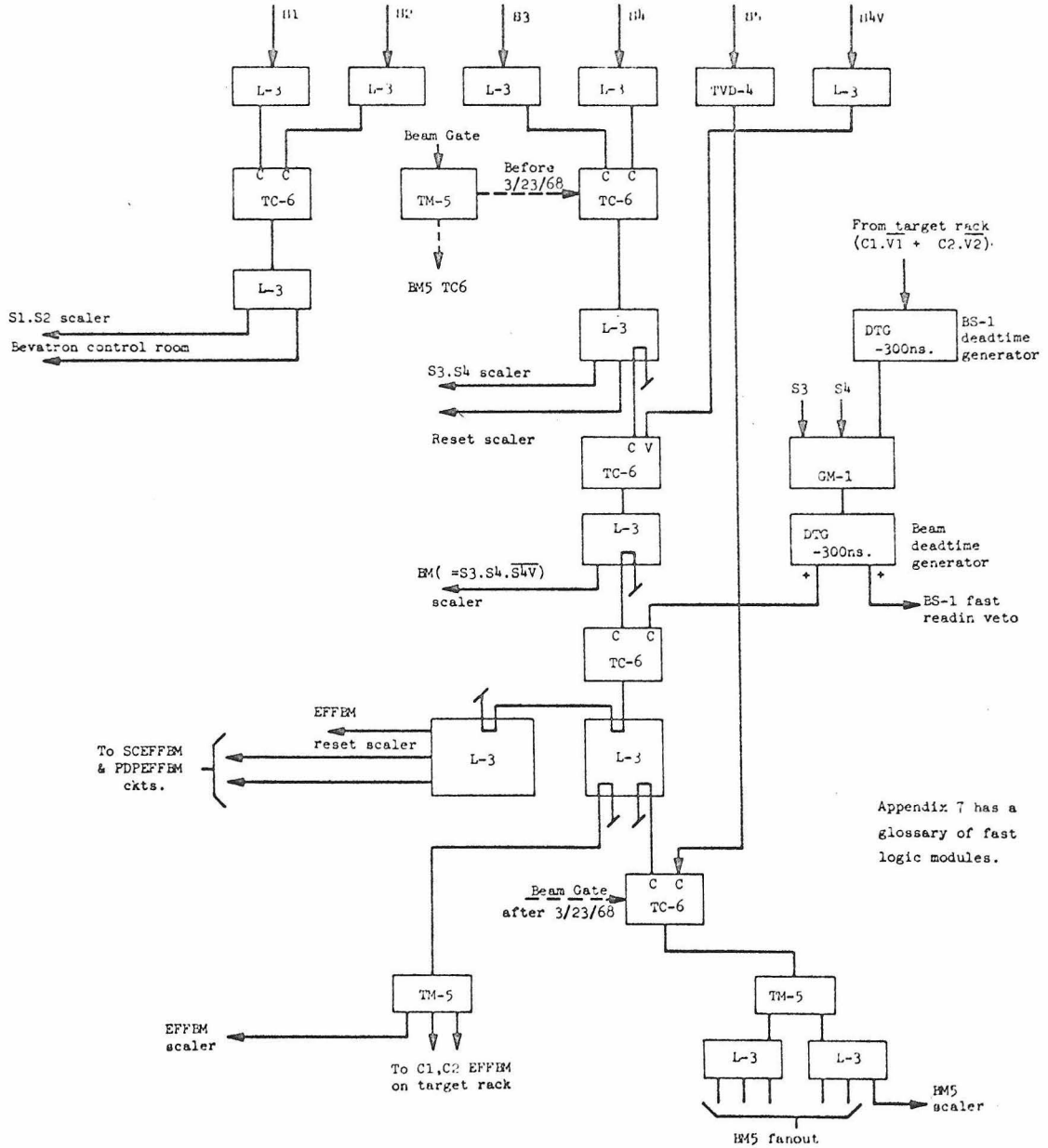


Fig. 31

Block diagram of beam electronics

an initial state of opposite strangeness from a K^0 . A ten atmosphere SF_6 Cerenkov counter was placed in the beam. By analyzing the Cerenkov pulse in coincidence with a time of flight system the K^- - contamination of the beam was measured to be $(0.1 \pm 0.01)\%$.

Appendix 3: Targets and Target Counters

As mentioned in the text, it was decided at the outset to maximize the production of K^0 's by using dense targets and to forego the advantages of hydrogen production kinematics. The usual technique of a coincidence counter before the target and a veto counter behind it was employed to select neutrals in the forward direction.

In order to fit the leptonic decay distributions to X using the functions N^+ and N^- , it is necessary to know where $t = 0$ is for the data used in the fit. A systematic error of 0.4 cms along the beam in the average K^0 production point changes ReX by .01, whereas ImX is not sensitive to this. X is relatively insensitive to the higher moments of the production point distribution. A target length of 3.0 cms was chosen. This was short enough so that the average K^0 -production point could be determined accurately enough and decays could be seen well within the first K_S lifetime (12 cms). This target length is a reasonable fraction of an interaction length for the denser metals.

It remained to decide on the material, the transverse dimensions, and the number of targets. Considerations involved are:

- (1) Total K^0 -production for a given incident pion flux.
- (2) Net acceptance through the apparatus of K_{e3} 's from these K^0 's. Different materials may produce K^0 's with different momentum and angular distributions.
- (3) Trigger rate given that (1) and (2) are satisfactory.
- (4) Multiple scattering and attenuation of the beam as it

passes through the targets, causing it to miss later targets.

- (5) Shadowing effect of a target on decays occurring upstream from it. This increases with transverse size of the target.
- (6) It was desirable to use the same material in all targets so that the K^0 production physics would be the same.

From runs with polyethylene, aluminum, brass and tungsten it was found that the number of neutral decays (vees) on the film per incident pion behaved as shown in Fig. 32. So (1) was not a strong factor in the choice of material. It was found that tungsten caused almost no beam to reach subsequent targets due to multiple scattering. With the same geometry, aluminum gave a higher K_{e3} triggering rate than brass because it converted fewer of the γ 's produced in it. These converted elsewhere in the apparatus, triggering the gas Cerenkov counter.

The final target configuration, previously shown in Fig. 4, was two brass targets 1.2" (3.0 cms) long, the first one 1.26" in diameter with its center 72" from the magnet center, and the second one 0.75" in diameter, 48" from the magnet center. An added feature was a disk of lead 0.2" (1 radiation length) thick between each target and its veto counter to help reduce the K_{e3} triggering rate by converting γ 's produced in the brass. The counters C_1 , C_2 , V_1 , and V_2 were all coupled by air lightpipes to a 1.0" diameter lucite rod lightpipe which led to RCA 7850 phototubes placed outside the magnetic field region. Air lightpipes were used to reduce the material in the decay region. The phototubes had their last few dynodes connected to

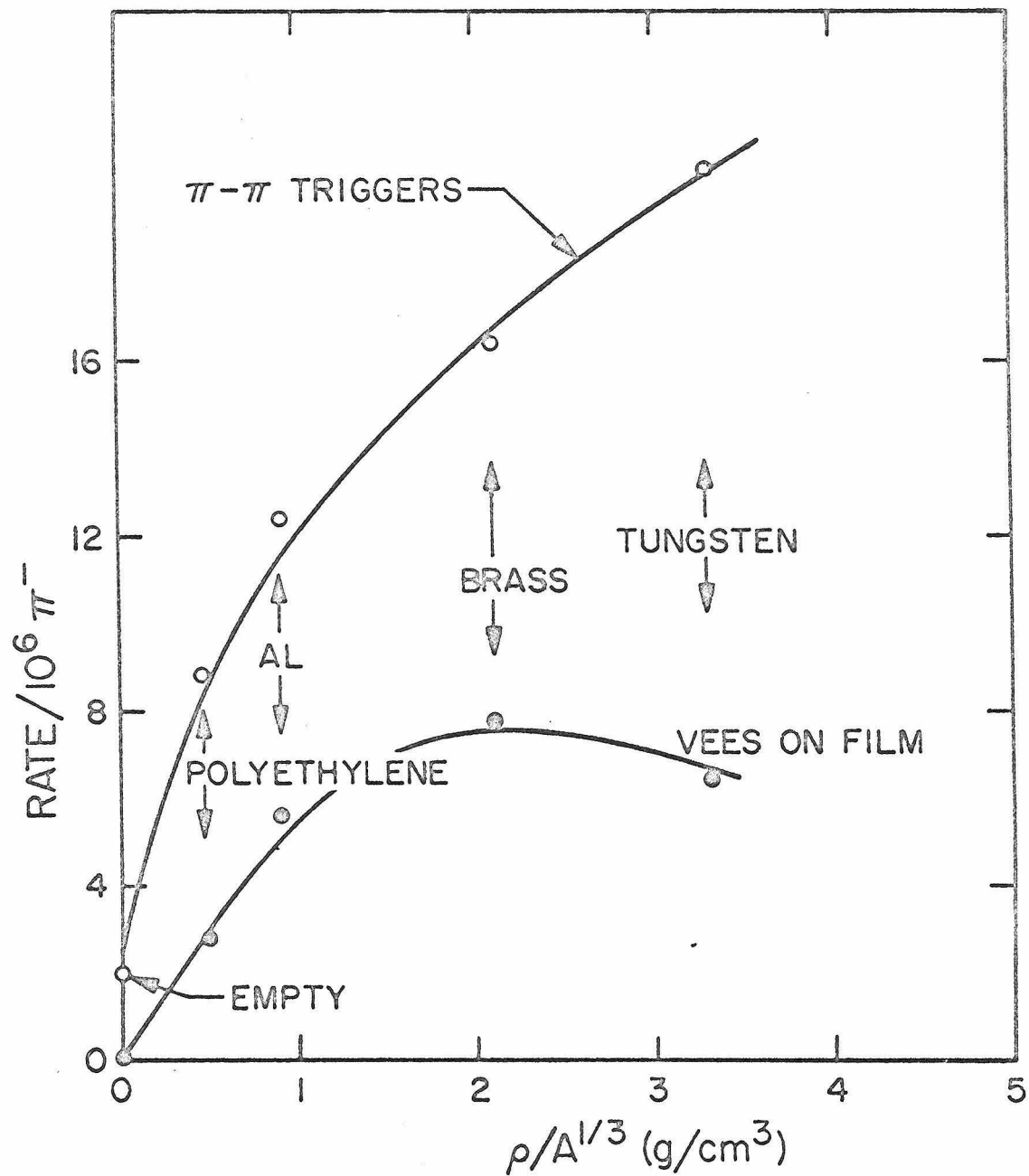
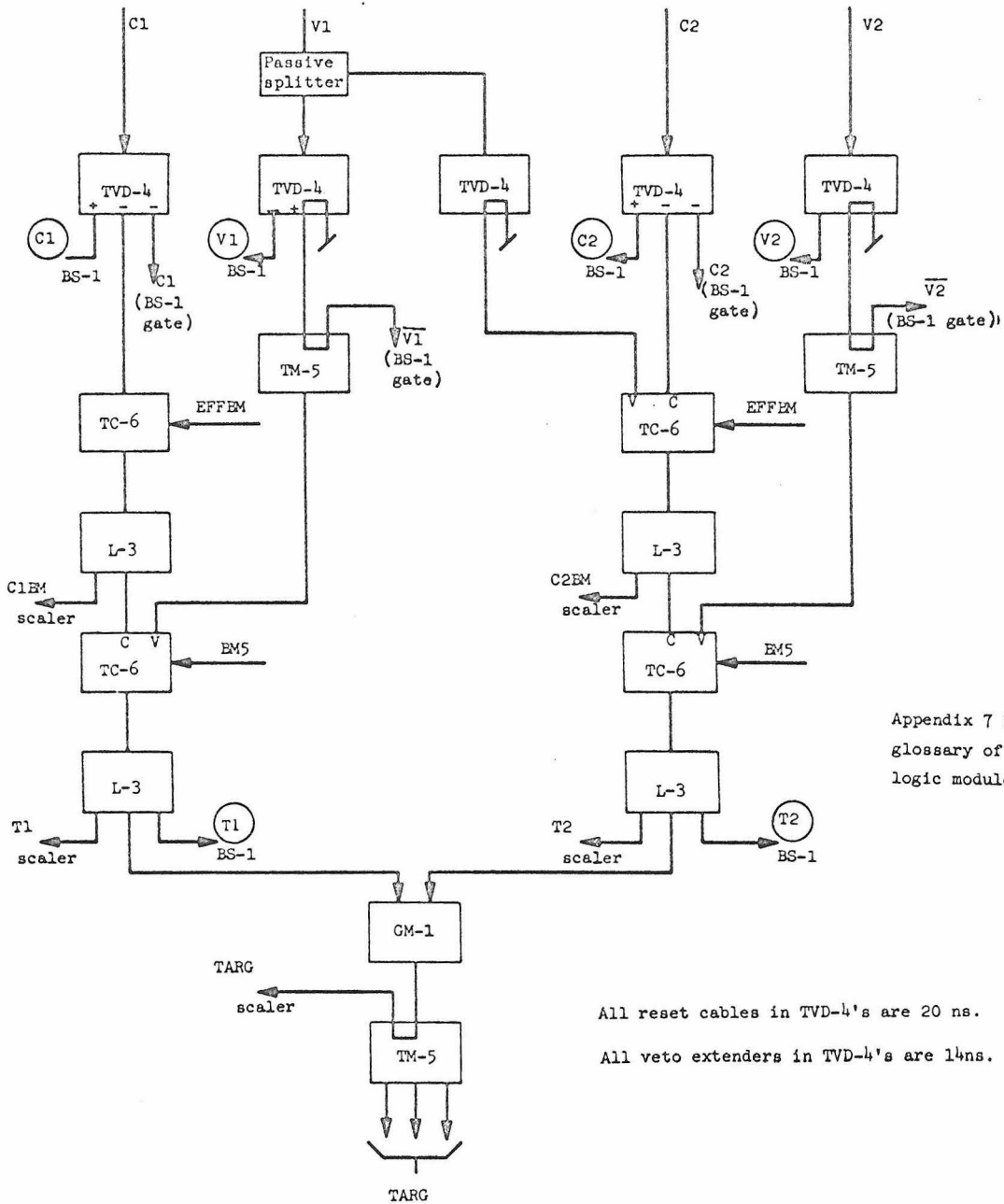


Fig. 32 Number of vees on film and $\pi\pi$ trigger rate for different target materials

a condenser bank to handle the high counting rates. These counters had efficiencies $> 99\%$. The counters were centered on the targets by pins which were placed in holes drilled halfway into the counters. The upstream target was suspended from an adjustable mounting bracket, whereas, to cut down on material in the decay region, the second target was actually supported by the air lightpipes. These were folded from 0.01" mylar and so had good mechanical rigidity.

A block diagram of the fast logic analyzing the signals from C_1 , C_2 , V_1 , and V_2 is shown in Fig. 33. Note that the signal from V_1 is split; one half goes to a TVD-4 set at a bias $> I_{\min}$ whose output vetoes C_2 . This prevented interactions in the first target from giving spurious triggers in the second target.



Appendix 7 has a glossary of fast logic modules.

All reset cables in TVD-4's are 20 ns.
 All veto extenders in TVD-4's are 14ns.

Fig. 33

Block diagram of target electronics

Appendix 4: Spark Chambers

There were three distinct sets of spark chambers in the apparatus which will be now separately described.

Production-decay Chambers

The production and decay of K^0 's was viewed by seven spark chamber modules. Each module was 18" x 8" x 4" and had 11 active $\frac{1}{4}$ " gaps. The first target was between the first and second modules, and the second target was between the fifth and sixth. Each plate had a total of .0015" aluminum and was stretched over a window frame shaped brass rod which was filled out in the middle by crinkled .0015" Al foil. Each module presented 0.01 radiation lengths of material to particles passing normal to the plates. The plates could slide in and out of the lucite box which formed the shell of the module, so that defective plates could be removed by simply opening up the module and replacing a plate. The whole assembly of chambers, high voltage condenser banks, targets, target counters, as well as S4 and S4V were mounted on a cart which ran on rails 8' above. This cart could be rolled in and out of the magnet with ease and allowed convenient access to the components on it as well as clearing the way to work on the apparatus inside the magnet.

The gas mixture used in these chambers (also in the momentum and shower chambers) was commercial 90/10 Ne-He mixture which was purified and recirculated. Each chamber was driven with 3.9 μ f. of capacitance charged to 9 Kv. and pulsed by spark gap in parallel with a shorting gap to provide uniformity of spark intensity. The delay

time at which the chamber efficiency dropped to 50% was measured to be 600ns. at the operating clearing field of 60V. The efficiency during operation for two tracks was 99%, but with competition from extra heavily ionizing tracks it deteriorated.

The tracks on the film were located in space using two kinds of fiducials: full fiducials and transfer fiducials. The full fiducials were a carefully surveyed set of aluminum strips with notches cut every 4" and were lit from behind by luminescent panels. Since these large area panels could not be pulsed at the rate at which pictures were taken, there was also a set of transfer fiducials consisting of smaller panels which could be rapidly pulsed and so photographed on every frame. The transfer fiducials were measured whenever a frame was measured and then the reconstruction program could refer them to the surveyed full fiducials using measurements made when both sets were lit. The full fiducials were securely attached to the magnet whereas the transfer fiducials were mounted on the mobile cart.

Because the chambers had only 9" vertical clearance down to the coil cover of the magnet, it was necessary to split the plan view of the chambers with a V-shaped mirror and combine these two halves at a later stage in the optics. This realistic film format made it easier to scan the decay region for neutral vees. It was felt that high visibility of low intensity sparks would aid in scanning, so an f-2.5 lens was used in the camera which viewed these chambers. The camera was a 35mm. Flight Research model 207 which

could pulse 15 times/sec. giving a deadtime of 70ms..

The chambers were removed at the end of the data-taking and a large illuminated lucite sheet, with a $\frac{1}{2}$ " x $\frac{1}{2}$ " cartesian grid etched on it, was inserted and photographed through the optics in both views at many distances from the camera. In this way, locations of optic axes could be found accurately. Significant distortions were discovered and carefully mapped out by this grid photography. A correction scheme was devised in the decay region reconstruction program and, using this, the position accuracy determined from straight through tracks was ± 0.08 ", ± 0.11 " for transverse position Y and Z respectively, and ± 0.01 radians for angular measurements, which is fairly typical spatial resolution for optical spark chambers.

Momentum Chambers

These chambers were placed in the region of highest field of the M-5 magnet and provided most of the information used for the measurement of the decay secondary momenta. There were four chambers in all: a front chamber, FM, was 8" x 24" with six $\frac{1}{4}$ " gaps and was placed between the S5 counter and the entrance window of the gas counter; the middle chamber, MM, was at the center of the magnet, immediately behind the MH, and was 60" x 18" with four $\frac{3}{8}$ " gaps and, finally, at the back of the magnet were placed the rear chambers, RMN and RMS, each 36" x 60" with six $\frac{3}{8}$ " gaps. The chambers were constructed with plates which consisted of an aluminum-styrofoam-aluminum sandwich, the aluminum being 0.0005" foil and the styrofoam $\frac{1}{8}$ " thick. Such plates are easy to handle and were set into lucite

frames without having to stretch and maintain taut large areas of aluminum foil. Each plate presented $.007 \text{ gms/cm}^2$ to incident particles, so the full set of momentum chambers presented $.6\%$ of a radiation length to particles normal to the plates.

The FM chamber was pulsed from $3.9\mu\text{f.}$ charged to 9 Kv., MM from $2 \times 3.9\mu\text{f.}$ at 12 Kv., and the two RM chambers were each pulsed from $3 \times 3.9\mu\text{f.}$ at 12 Kv.. The gas mixture was the usual 90-10 Ne-He. The fiducials were similar to those of the production-decay chambers, with transfer and full fiducials on all chambers. Each chamber was looked at in the plan and elevation views by optics of high quality bolted securely to the magnet. The Flight Research model 207 camera was also bolted to the magnet. There were considerable variations in spark intensity for different views on the film and it was felt that making all views equally bright would make it easier to measure the film. A plate of grey filters was mounted about 10' from the camera to give the desired uniformity of intensity on the film. The transverse position measurements were $\pm 0.03''$ in the FM and RM chambers, $\pm 0.06''$ in the MM chambers, but the angular measurements were poor $\gtrsim \pm 1^\circ$, due to the short track lengths and the staggering of successive sparks by the crossed magnetic and electric fields. However, the chambers were primarily used to measure the sagitta of the orbits and the momentum resolution obtained was $\Delta p/p \sim 5\%$.

Shower Chambers

The shower chambers were used to study the interaction of the decay secondaries in three radiation lengths of lead and con-

sisted of six modules, three on each side of the center line. They were located with the normal to the plates at 16° to the center line so that, on the average, the decay secondaries would be at normal incidence. Each module was 4' x 6' and contained nine plates each formed of an Al-Pb-Al sandwich. There were six active gaps in each module, so a non-interacting track would give 18 sparks in traversing the array. The plates had .02" of Al on either side of .02" Pb, the sandwich being glued together with epoxy and pressed in a very large area hydraulic press to ensure flatness. The modules were mounted on a mobile cart which could be moved to provide access to the apparatus at the rear of the magnet.

The gas mixture was 90-10 Ne-He and each module was pulsed from a 4 x 3.9 μ f. condenser bank charged to 12 Kv.. As with the other chambers, there were carefully surveyed full fiducials and the usual supplementary transfer fiducials pulsed for every frame. The chambers were viewed in the plan and elevation views. The optics were not as good as for the other chambers since there were many large area mirrors mounted on a scaffold constructed from steel tubing which was not entirely rigid. The camera was again a Flight Research model 207. The position measurements had resolutions $\pm 0.2''$ and angles were measured to ± 0.02 radians. As mentioned in Chapter III, these measurements were of small weight once the momentum chambers were included in the fitting, but did serve as a starting point. The identifying power of the chambers for π 's and e's will also be discussed in that chapter.

Appendix 5: Freon Cerenkov Counter

A 1 atm. Freon 12 Cerenkov counter was used for electron detection. At 1 atmosphere $n_{\text{Freon 12}} = 1.00105$ which gives a Cerenkov threshold velocity of $\beta = 1/n = .99895$ corresponding to $\gamma = 21.9$. This gives threshold momenta of $p_e = 11.1 \text{ MeV}/c$, $p_\mu = 2.29 \text{ GeV}/c$, and $p_\pi = 3.02 \text{ GeV}/c$. With an incident beam momentum of $2.85 \text{ GeV}/c$ only electrons will directly count in the counter; any other particles triggering it through electron generation. For $E_e \gg m_e$, $\theta_C^2 = 2(n-1) = .0021$, so $\theta_C \approx .05 \approx 3^\circ$.

The gas was contained in an aluminum box 18" x 35" x 60". The front and back panels, which had openings, were 3/4" Al and the other sides were all 1/4" Al. The entrance and exit windows consisted of black mylar 0.02" thick. A sketch is shown in Fig. 34. The mirrors on which the Cerenkov light was first incident were 1/8" thick lucite spherical mirrors attached to adjustable mounts which could be manipulated from outside without opening the counter. The light then bounced back into one of the two lightpipes and ultimately into the phototubes. The lightpipes were constructed from a synthetic fibre soaked in epoxy and cast into shape, the end result being like fibreglass. The sections just before the phototube were parabolic in shape with a focus at the phototube. The parameters of the parabola were optimized using a light ray tracing computer program and a cast of this shape was made by spinning a rough approximation to the shape at a certain speed and pouring epoxy on it. The epoxy then hardened to a parabola whose parameters depended on the velocity of rotation.

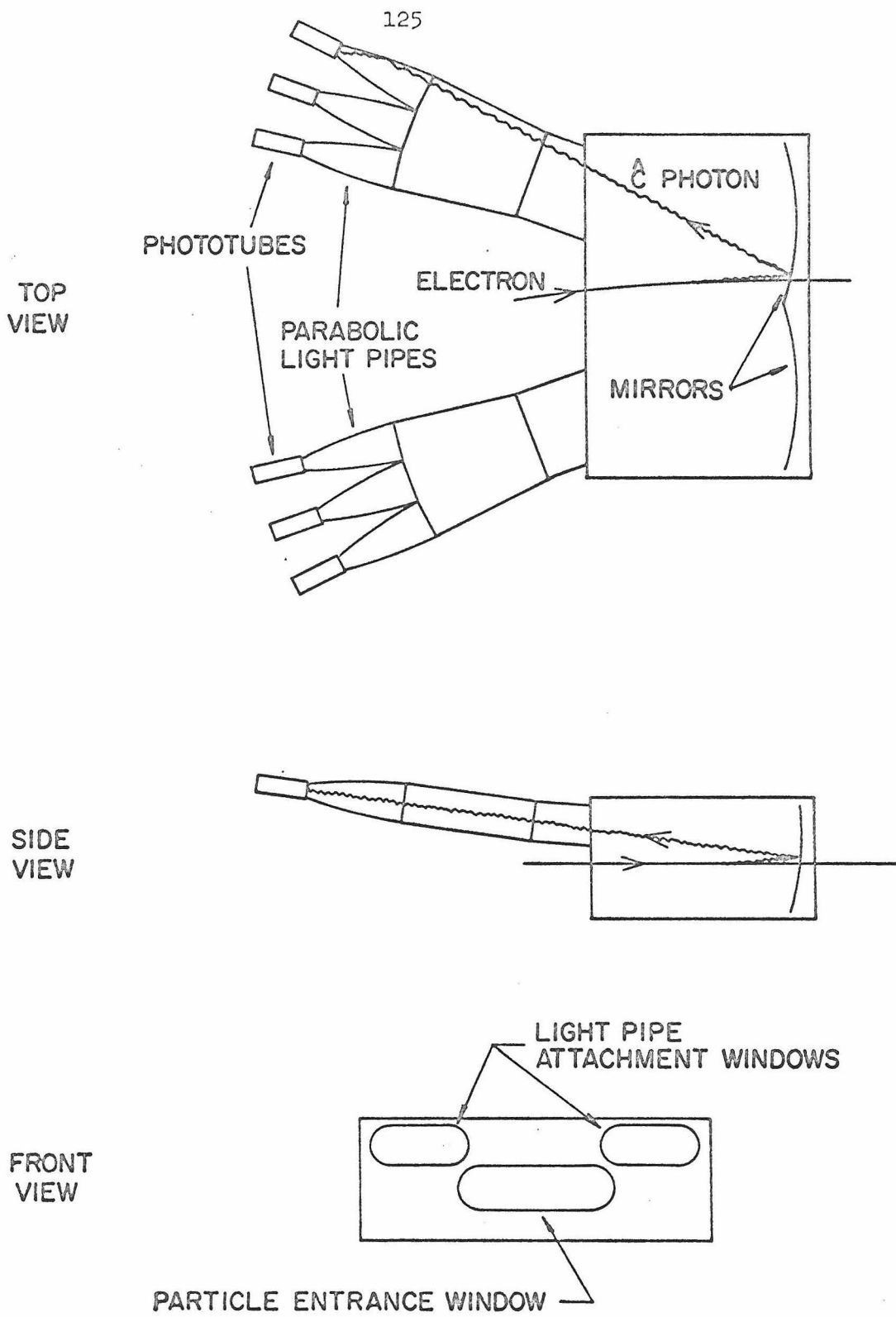


Fig. 34

Sketch of gas Cerenkov counter

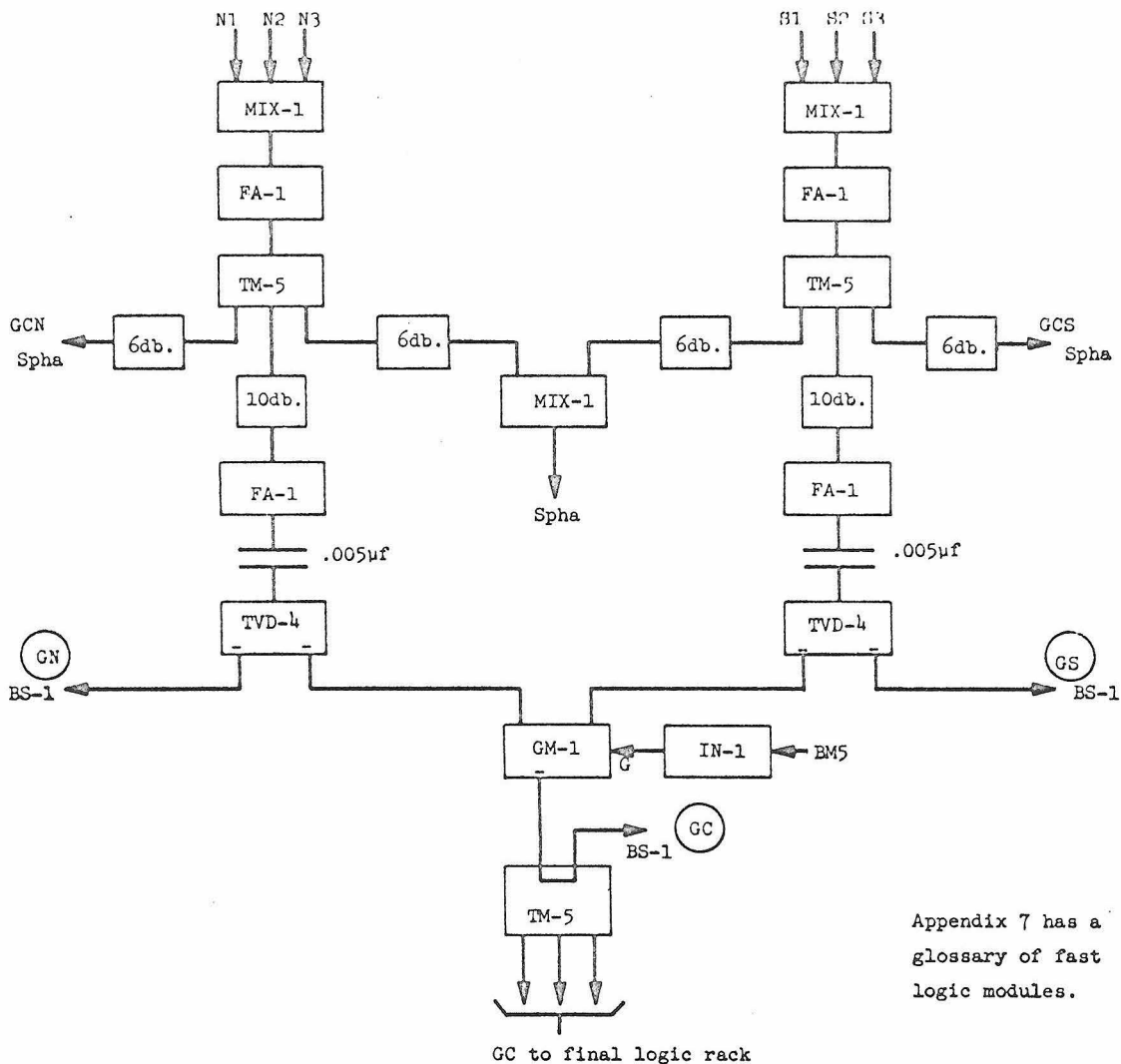
The phototubes used were RCA 8575 which had a measured photocathode efficiency of 28%. There were three phototubes on each side. They were in a region of relatively high field and were shielded with $\frac{1}{2}$ " thick soft steel tubing. The counter was bolted to a set of rails attached to the coil cover of the magnet.

The counter was originally tested with 1.0 GeV electrons at the Caltech synchrotron. The counter was not in a magnetic field and so the results of such tests are not obviously comparable to the conditions in the experiment. The best yield obtained in the electron beam was a distribution which corresponded to a Poisson with $m = 9$. If one assumes no other broadening, this gives nine photoelectrons from the RCA 8575 phototubes. The actual distribution from the counter for the final K_{e3} data is shown in Fig. 16, Chapter III.

To get the narrowest distribution when summing phototubes the gains must be equalized. To do this with the six phototubes of the gas counter, it was necessary to have some well defined reference signal. For this reason, the phototubes had small pieces of plastic scintillator glued on the side of their photocathodes, with a Cs_{137} source attached. The gains were equalized at Caltech by moving the counter relative to the electron beam so that all the Cerenkov light shone on one phototube at a time. The gains were adjusted to get the same mean pulse height from each tube, and then the ratios of the signals from the sources were noted. Thus, while running at Berkeley, the gains could be equalized by getting the signals from the sources into that ratio. For example, when the magnetic field polarity of

the M-5 magnet was changed, the gains of the phototubes changed slightly and the source signals were used to bring the six phototubes back to equal gains.

The electronic circuitry that analyzed the phototube signals is shown in Fig. 35. As can be seen, the three signals on each side were first added and then fast amplified (MIX-1 and FA-1). They were then separately pulse height analyzed and also the sum pulse height analyzed. After another stage of fast amplification, the signals went to a TVD-4 discriminator set at a very low bias and if either of these triggered in coincidence with the beam a signal GC was generated and sent to the final logic rack. The distributions of pulse heights for the separate sides and the sum were stored in the PDP-8 computer while running. It could be inspected on a CRT display and provided a good check that the counter was operating normally.



Appendix 7 has a glossary of fast logic modules.

Fig. 35 Block diagram of gas Cerenkov counter electronics

Appendix 6: Hodoscopes and Shower CountersMultiples Hodoscope

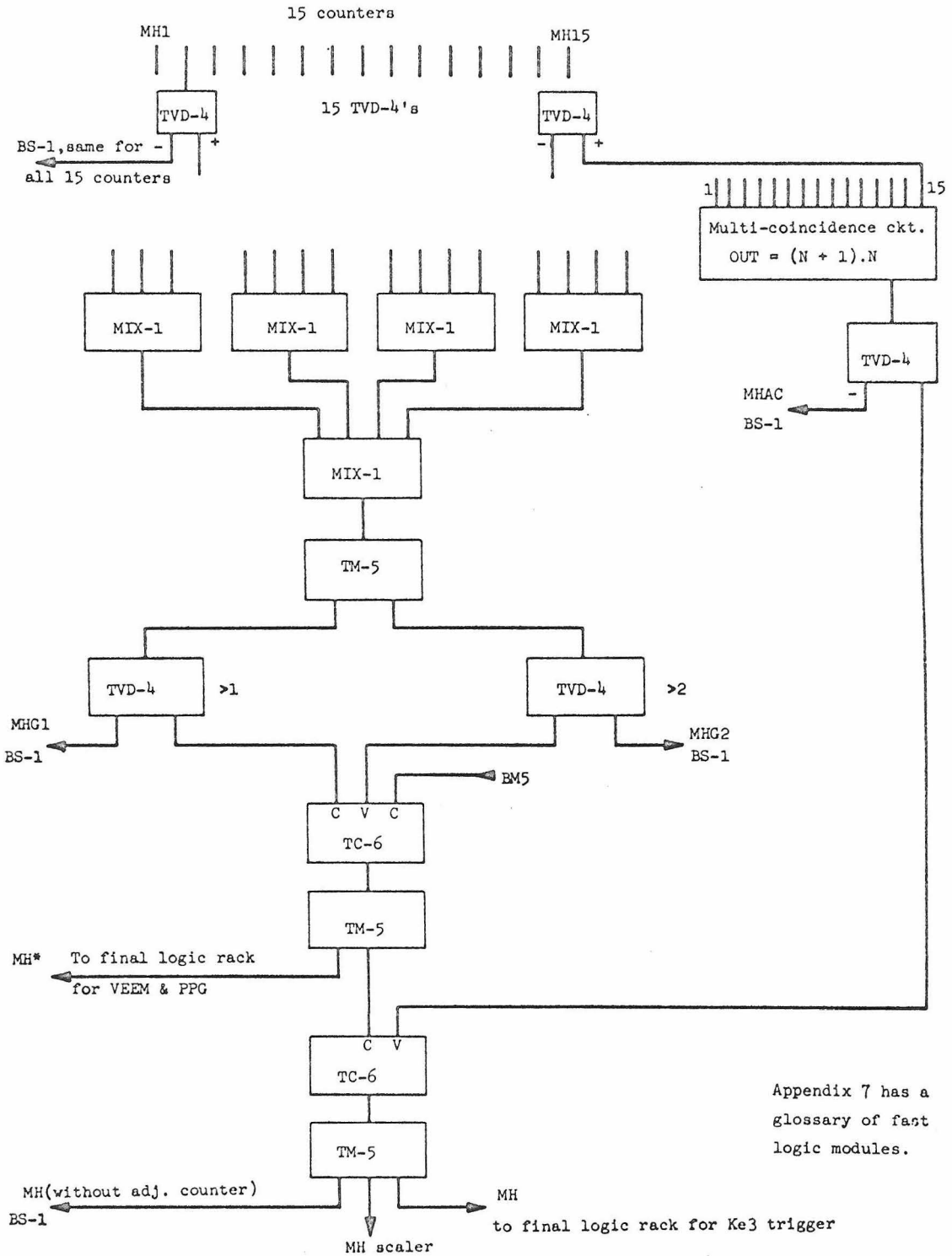
The multiples hodoscope, MH, was a set of fifteen horizontal 60" x 1" x 3/8" scintillators made from Pilot Y which has good attenuation characteristics. The hodoscope was placed perpendicular to the beam 8.7" downstream from the magnet center. Each counter had a 6655A phototube which was mounted in a gap between two sections of the magnet yoke where the field was relatively low and heavy shielding was not necessary. The pulse height distribution, from the end of a counter away from the phototube, was a Poisson for which the mean, m , was greater than 20 and rose to 60 at the end near the phototube. This meant that the counters could be operated with an efficiency $> 99.9\%$ from all parts of the counter. A check of the uniformity of response of the counters comes from the profile of accepted events at the MH, in which no bias along the counters can be seen.

A block diagram of the MH electronics is shown in Fig. 36.

There are three basic signals:

- MHG1 : 1 counter triggered.
- MHG2 : 2 counters triggered.
- MHAC : Adjacent counters triggered.

The signal $MH^* = MHG1 \cdot \overline{MHG2} \cdot BM5$ was used in the general VEEM trigger and also in the PPG trigger for the $K^0 \rightarrow \pi^+ \pi^- \pi^0$ experiment being run in parallel. For the K_{c3} (PIE) trigger, the signal used was



Appendix 7 has a glossary of fast logic modules.

Fig. 36

Block diagram of MH electronics

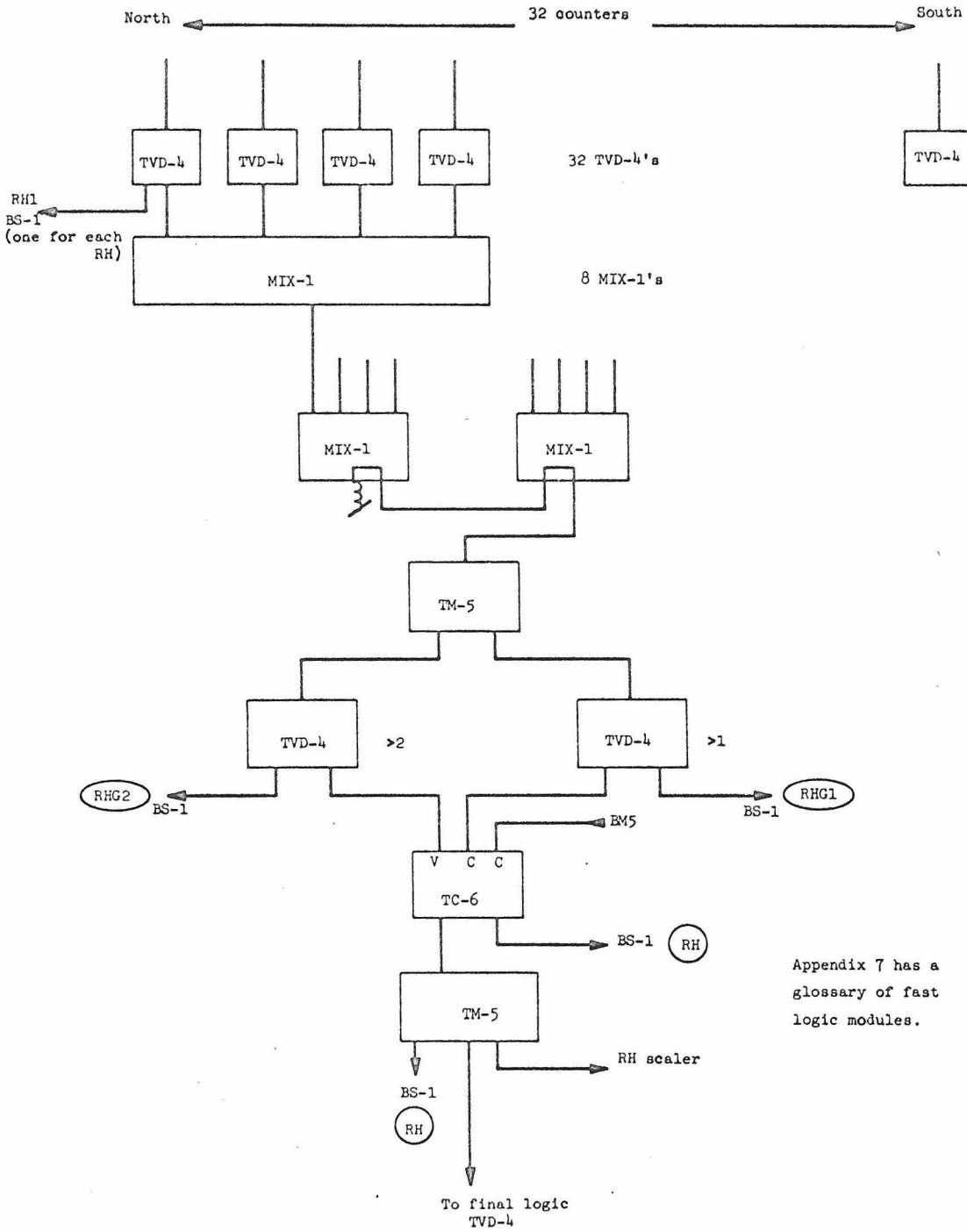
MH = MHG1.MHG2.MHAC.BM5, the MHAC signal being generated by a multi-channel coincidence circuit which gave an output when adjacent counters fired.

Rear Hodoscope

The rear hodoscope, RH, consisted of two sections each having sixteen 42" x 4" x $\frac{1}{4}$ " Pilot Y scintillators arranged vertically, with phototubes at the bottom. Each side had its normal at 16° to the center line and was mounted, together with its phototube shielding, on the mobile cart which also supported the shower chambers and shower counters. The apex where the two sides met was 84.4" downstream from the magnet center. A block diagram of the electronic circuitry which analyzed the RH signals is shown in Fig. 37. As in the MH case, the basic signal, RH, is formed thus: RH = RHG1.RHG2.BM5. In this case there is no restriction on adjacent RH counters firing. Each RH counter had above it a light, visible in the shower chamber optics, with the counter number on it. This light flashed on when a picture was taken, if that counter had triggered, and was very useful in picking out the triggering tracks when scanning the shower chamber film.

Shower Counters

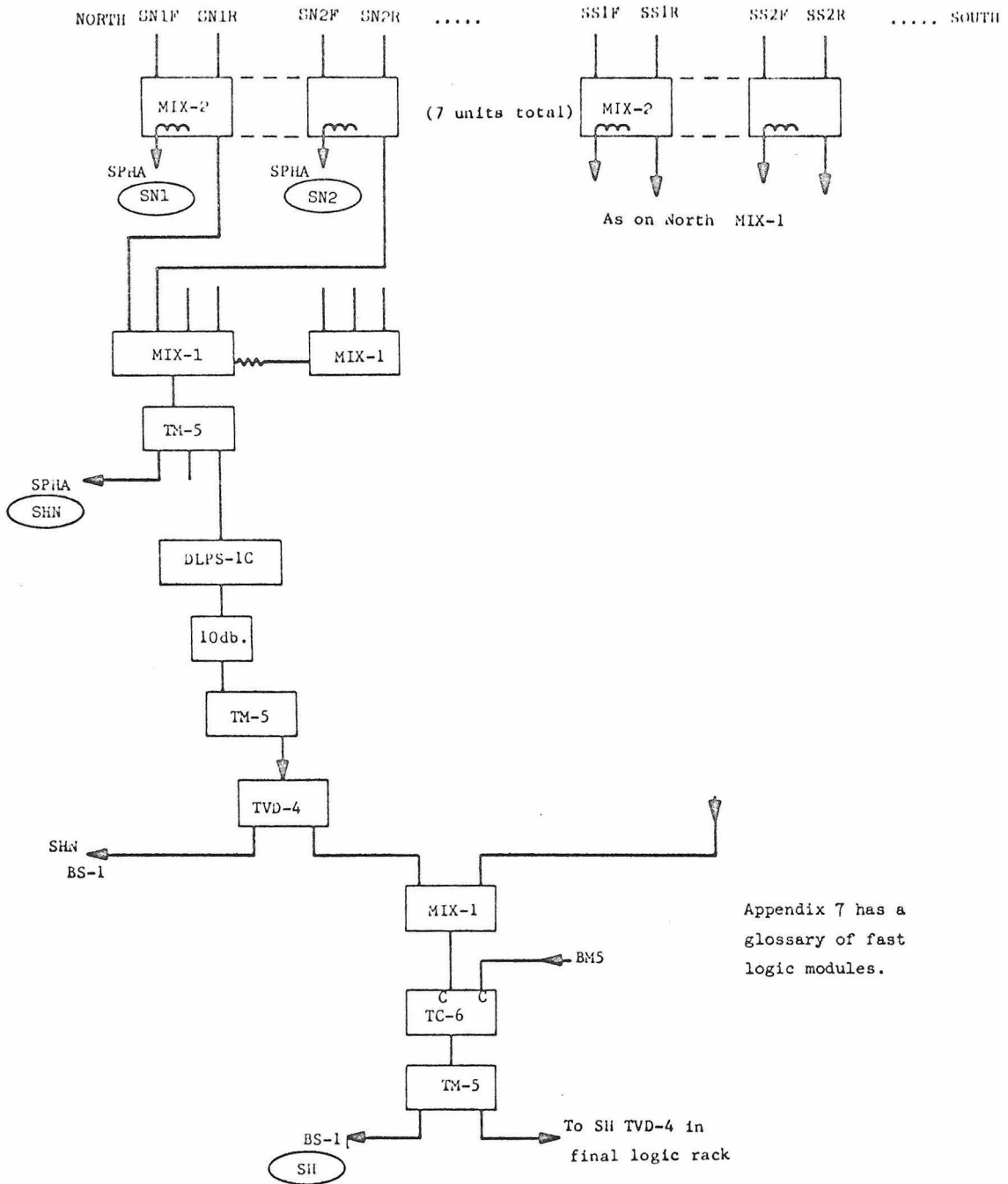
The shower counters immediately behind the shower chambers, consisted of fourteen modules, organized in two seven-module sections, one on each side of the center line with their normals at 16° to the center line. Each module had two scintillator slabs, one with its lightpipe on top, the other with lightpipe on bottom and with 0.4"



Appendix 7 has a glossary of fast logic modules.

Fig. 37 Block diagram of RH electronics

lead between the scintillators. The slabs were 52" x 10" x 3/8" Ne 102 scintillators with lightpipes attached at 90° to keep the assembly compact. The lightpipes were placed at opposite ends to average over the attenuation of signals along the counter. The 0.4" of lead was glued between 1/4" layers of styrofoam backed with aluminum sheeting and the whole assembly, scintillators and lead, was bolted to a frame and mounted on the mobile cart. The electronic circuitry which interfaced these counters is shown in Fig. 38. Since each module was separately pulse height analyzed it was necessary to match the gains of the fourteen modules. Minimum ionizing particles gave a very noticeable peak (see Fig. 6, Chapter III) in the pulse height spectrum and the high voltage on the 6655A phototubes was adjusted to place these peaks in the same channel for all modules. The pulse height spectrum could be displayed from the PDP-8 while running and this also provided a check on the stability of the counter gains.



Appendix 7 has a glossary of fast logic modules.

Fig. 38

Block diagram of SH electronics

Appendix 7: Fast Electronics and Trigger Logic.

The fast electronics used standard modules built at Caltech which have been described in detail in CTSL Internal Report No. 31. A brief glossary of these circuits will help in understanding the electronics block diagrams:

FA-1	Fast amplifier; DC coupled, gain 10, - input, - output, risetime 2.3 ns..
TVD-4	Fast discriminator, DC coupled, input -.05 to -1V, output rise and fall time 2 ns., output length(7 ns. + reset cable length).
L-3	Limiter, DC coupled, shapes pulses for use in TC-6, risetime 2 ns..
TM-5	DC coupled fast multiplexer for digital signals.
TC-6	4-channel coincidence or anticoincidence circuit, resolving time 2 ns..
GM-1	Gated mixer, can also be used as a flip-flop.
IN-1	Inverter.
MIX-1	Mixer.
DLPS-1C	Delay line pulse shaper.
DTG-1	Deadtime generator.

The fast logic was organized into seven racks: Trigger, Beam, GC, RH, MH, SH, and Target. All except the final trigger rack have already been described in Appendices 2, 3, 5, and 6. A block diagram of the trigger rack is given in Fig. 39. The signals TARG,

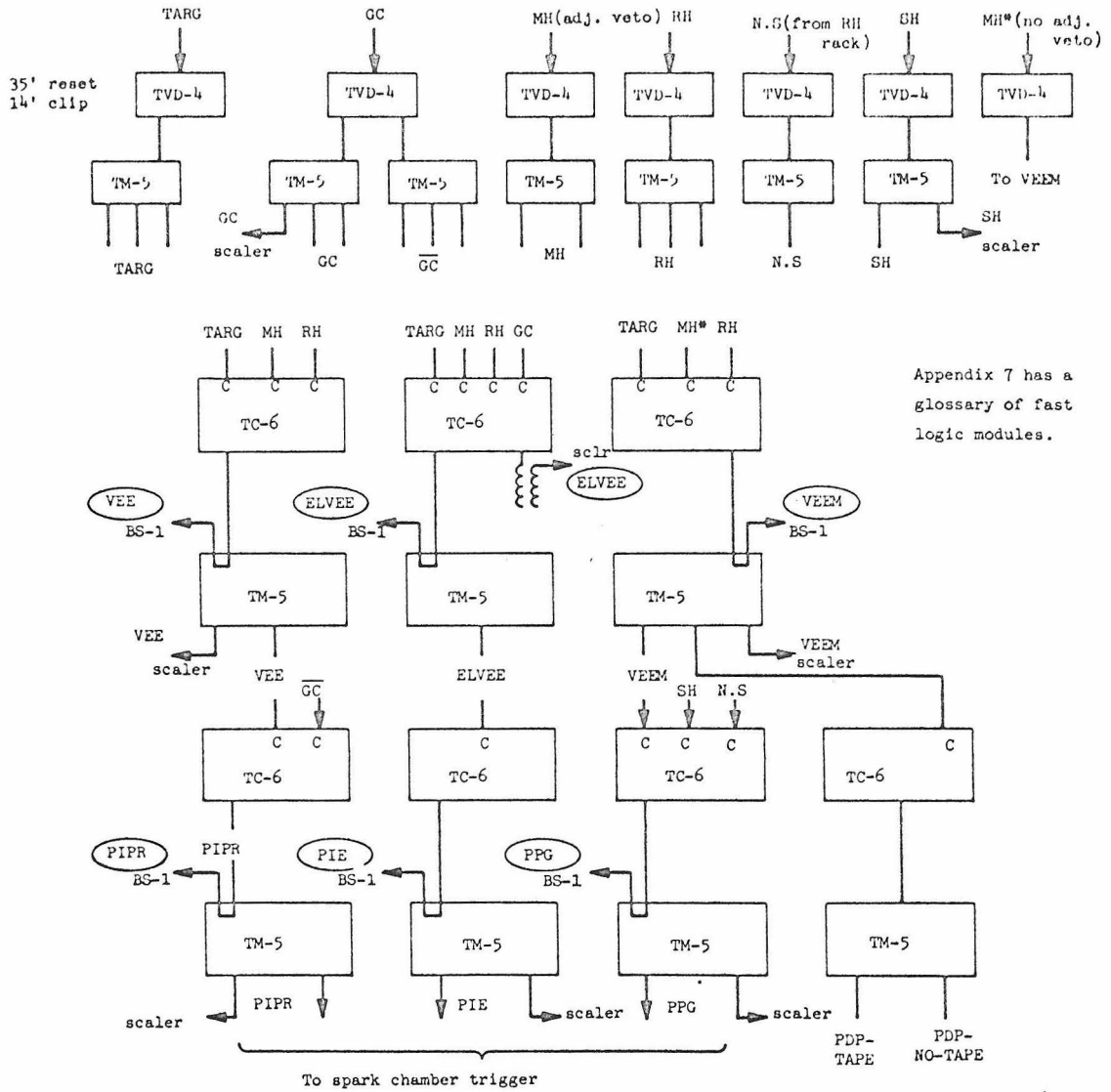


Fig. 39 Block diagram of trigger electronics

GC, MII, RII, and SII were all about 10 ns. long when they arrived at the trigger rack. Accidental rates in the logic were negligible since the beam was always $< 500\text{K}$ per sec. and was usually without excessively spiked RF structure. Table 8 has a list of all fast logic signals.

The normal "DATA" run trigger was (PIE + PPG), normal "CALIBRATION" run trigger was VEE before 2/2/68, VEEM after 2/2/68. The TAPE trigger was always VEE before 2/2/68, always VEEM after 2/2/68.

TABLE 8. FAST LOGIC SIGNALS

*Indicates that the signal was scaled and logged.

BEAM	*S1.S2 S3.S4	} used for beam tuning and as a control room monitor
	BEAMDT	300ns. generated by $(C_1 \cdot \overline{V_1} + C_2 \cdot \overline{V_2})$
	*EFFBM	= BM. \overline{BEAMDT}
	*BM5	= EFFEM.S5
TARGET	*C ₁ BM	= C ₁ .EFFEM
	*C ₂ BM	= C ₂ .EFFEM
	*T1	= C ₁ . $\overline{V_1}$.BM5
	*T2	= C ₂ . $\overline{V_2}$.BM5
	TARG	= T1 + T2
	*GC	= GCN + GCS
MH	MHG1	= > 1 counter from MH
	MHG2	= > 2 counters from MH
	MHAC	= Adjacent MH counters fired
	*MH	= MHG1. $\overline{MHG2}$. \overline{MHAC} .BM5
	MH*	= MHG1. $\overline{MHG2}$.BM5 (also called MHWOS)
RH	RHN	= signal in RH 1-16
	RHS	= signal in RH 17-32
	RHG1	= > 1 counter in RH
	RHG2	= > 2 counters in RH
	*RH	= RHG1. $\overline{RHG2}$.BM5

(continued)

TABLE 8. FAST LOGIC SIGNALS (Continued)

	{	*NS	=	RHN.RHS
SH	{	SHN	=	sum of North above TVD-4 threshold
		SHS	=	sum of South above TVD-4 threshold
		*SH	=	(SHN + SHS).BM5
TRIGGER	{	*VEEM	=	TARG.MH*.RH
		*PPG	=	VEEM.SH.NS. \overline{GC}
		*VEE	=	TARG.MH.RH
		PIPR	=	VEE. \overline{GC}
		*PIE	=	VEE.GC
		*PDPEFFBEAM	=	EFFEM. ($\overline{\text{PDP}} \text{ downtime}$)
		*S.C.EFFBEAM	=	EFFEM. ($\overline{\text{spark chamber}} \text{ downtime}$)

Appendix 8: Slow Electronics and Computer.

An important part of the electronics was the interface between the fast logic and the PDP-8 computer. The fast logic pulses were ~ 10 ns. long, whereas the PDP-8 was a relatively slow computer with a 4K memory and a $1.5\mu\text{s}$. memory cycle time. The digital information was read from the fast logic racks into BS-1 Buffer Storage circuits. The analog counter pulses were pulse height analyzed by 64-channel Slow Pulse Height Analyzers called SPHA's. These circuits were all clamped while the spark chambers were firing. When the electrical noise had died down, the BS-1 and SPHA information was read into the PDP-8 accumulator by a read control circuit. The resident PDP-8 program, EXPO, was then interrupted at whatever task it was engaged in and began storing the fresh data in its memory. When several events had been accumulated, they were written out on magnetic tape on a DATAMEC D2020 tape unit. The tape I/O was double-buffered so that it gave a negligible contribution to the overall deadtime. The EXPO program could histogram any data the experimenter called for through the teletype and display the result on a CRT. This program has been described in detail in DECUS No. 8-161.

Besides being stored on tape, some of the BS-1 information was put directly on film so that it would be available while scanning. This was done by having the BS-1 information activate relay switches in series with data lights visible to the cameras. These data lights were luminescent panels similar to those used for the transfer fiducials. The circuitry for these lights, which involved

many poorly shielded cables around the spark chambers, was electrically isolated from the BS-1 and fast electronics by coupling the two with miniature bulbs shining on LASCR's.

The film advance for the three cameras was governed by a camera control circuit which controlled camera deadtimes, etc., and prevented the spark chambers from triggering unless the cameras were ready. In between machine pulses this circuit triggered a loop generator on the cameras which pulled out a loop of ten frames so the delicate camera mechanism did not have to pull film directly off the 1200' roll in the magazine.

Appendix 9: Data-taking Procedures and Checks.

The usual spark chamber trigger was (PIE + PPG) and the tape trigger, at the beginning of the 4-month run, was VEE, later changed to the more general VEEM. After about 12 hours of data taking with this trigger a short calibration run was taken, triggering the spark chambers as well as the tape on VEEM which gave many $K_S \rightarrow 2\pi$ events needed for the Monte Carlo efficiency calculations. While running, a continuous run-by-run log was kept of all rates that were scaled (normalized to the total number of beam particles). Any discrepancies in these rates were investigated and the trouble cured before resumption of data-taking. The BS-1 and SPHA information was being logged by the PDP-8 and could be displayed on the CRT. The appearance of these histograms was a good indication of how the counters were working and one could find out very quickly if a counter were maladjusted or totally turned off. The apparatus was visually checked at least every eight hours while running. Spark chamber performance, fiducial and logic lights, and camera operation were all checked. The developed film was also spot-checked for spark-chamber efficiency, burnt out data lights, etc.. The field polarity of the M-5 magnet was reversed every few days, amounting to twenty-five times during the data-taking run. A record was kept so that the total amount of data at each polarity was equal. The magnet current was monitored to 0.1%.

Appendix 10: Scanning Procedures.Tape Scan

The analysis of a tape record is demonstrated in Fig. 40 with the aid of a sample event. The RH counters triggered were 12 and 22. The pulse height in each of the fourteen shower modules is given above the module. The first step is to search for an "electron" -- an adjacent pair of modules with pulse height > 14 ($1.7 I_{\min}$). Pairs 4-5, 5-6, and 6-7 are looked in behind RH 12, and 9-10, 10-11, and 11-12 are looked in behind RH 22. An "electron" is found in 4-5, 5-6, 6-7, 9-10, and 10-11. Next, the "pion" search looks for individual modules with pulse height between 4 and 21 ($0.5 - 2.6 I_{\min}$) and < 5 ($0.6 I_{\min}$) in the modules on either side. The "pion" search is unsuccessful in 4, 5, and 6 behind RH 12. It is similarly unsuccessful in 9 and 11, but finds one in 10 behind RH 22. So, the event is accepted with an "electron" behind RH 12 and a pion behind RH 22.

It was stated in the text that there was no evidence for any decay-length dependent biases in the tape scan and this will now be demonstrated. Fig.'s 41 and 42 show histograms of electron and pion pulse height for four intervals of decay position (first target only) from the final data: 5" - 15", 15" - 25", 25" - 35", and 35" - 45". The mean pulse height in each of these intervals is 46.0, 48.3, 50.6, 50.3 for electrons, and 17.1, 18.1, 19.5, 19.1 for pions. Since the variations in the average are well within the width of the distribution for each case, it is concluded that there

Computer scan analysis of S.N. 910742,
 event accepted with electron behind
 RH 12 and pion behind RH 22.

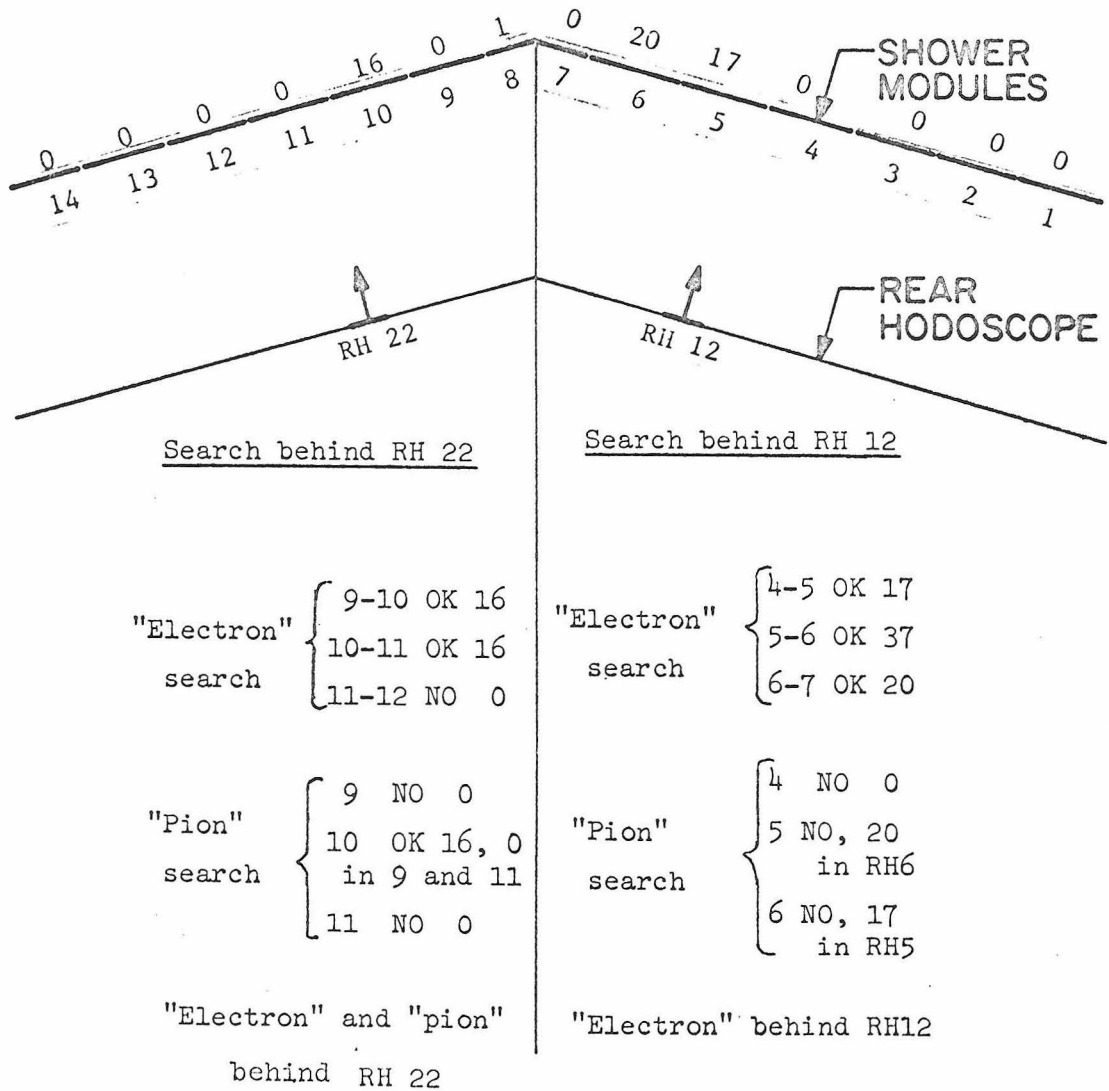
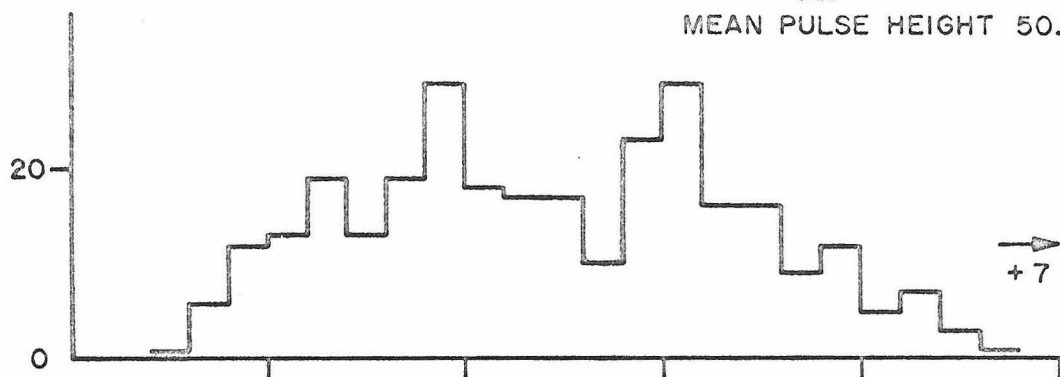
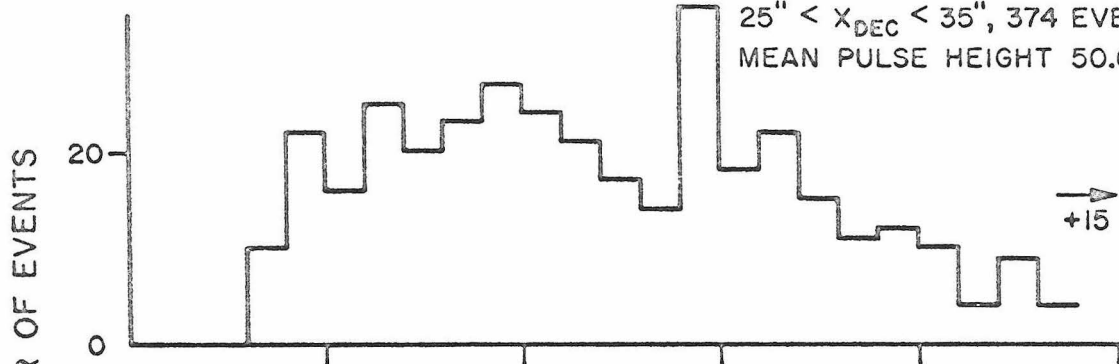


Fig. 40 Computer scan analysis of a K_{e3} trigger

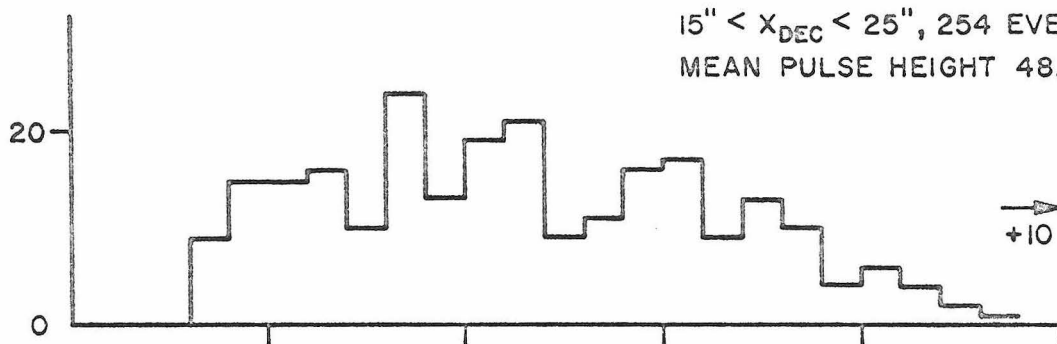
$35'' < X_{DEC} < 45''$, 302 EVENTS
MEAN PULSE HEIGHT 50.3



$25'' < X_{DEC} < 35''$, 374 EVENTS
MEAN PULSE HEIGHT 50.6



$15'' < X_{DEC} < 25''$, 254 EVENTS
MEAN PULSE HEIGHT 48.3



$5'' < X_{DEC} < 15''$, 151 EVENTS
MEAN PULSE HEIGHT 46.0

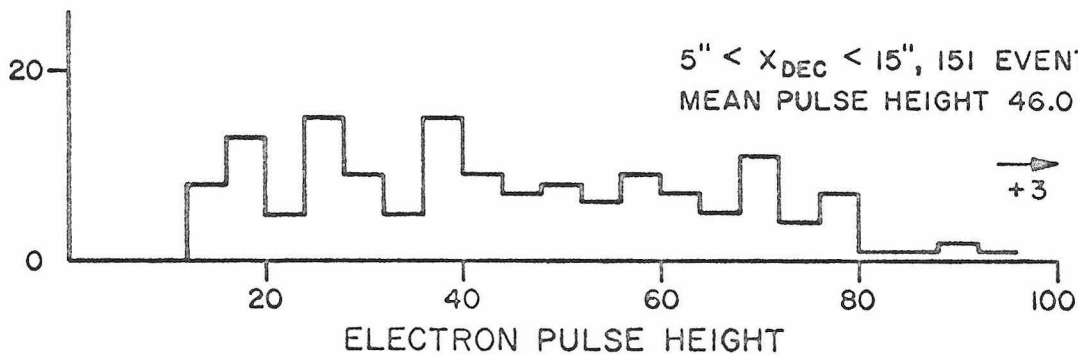


Fig. 41

Electron pulse height in shower
counters for four segments of
decay region

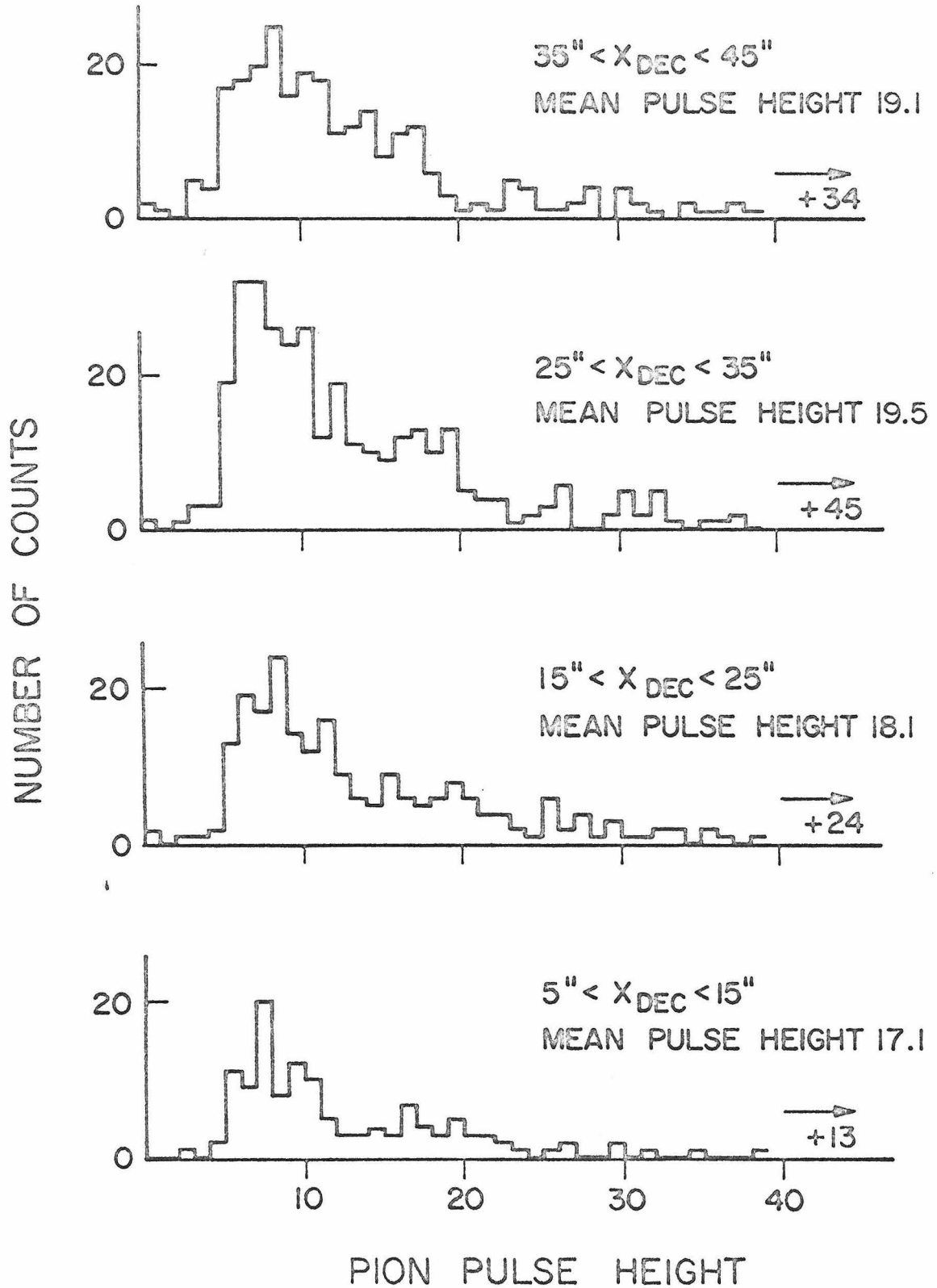


Fig. 42 Pion pulse height in shower counters
for four segments of decay region

is no evidence for any systematic position-dependence in the pulse height spectrum of either electrons or pions.

Another possible source of bias would arise if the electron-pion separation at the shower modules were dependent on decay length in the front end. When the electron and pion are near one another, the pion could add its pulse height to the electron giving a pulse height above threshold to events that would otherwise fail, since a pion search is not made when the RH separation is ≤ 4 . This question was investigated using Monte Carlo events, dividing the decay region into three segments and histogramming the electron-pion separation in each segment. These are shown in Fig. 43. There is no statistically significant difference between these histograms.

Charge biases in the computer scan were investigated by histogramming separately the pulse heights of e^+ , e^- , π^+ and π^- from the final data. These are shown in Fig. 44 and there is no demonstrable difference between distributions for different charge states.

Fig. 45 shows the acceptance of the computer scan as a function of electron energy. Low energy electrons reach shower maximum well before three radiation lengths and so give a very small pulse in the shower counters. This efficiency was used as a correction in the Monte Carlo program.

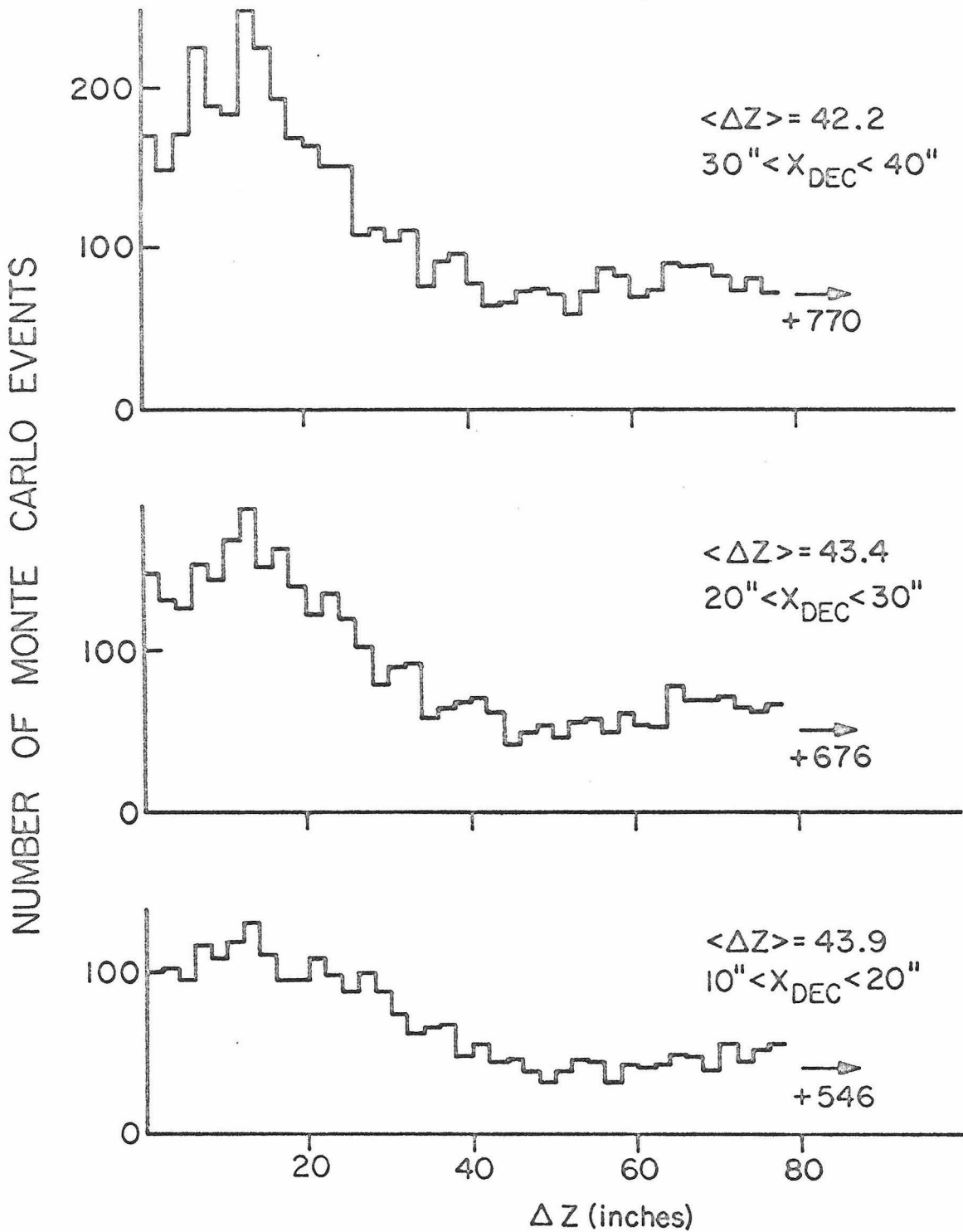


Fig. 43 Horizontal separation between pion and electron at shower counters

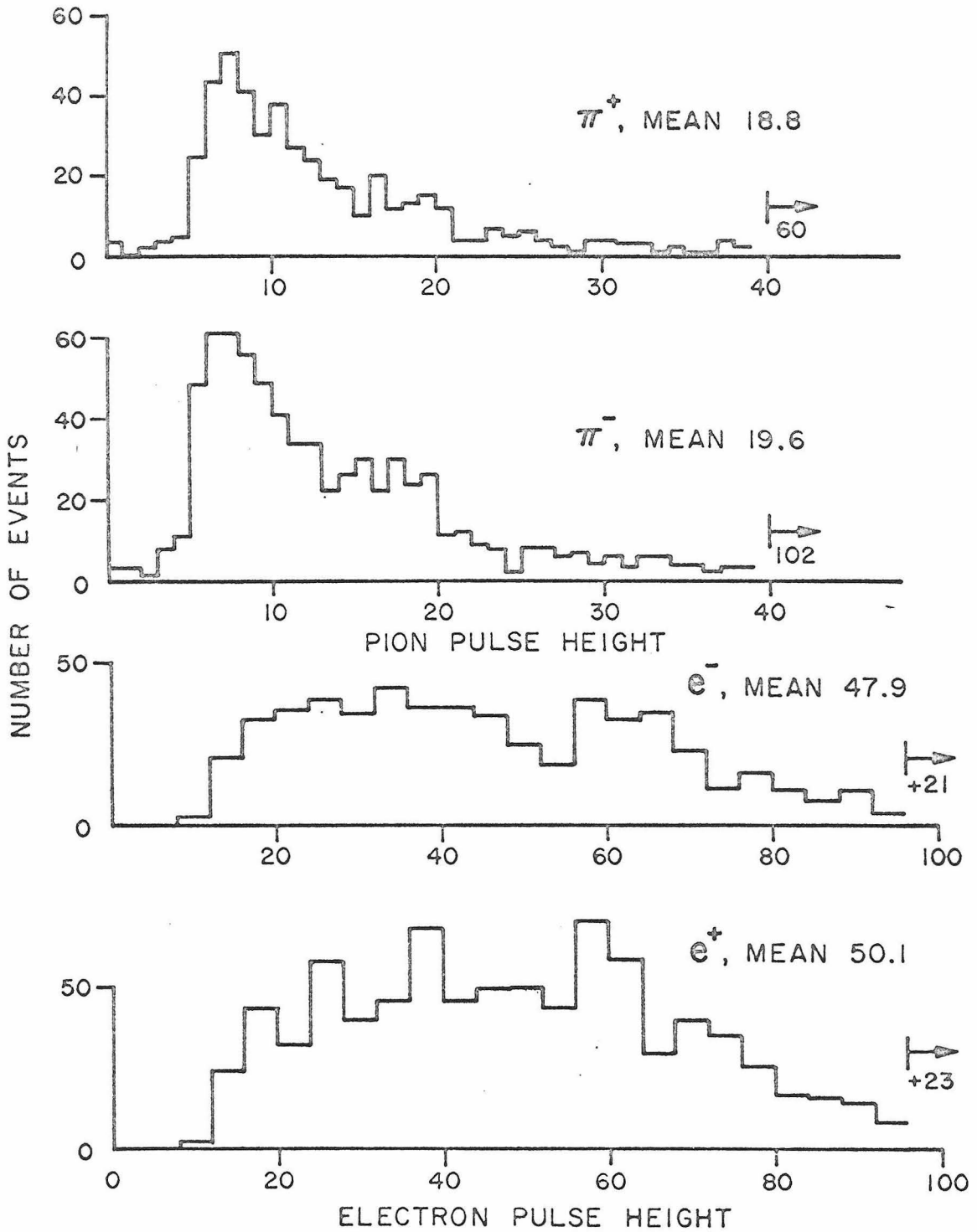


Fig. 44 Shower counter pulse heights of e and π for different charges

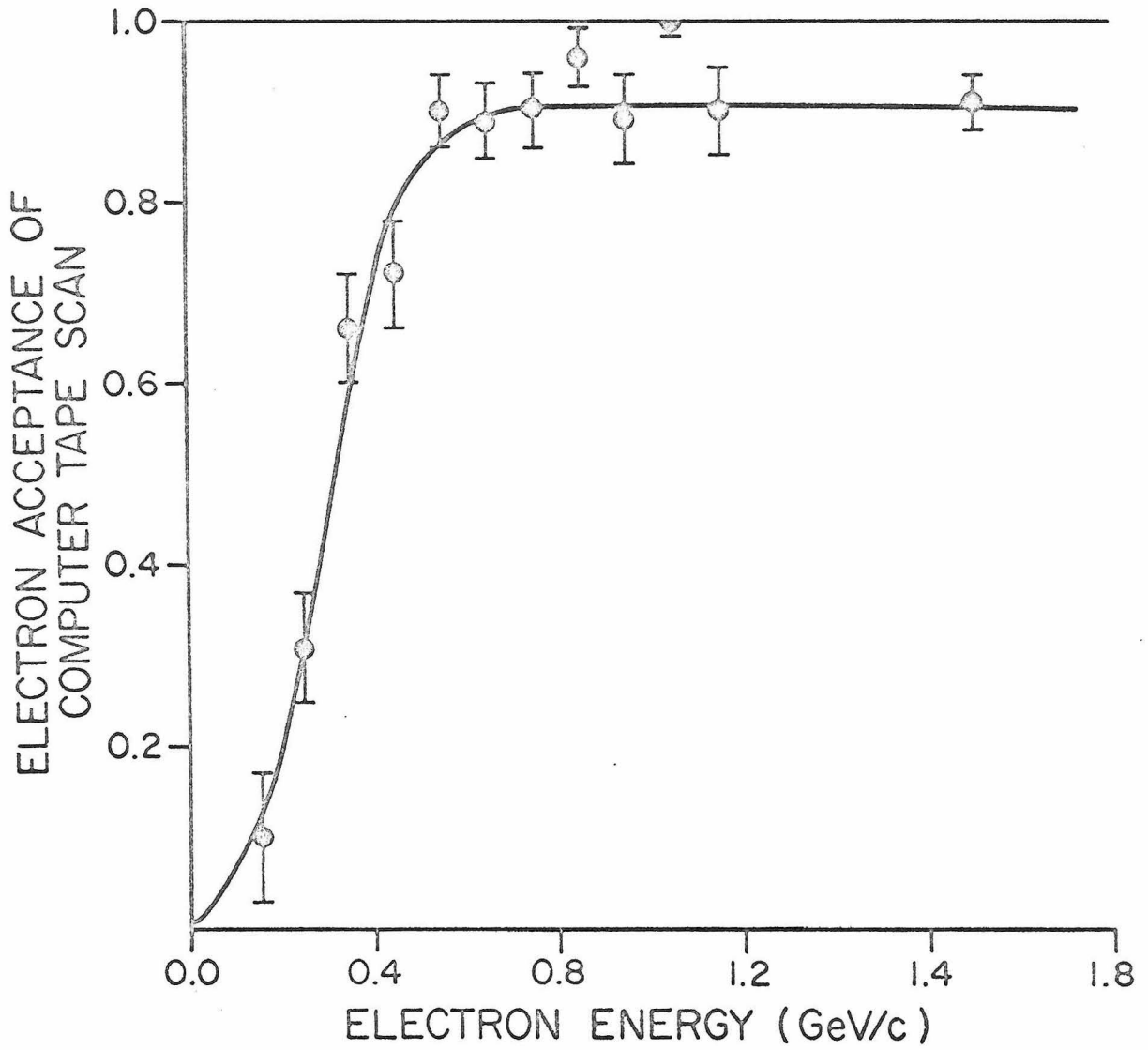


Fig. 45 Electron acceptance of computer scan as a function of electron energy. Smooth curve is to guide the eye.

Shower Scan

The actual scanning instructions given to the scanner are reproduced here, with Fig. 46 for illustration.

"Shower Scanning Procedure for K_{e3}

The primary object of this scan is to pick up events in which a pion and an electron have triggered the shower detecting part of the apparatus. If the event is not π -e combination but can be classified π - π , then it is also included and its type noted.

Find the RH counters from the computer output and look for the tracks in the shower chamber which extrapolate into the RH counters on the scanning template. The tolerance for this is $\pm \frac{1}{2}$ counter on either side of the triggered RH counter. If a unique π -e combination can be found, a pion in one counter and an electron in the other, then the event is accepted. If there is an ambiguity where two pions or two electrons are within the limits of the counter, then the event is rejected as ambiguous (if one of these ambiguous tracks is within $\frac{1}{2}$ counter but not actually inside, then take the one that is inside and accept the event).

Pion criteria:

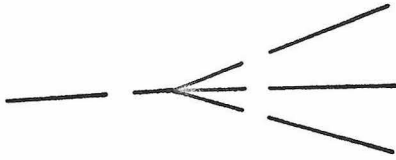
1. Straight through tracks.
2. Tracks scattering at a definite point, with straight segments.
3. Tracks with an interaction where a number of straight



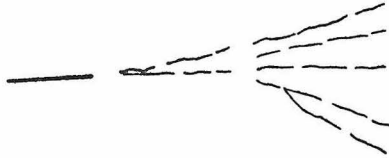
1. Straight through tracks



2. Tracks scattering at a definite point with straight segments



3. Tracks with an interaction where a number of straight tracks emanate from a definite vertex



4. Example of a shower

Fig. 46 Shower scanning criteria

tracks emanate from a definite vertex.

Electron criteria:

Any track which satisfies none of the pion criteria and is not an obvious stop, i.e., a straight track which stops at a definite point in the chambers. In general, an electron is characterized by extra curving tracks coming off at small angles."

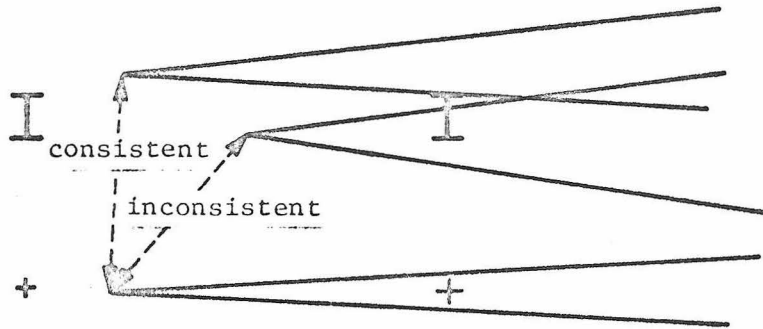
Decay Region Scan

The actual instructions used by the scanners are reproduced here, with Fig.'s 47 and 48 for illustration.

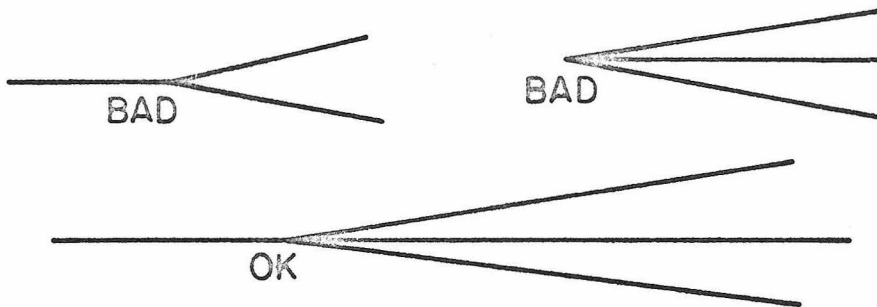
"K_{e3} Scanning in the Front End

From the computer output find the two MH numbers and insert the pins in the appropriate holes. Move the strings attached to the pins over the elevation view until the tracks associated with these MH counters are identified. For T1 events the tolerance is ± 2 counters; for T2 it is ± 3 counters. If these two tracks satisfy the following:

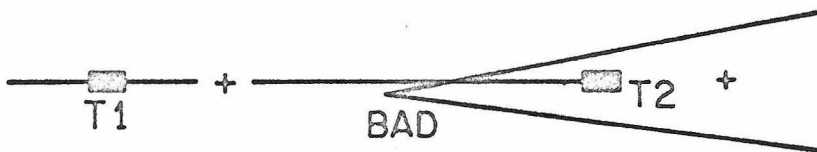
- a) Are reasonably straight, with no scatter $> 5^\circ$.
- b) Form a consistent vertex in both views, at the same position along the beam within a few gaps (be liberal when tracks are on opposite sides of split in the plan view).
- c) There are no other tracks stopping or starting at the vertex either from upstream or going downstream (tracks going right through vertex do not affect event).



a) Vertex consistency between plan and elevation views



b) Extra tracks at vertex



c) Vertex position relative to triggered target (example is a T2 trigger)

Fig. 47 Production-decay region
scanning criteria

- d) The vertex must not be upstream (to the left in picture) of the target which triggered.

If a) through d) are satisfied, then check the event on the scan list and write down an estimate of the chamber number and plate number of the vertex.

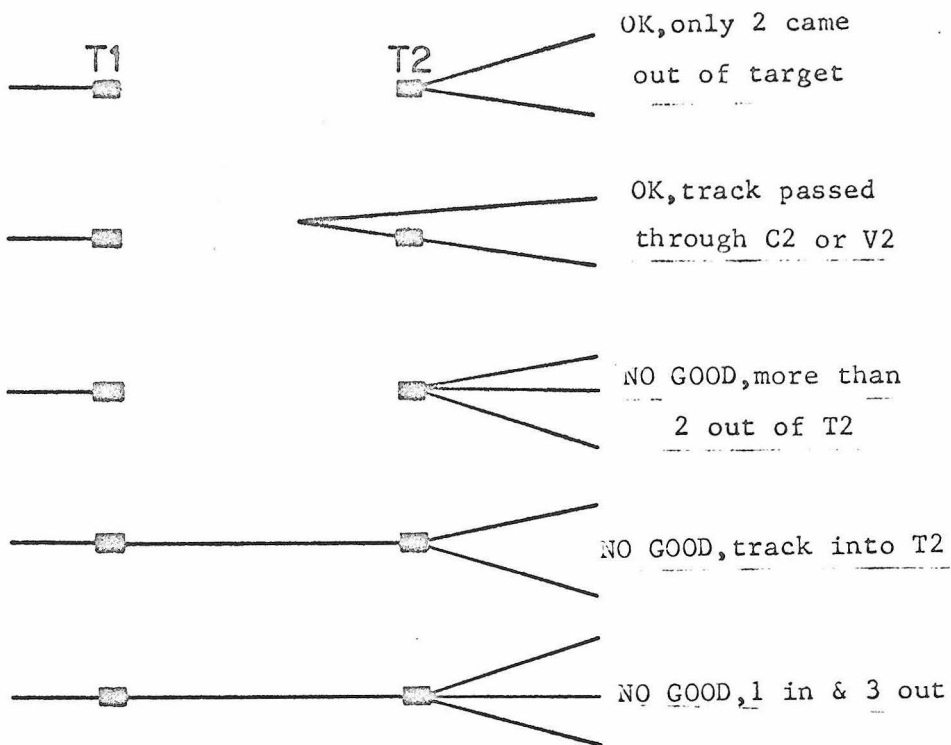
The following special cases are illustrated in Fig. 48.

1. C₁V₂ or C₁C₂V₂ events

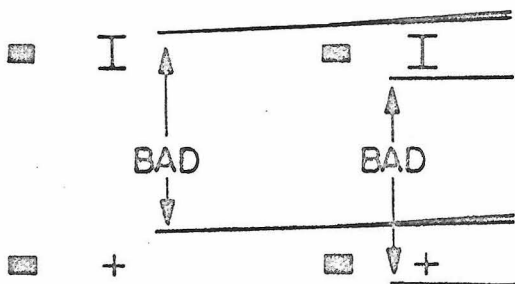
These events are to be treated by the same rules as the regular vees with the addition that if a track appears to pass right through the vertex then the event is rejected.

2. Small opening angle events

For events with vertex upstream of T2, reject the event if there is no opening for at least two chambers in both views. For events downstream (to the right in picture) from T2, there must be evidence of two separate tracks for the event to be acceptable."



1. T1 events where either C2 or V2 fired



2. Small opening angle events

Fig. 48 Special cases in production-decay region scan

Appendix 11: Measuring, Reconstruction and Track Fitting.

This Appendix describes how measurements from the three 35mm. frames taken for each event were used to reconstruct the trajectories of the decay secondaries in the magnetic field.

For each measuring machine a program, COVTUV, was written to transform the numbers, encoded in the digitization process, into two cartesian coordinates and an angle on the measuring table. The overall calibration of each machine was regularly checked by placing an accurate cartesian grid in the film clamp and digitizing many points and angles. These measurements were analyzed by a checking program using the same version of COVTUV that was being used to analyze the data. Over the period in which the data pictures were processed, no significant drifts were found in the calibration of the measuring machines.

Measurement of a decay region picture will be taken as an example of the spark chamber digitization process. Fig. 49 (a) shows an example of a production-decay region picture; Fig. 49 (b) shows a frame for which the accurately surveyed full fiducials were lit along with the transfer fiducials. The measuring procedure for data frames was to make twelve position-angle measurements in the order indicated. When measuring transfer fiducials, the position only was measured by simply placing the measuring arm cross-hair at the point to be digitized. In measuring decay secondary tracks, the cross-hair was placed as close as possible to the decay vertex. For each run, a few sets of full fiducials were measured in the order indicated in (b).

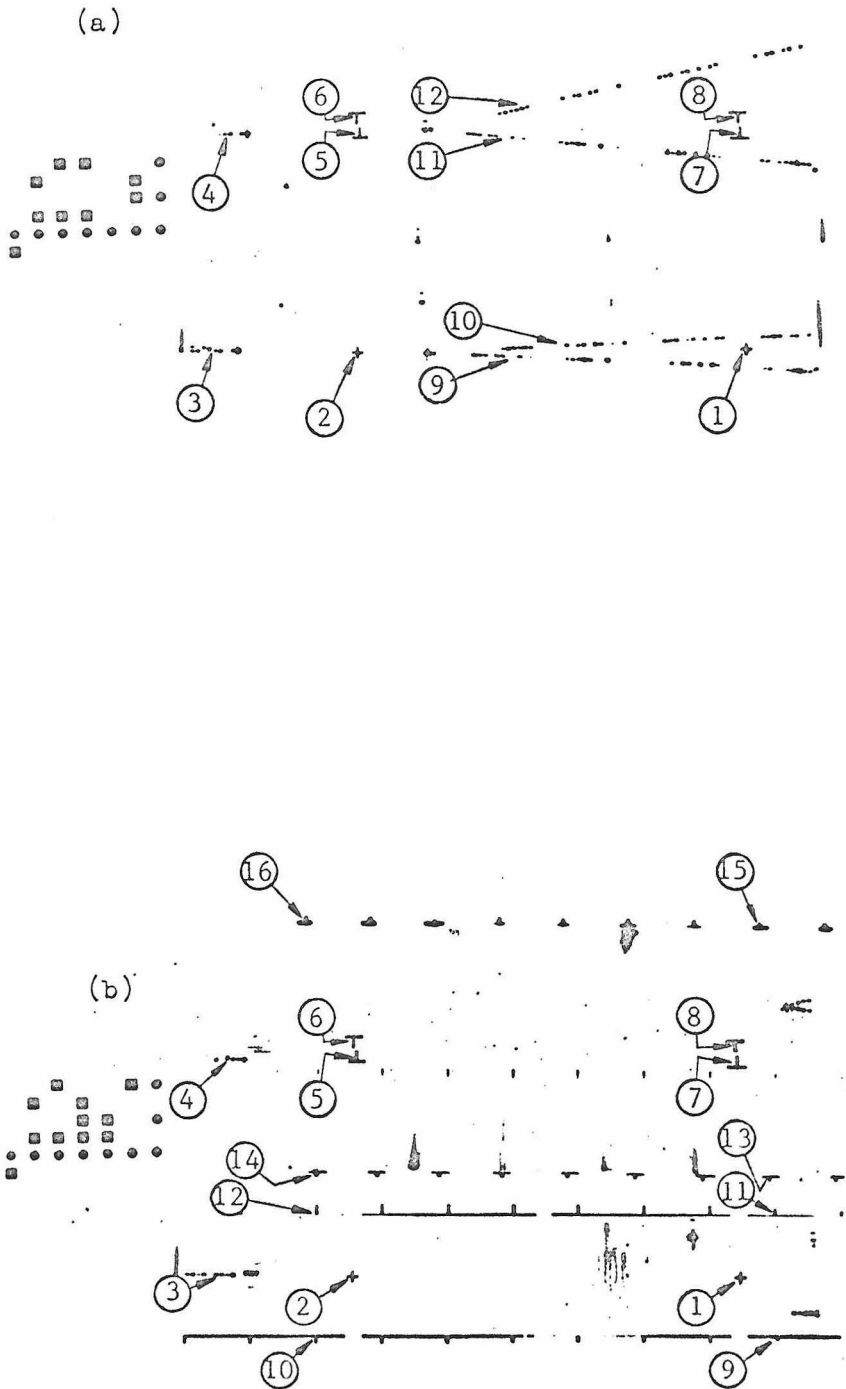


Fig. 49 Production-decay region measurements : (a) Normal data frame; (b) Full fiducial frame. Numbers indicate measuring order.

A set of about ten full fiducials was collected by duplicating those measured in adjacent runs. Any variations in the optics took place on a long time scale relative to the few hours it took to collect a data run, so it was reasonable to combine full fiducial measurements from three adjacent runs.

In analyzing a set of data measurements, the first step was to use the full fiducial measurements to calculate for each view the magnification from the table to real space and the location of the optic axes relative to the transfer fiducials. The average over the ten frames was used to avoid sensitivity to single measuring errors. The optic axes for the plan and elevation views intersected rather closely in space. The measurements were analyzed to find the equation of the tracks projected onto the planes containing the optic axes, with the transfer fiducials as a reference. It is then a matter of algebra to calculate the equation of the track in three dimensions. The optic axis locations were known from the surveying so this 3-D equation could be transformed to a standard coordinate system whose X-axis was along the beam, Y-axis in the vertical direction, Z-axis perpendicular to these two and whose origin was located 80" upstream from the magnet center. The procedure in the momentum and shower chambers was similar so that all shower chamber tracks could be geometrically reconstructed in a common coordinate system.

The process described so far involved programs consisting of about 3,000 cards of Fortran and used a large number of parameters measured in the survey of the apparatus at the conclusion of the

experiment. There are limitless possibilities for both programming and surveying errors in this scheme, and it is clearly desirable to have enough direct checks to tie the process together. This was provided by runs of straight through tracks, where the apparatus was triggered on interactions in the targets with the magnetic field turned off. Measurements of the track of the same particle made in different chambers were fit to a straight line. Using a sample of 1,000 such tracks, systematic errors in the chamber positions could be found and corrected and the spatial resolution of each chamber measured in the transverse position and angle. These resolutions were used as assigned errors in the trajectory fitting program, to be discussed next, and were:

<u>Chamber</u>	<u>Transverse Y (vertical)</u>	<u>Transverse Z (horizontal)</u>
Prod. -dec.	.08", 6mr	.11", 6mr
FM	.03", 17mr	.03", 500mr
MM	.06", 17mr	.06", 500mr
RM	.03", 17mr	.03", 17mr
Shower	.20", 17mr	.20", 17mr

The huge 500mr angular resolution in the front and middle momentum chambers, horizontal view, is a reflection of the short track length and the staggering of sparks in the crossed electrical clearing and magnetic fields.

The information obtained from the measurements was, at this stage, in the form of a 3-D equation of a segment of track at each

chamber where a measurement was made. The next step was to find the orbit which gave the best fit to these track segments and thence to calculate the momentum of the particle from the known magnetic field.

A subroutine was written which could generate a trajectory through the magnetic field from a given initial momentum and direction. In order to fit the measured segments to a common trajectory, an initial momentum and direction were guessed at, traced through the magnet and compared with the measured track at each chamber. The derivative of the position and slope was calculated at each chamber, with respect to the five initial parameters. Using this information, the best fitting trajectory was obtained by minimizing its χ^2 as a function of the initial parameters. The five initial parameters of each track were then varied to constrain the two trajectories to intersect at a unique point in space, the decay vertex.

With 3- momenta of the two decay secondaries known, the invariant mass of different decay hypotheses was calculated, e.g., $m_{\pi e}$, $m_{\pi\pi}$, m_{ee} , etc.. The following information was then compiled into a 1,000-word record and written out on magnetic tape:

- 1) Bookkeeping information, e.g., frame number, date measured, etc.
- 2) Information from the data tape record written during the experiment, e.g., which counters fired, pulse height in gas counter, shower modules, etc.
- 3) Information on trajectories of decay secondaries, e.g., transverse coordinates at places of interest in the

apparatus, decay vertex coordinates, etc.

- 4) Quantities calculated from the momenta, e.g., $m_{\pi e}$, $m_{\pi\pi}$, etc.
- 5) Error matrices for measurements in each chamber and of the final fit.

Appendix 1.2: Monte Carlo Program

Discussion of the Monte Carlo program will first deal with the simulation of $K_S \rightarrow 2\pi$ decay and later with $K^0 \rightarrow \pi e \nu$. In each case it is assumed that p_K , θ_K , and x_K are given.

 $K_S \rightarrow \pi^+ \pi^-$

These were randomly generated in the center-of-mass system and then Lorentz-transformed into the laboratory system using p_K and θ_K . The individual decay secondaries had their orbits traced through the magnetic field. If both secondaries succeeded in traversing the field region without striking the magnet poles, coils or return iron, then the Monte Carlo event was subjected to the following checks:

- 1) Decay vertex within fiducial volume.
- 2) Tracks are contained in fiducial volume for their length in decay region.
- 3) One track hits S5.
- 4) Both tracks hit MH and go through different counters separated by at least one counter.
- 5) Both tracks hit RH and go through different counters.
- 6) Both tracks hit shower modules.

For $K_S \rightarrow 2\pi$ it was demanded that both tracks be contained within the GC front and rear windows. The only reason for this demand was historical -- at first it was feared that tracks traversing 3/4" of aluminum would reconstruct poorly, but it was later found that this was not the case and for the K_{e3} 's the requirement was not imposed. Events satisfying all the preceding conditions were written on magnetic tape for subsequent examination.

Besides being a complex simulation program, the Monte Carlo program had as input very many parameters of the apparatus which were measured in the survey carried out at the end of the experiment. It is desirable to have as many checks as possible on such a procedure. Besides the checks mentioned in the text -- momentum, angular and decay vertex position distributions -- it was also possible to compare the decay secondary transverse position distribution (commonly called profile) for data and M.C. events at different points. For $K_S \rightarrow 2\pi$, profiles were compared in both Y and Z directions at a) end of decay region, b) MH, and c) RH. These comparisons are shown for T1 data in Fig.'s 50 and 51. The agreement is good in all profiles except that the data have a bigger dip than the Monte Carlo at $Z = 0$ in all Z-profiles. This is probably due to (1) a concentration of material at $Z = 0$ behind the gas counter mirrors, and (2) a tendency to miss events which are near the center-line of the shower chambers. Neither of these effects give position biases in the front end so it was not necessary to correct for them.

The only inconsistency found in the $K_S \rightarrow \pi^+\pi^-$ data was that the number of events actually coming from T2 was 70% of the number calculated from the T1 rate, correcting for efficiency and beam flux differences. For one set of runs this was:

$$N_{T1} \times \frac{(\text{T2 Beam})}{(\text{T1 Beam})} \times \frac{(\text{T2 Efficiency})}{(\text{T1 Efficiency})} = 349$$

and 241 events were actually seen, so the $K_S \rightarrow 2\pi$ rate from T2 is $(.7 \pm .1)$ of the rate expected.

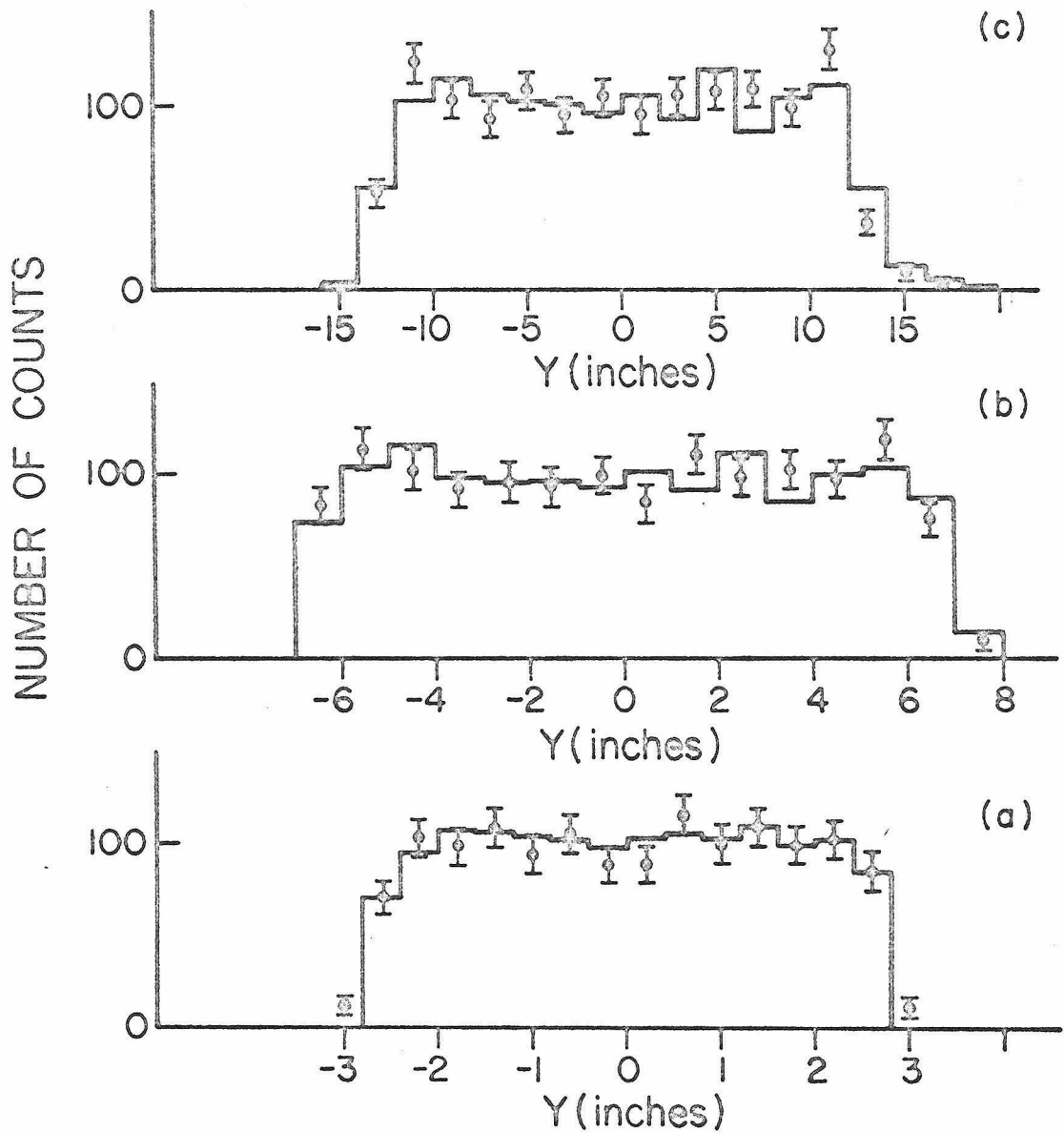


Fig. 50 Comparison between calibration data (points) and Monte Carlo (histograms) for Y-profile of π at (a) End of decay region, (b) MH and (c) RH.

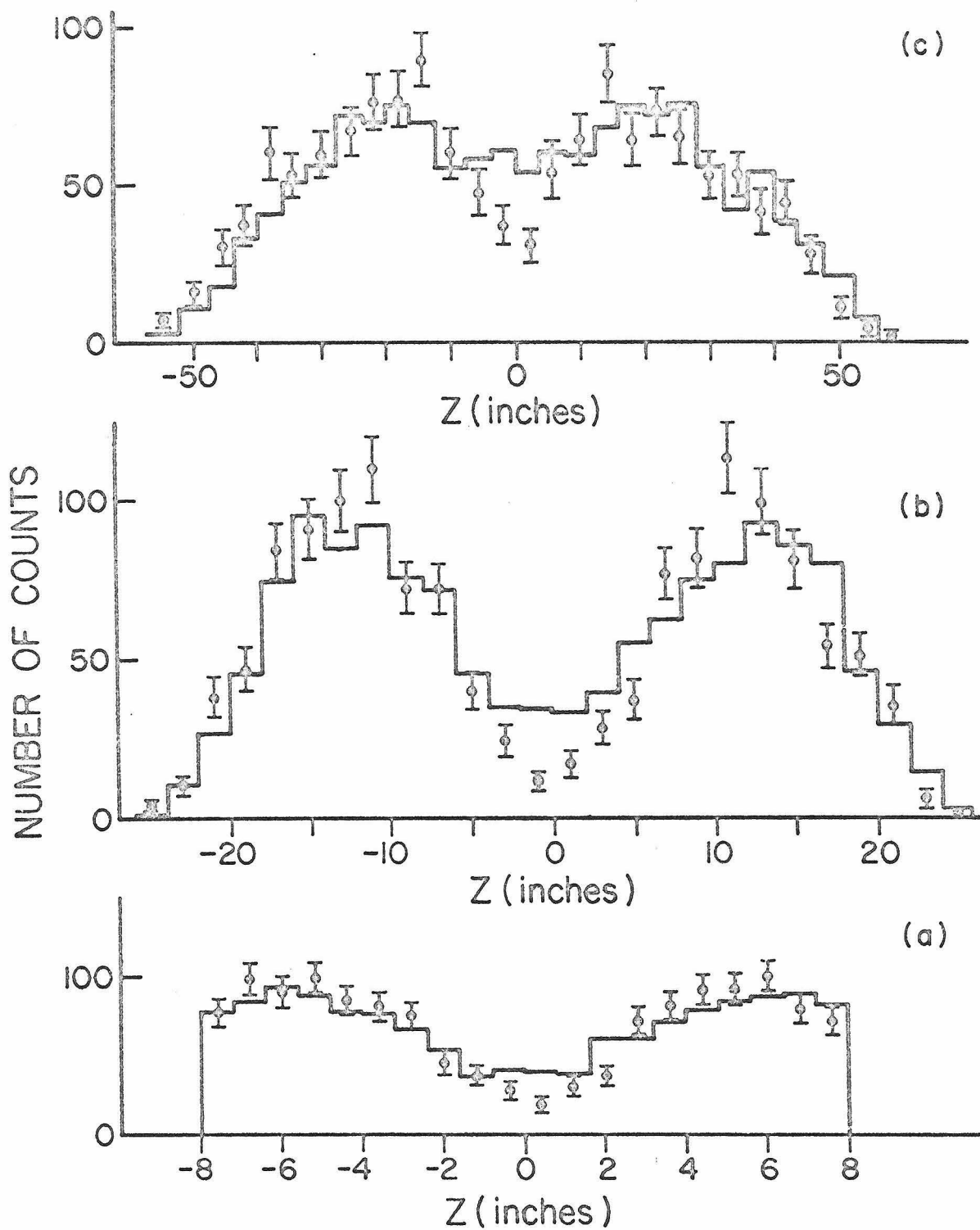


Fig. 51

Comparison between calibration data (points) and Monte Carlo (histograms) for Z-profile of π at (a) End of decay region, (b) MH and (c) RH.

This discrepancy may be due to the difference in geometry between T1 and T2. For example, secondaries from T2 may get into the MH without passing through V_2 , thus vetoing the event, whereas this would be rarer from T1 which is 24" further away from the MH. It was felt that this failure to normalize the targets for $K_{\pi 2}$ data would only affect the physics if one attempted to impose a normalization in fitting the K_{e3} 's. The efficiency calculations were checked very thoroughly to be sure that the effect was not due to a programming error.

$K^0 \rightarrow \pi e \nu$

The Monte Carlo K_{e3} 's were generated in the E_{π} vs. E_e Dalitz plot with the spectrum that one gets from the matrix element in Appendix 1 with $\xi = \frac{f_-}{f_+} = 0$ and no q^2 - dependence in f_+ . (29) They were then Lorentz-transformed into the lab, using p_K and θ_K as given. The Monte Carlo events were then sent through exactly the same program as the $K_S \rightarrow 2\pi$ events without the added requirement that both tracks be within the GC windows. As before, successes were written on magnetic tape for later examination. Fig.'s 52 and 53 show Z-profile comparisons for both e and π from T1 events at three locations in apparatus and again the agreement is good.

For the K_{e3} data the relative number of events from T1 and T2 is in agreement with the calculated ratio. However, when fitting, the normalization between the targets was still allowed to vary as a free parameter.

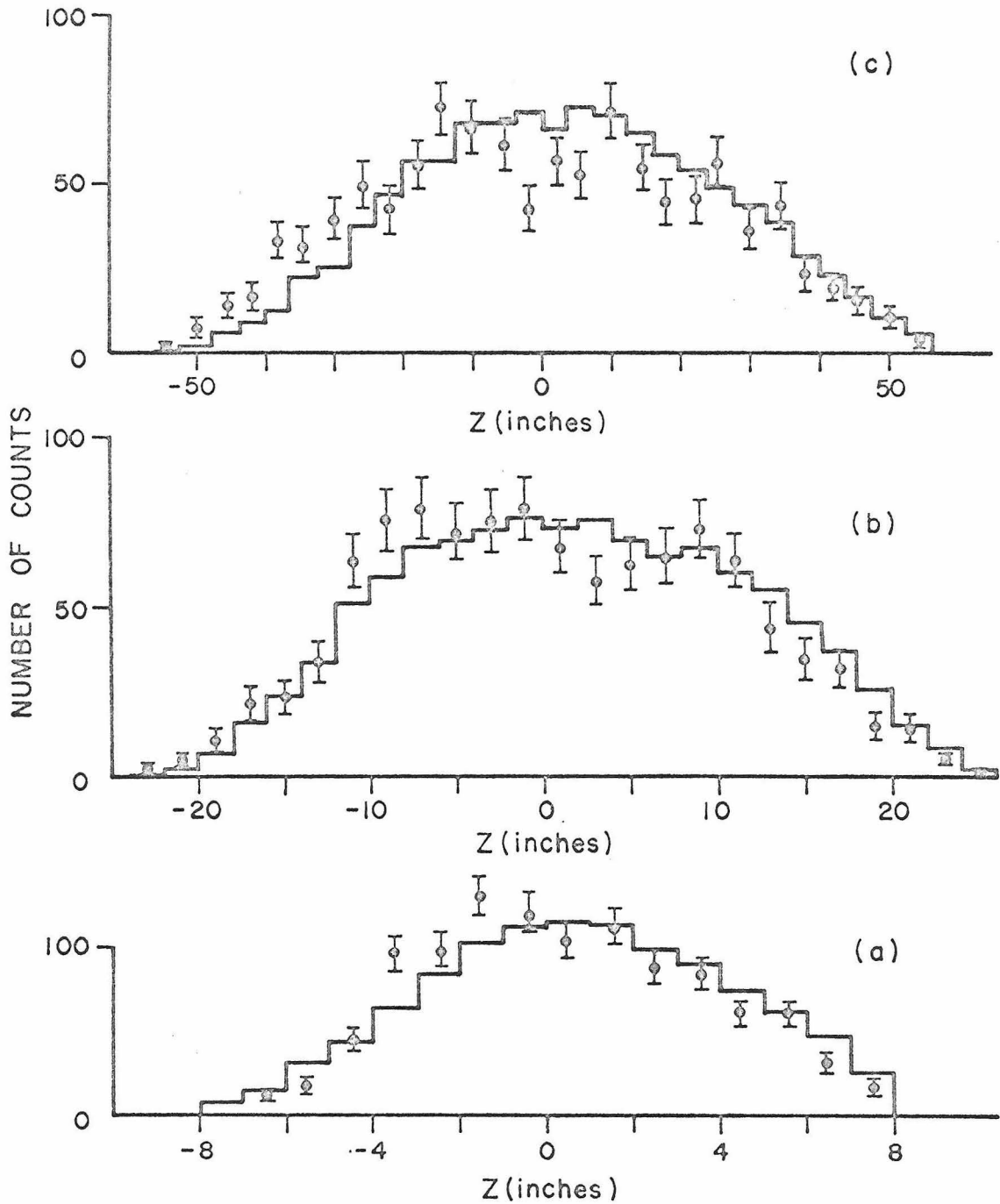


Fig. 52

Comparison between μ_e data (points) and Monte Carlo (histograms) for Z-profile of e at (a) End of decay region, (b) MH and (c) RH.

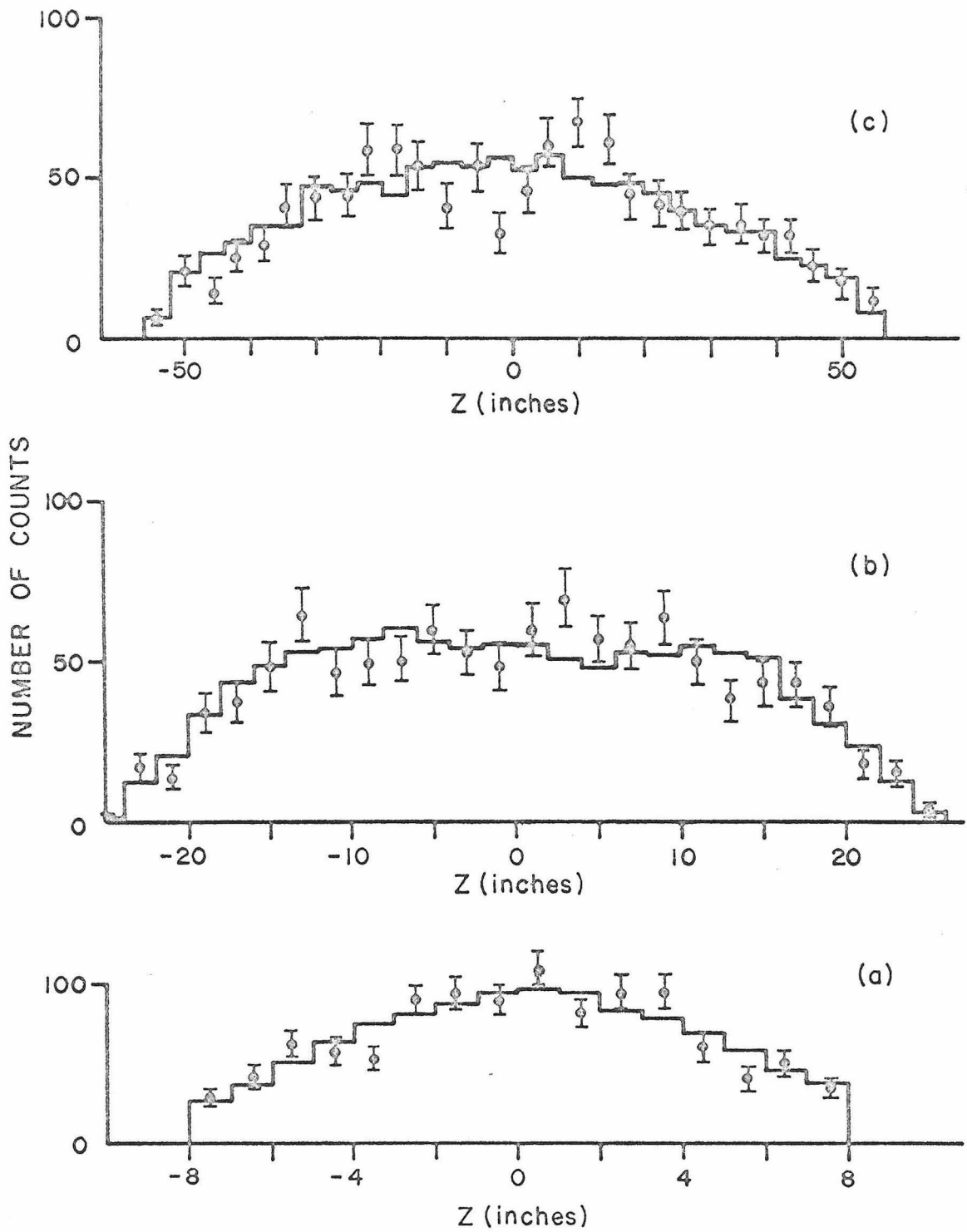


Fig. 53 Comparison between π data (points) and Monte Carlo (histograms) for Z-profile of π at (a) End of decay region, (b) MH and (c) RH.

Appendix 13: Smearing of Time Distributions Used in Maximum Likelihood Calculation

Corrections were made to $N^+(t)$ due to spread of production point in targets and the finite width of the momentum spectrum of accepted K_{e3} 's. The latter has already been shown in Fig. 24. In general, the proper time is give by:

$$\tau = \frac{m_K}{p_x c} (x_D - x_P) = k \frac{(x_D - x_P)}{p_x} \quad \text{putting } k = m_K c^{-1}$$

where x_D is the decay point, x_P is the production point, measured from the center of the target so that $\langle x_P \rangle \approx 0$ and p_x is the x-component of K^0 momentum. The effect of the width in $(x_D - x_P)$ and p_x was taken into account in a Taylor's expansion as follows:

$$f\left(k \frac{x_D - x_P}{p_x}\right) \approx f(l) + \frac{1}{2} \left\{ f''(l) l^2 \left(\frac{\sigma_p^2}{p_0^2} + \frac{\sigma_x^2}{x_D^2} \right) + 2f'(l) l \frac{\sigma_p^2}{p_0} \right\},$$

where $l = kx_D$, $1/p_0 = \langle 1/p_x \rangle$ and $\sigma_x^2 = (\sigma_{x_D}^2 + \sigma_{x_P}^2)$. σ_{x_D} was

calculated from the reconstruction of each event, σ_{x_P} was taken as

.3" corresponding to uniform production in the targets and σ_p as

.38 GeV/c from the p_K - spectrum. The effect of the p_K - spectrum can

be taken into account exactly by numerical integration.

The $N^+(t)$ time distributions were calculated for the three cases:

- (a) Effect of spread in p_K neglected.

(b) Taken into account up to the second moment by the above scheme.

(c) Folded into the distribution numerically.

Fig. 54 shows the difference of (a) - (b) and the difference (c) - (b).

If the fit to X is done with the time distributions from (a), one gets

$$\text{Re}X = -.080 \begin{matrix} +.036 \\ -.034 \end{matrix}, \quad \text{Im}X = +.104 \begin{matrix} +.084 \\ -.072 \end{matrix} \quad \text{compared to the final}$$

$$\text{Re}X = -.069 \pm .036, \quad \text{Im}X = +.108 \begin{matrix} +.092 \\ -.074 \end{matrix} \quad \text{quoted from using (b)}. \quad \text{The}$$

effect of (c) on the time distributions changes the relative proba-

bility by $< 0.5\%$ of N^+ at $t = 0$, when compared to the time distri-

butions from (b). This is less than the difference between the

distributions from (b) to (a). Since the change in X from using (b)

to using (a) is negligible compared to the statistical error, it

follows that the effect of neglecting higher moments has a negligible

effect on X.

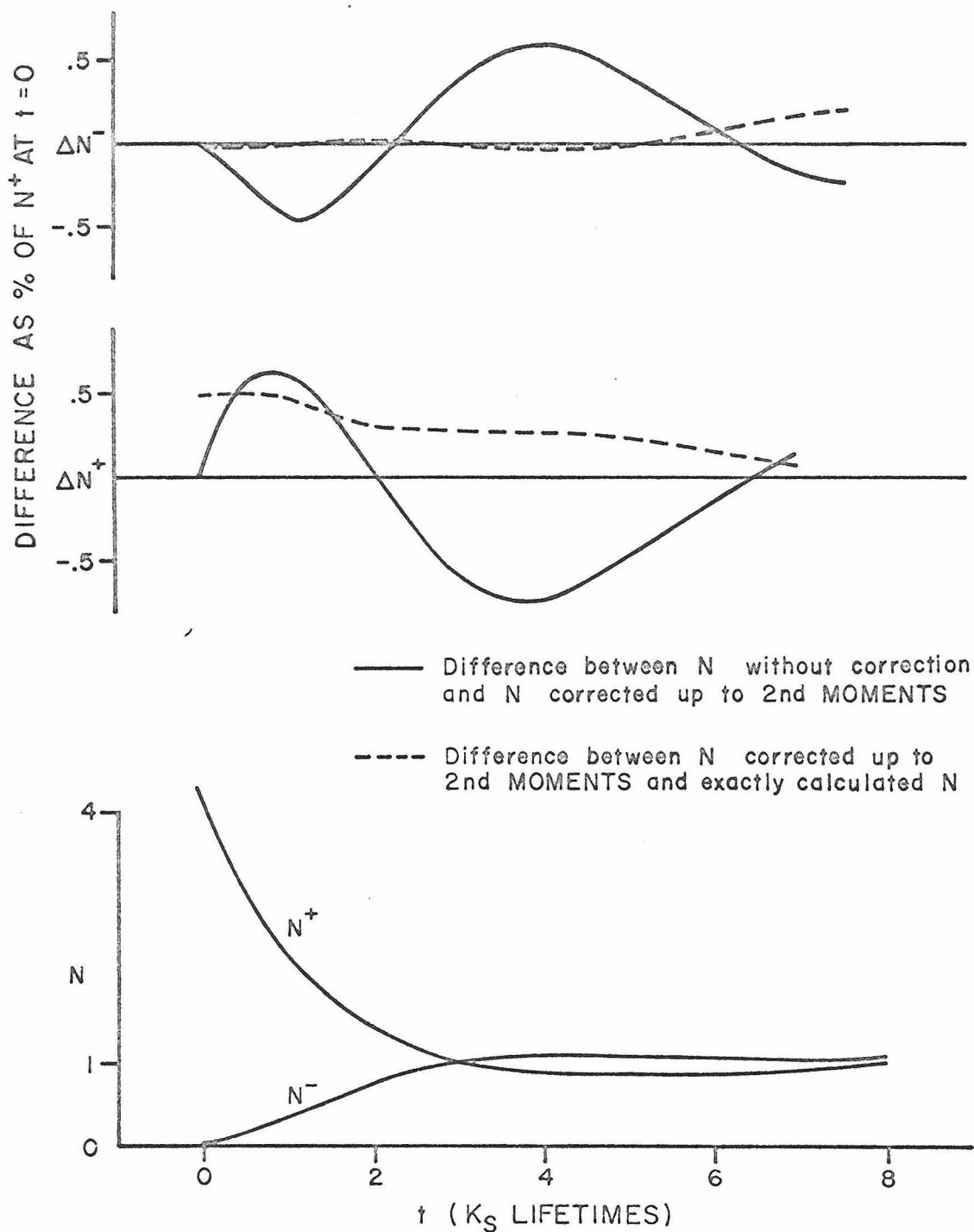


Fig.54 Difference in N^+ (N^-) with various corrections for higher moments of p_K -spectrum. N^+ and N^- for $X = 0$ are also shown.

VII. REFERENCES

1. R. P. Feynman and M. Gell-Mann, Phys. Rev. 109, 193 (1958).
2. N. Cabibbo, Phys. Rev. Letters 10, 531 (1963).
3. R. G. Sachs, Phys. Rev. Letters 13, 286 (1964).
4. F. S. Crawford, Rapporteurs Talk, Proceedings of the XIth International Conference on High Energy Physics, CERN, 1962.
5. A. Barbaro-Galtieri, W. H. Barkas, H. H. Heckman, J. W. Patrick and F. M. Smith, Phys. Rev. Letters 9, 26 (1962).
6. R. P. Ely, W. M. Powell, H. White, M. Baldo-Ceolin, E. Calimani, S. Ciampolillo, O. Fabbri, F. Farini, C. Filippi, H. Huzita, G. Miari, U. Camerini, W. F. Fry and S. Natali, Phys. Rev. Letters 8, 132 (1962).
7. G. Alexander, S. P. Almeida and F. S. Crawford, Phys. Rev. Letters 9, 69 (1962).
8. Proceedings of the 1969 Topical Conference on Weak Interactions at CERN, CERN-69-7, Hyperon Decays, p. 131, H. Filthuth; Leptonic K-decays, p. 227, C. Rubbia.
9. U. Nauenberg, P. Schmidt, J. Steinberger, S. Marateck, R. J. Plano, H. Blumenfeld, and L. Seidletz, Phys. Rev. Letters 12, 679 (1964).
10. F. Eisele, R. Engelmann, H. Filthuth, W. Fohlisch, V. Hepp, E. Leitner, W. Presser, H. Schneider, M. L. Stevenson, and G. Zech, Zeitschrift fur Physik 221, 401 (1969).

REFERENCES (Continued)

11. A. Barbaro-Galtieri, G. E. Derenzo, T. R. Price, A. Rittenberg, A. H. Rosenfeld, N. Barash-Schmidt, C. Bricman, M. Roos, P. Soding, and C. G. Wohl, *Rev. Mod. Phys.* 42, 87 (1970).
12. B. Aubert, L. Behr, F. L. Canavan, L. M. Chounet, J. P. Lowys, P. Mittner, and C. Pascaud, *Physics Letters* 17, 59 (1965).
13. M. Baldo-Ceolin, E. Calimani, S. Ciampolillo, C. Filippini-Filosofo, H. Huzita, F. Mattioli, and G. Miari, *Nuovo Cimento* 38, 684 (1965).
14. P. Franzini, L. Kirsch, P. Schmidt, J. Steinberger, and R. J. Plano, *Phys. Rev.* 140, B127 (1965).
15. L. Feldman, S. Frankel, V. L. Highland, T. Sloan, O. B. Van Dyck, W. D. Wales, R. Winston, and D. M. Wolfe, *Phys. Rev.* 155, 1611 (1967).
16. D. G. Hill, D. Luers, D. K. Robinson, M. Sakitt, O. Skjeggestad, J. Canter, Y. Cho, A. Dralle, A. Engler, H. E. Fisk, R. W. Kraemer, and C. M. Meltzer, *Phys. Rev. Letters* 19, 668 (1967).
17. B. R. Webber, F. T. Solmitz, F. S. Crawford, and M. Alston-Garnjost, *Phys. Rev. Letters* 21, 498 (1968).
18. F. James and H. Briand, paper submitted to XIVth International Conference, Vienna 1968.
19. L. S. Littenberg, J. H. Field, O. Piccioni, W. A. W. Mehlhop, S. S. Murty, P. H. Bowles, and T. H. Burnett, *Phys. Rev. Letters* 22, 654 (1969).

REFERENCES (Continued)

20. S. Bennett, D. Nygren, H. Saal, J. Sunderland, J. Steinberger, and K. Kleinknecht, *Physics Letters* 29B, 317 (1969).
21. O. I. Dahl, L. M. Hardy, R. I. Hess, J. Kirz, and D. H. Miller, UCRL-16978 (1967).
O. I. Dahl, L. M. Hardy, R. I. Hess, J. Kirz, D. H. Miller, and J. Schwartz, UCRL-17217 (1967).
22. An estimate of $\sigma(K^-p \rightarrow \bar{K}^0n)$ at 2.85 GeV/c was obtained from data at $P_K = 1.8$ GeV/c (P. M. Dauber, *Phys. Rev.* 134, (1964) B1370) where the cross section was measured to be $(1.55 \pm .09)$ mb and data at $P_K = 5, 7, 12$ GeV/c (P. Astbury *et al.*, *Physics Letters* 23, 396 (1966)) where $\sigma = (151 \pm 18)\mu\text{b}$ $(99 \pm 8)\mu\text{b}$ and $(45 \pm 5)\mu\text{b}$. The data were fit to a power law in s and from this the cross section at 2.85 GeV/c was estimated to be $500\mu\text{b}$.
23. T. D. Lee and C. S. Wu, *Ann. Rev. of Nucl. Sci.*, 16, 511 (1966).
24. J. D. Jackson, 1962 Brandeis Lectures, Vol. I.
25. C. D. Buchanan, to be published in *Nuovo Cimento Letters*.
26. D. Dorfan, J. Enstrom, D. Raymond, M. Schwartz, and S. Wojcicki, *Phys. Rev. Letters* 19, 987 (1967).
27. S. Bennett, D. Nygren, H. Saal, J. Steinberger, and J. Sunderland, *Phys. Rev. Letters* 19, 993 (1967).
28. T. Kirk, J. Marx, D. Nygren, J. Peoples, and J. Steinberger, preliminary result reported to 1969 CERN Topical Conference on Weak Interactions (see p. 297, ref. 8).
29. F. J. Sciulli, University of Pennsylvania, Doctoral Dissertation, 1965.